3407

NATIONAL LIBRARY

OTTAWA

BIBLIOTHÈQUE NATIONALE

OTTAWA

NAME OF AUTHOR...Stuart Kenneth Searles.....

TITLE OF THESIS...Equilibrium Gas Phase Solvation Reactions

.....

.....

UNIVERSITY..of Alberta.....

DEGREE....Ph. D.....YEAR GRANTED.....1968.....

Permission is hereby granted to THE NATIONAL LIBRARY OF CANADA to microfilm this thesis and to lend or sell copies of the film.

The author reserves other publication rights, and neither the thesis nor extensive extracts from it may be printed or otherwise reproduced without the author's written permission.

(Signed)..Stuart...Searles

PERMANENT ADDRESS:

National Bureau of Standards
Radiation Chemistry Section
.....
Washington, D. C. 20234
.....

DATED.....Dec. 23,..1968

NL-91

THE UNIVERSITY OF ALBERTA

Mass Spectrometric Investigation of the Equilibrium Gas Phase Solvation Reactions Involving (a) Hydration of the Proton, (b) Hydration of the Potassium Ion, and (c) Solvation of the Ammonium Ion by Ammonia Molecules

by

© Stuart Kenneth Searles

A THESIS

SUBMITTED TO THE FACULTY OF GRADUATE STUDIES

IN PARTIAL FULFILMENT OF THE REQUIREMENTS FOR THE DEGREE

OF DOCTOR OF PHILOSOPHY

DEPARTMENT OF CHEMISTRY

EDMONTON, ALBERTA

September, 1968

THE UNIVERSITY OF ALBERTA

FACULTY OF GRADUATE STUDIES

The undersigned certify that they have read, and recommended to the Faculty of Graduate Studies for acceptance, a thesis entitled

MASS SPECTROMETRIC INVESTIGATION OF THE EQUILIBRIUM GAS PHASE SOLVATION REACTIONS

involving: (a) Hydration of the Proton, (b) Hydration of the Potassium Ion, and (c) Solvation of the Ammonium Ion by Ammonia Molecules submitted by Stuart Kenneth Searles in partial fulfilment of the requirements for the degree of Doctor of Philosophy.

P. Kebarle
Supervisor

W. B. Dunford

W. Allen

F. Weinhaus

J. R. Brenon

Jean H. Futrell
External Examiner

Date September 4, 1968

ABSTRACT

A specially designed mass spectrometer was used to analyze the equilibrium concentrations of gas phase solvated ions arising from: 1. the irradiation of water vapor, 2. the irradiation of ammonia vapor, and 3. the thermal ionization of potassium in water vapor. The analyses proved the occurrence of the general reactions 1-3 respectively. The notation n-1,n is used to denote specific reactions. (For example, reaction 1,2 of the general reaction 1 is $H^+(H_2O) + H_2O \rightleftarrows H^+(H_2O)_2$).

(1) $H^+(H_2O)_{n-1} + H_2O \rightleftarrows H^+(H_2O)_n$ $\quad n = 2\text{-}7$

(2) $NH_4^+(NH_3)_{n-1} + NH_3 \rightleftarrows NH_4^+(NH_3)_n$ $\quad n = 1\text{-}6$

(3) $K^+(H_2O)_{n-1} + H_2O \rightleftarrows K^+(H_2O)_n$ $\quad n = 1\text{-}6$

Measurement of the gaseous solvent pressure led to determination of the equilibrium constants $K_{n-1,n}$ for reactions 1-3. Typically the pressure was varied from 0.2 to 3 torr to prove the necessary condition that $K_{n-1,n}$ is pressure independent. A temperature study of the reactions over the range -60° to 600°C allowed determination of $\Delta G°_{n-1,n}$, $\Delta H°_{n-1,n}$, and $\Delta S°_{n-1,n}$ from van't Hoff type plots. With one exception these values monotonically increased with increasing cluster size. The ranges for $\Delta H°_{n-1,n}$ (298°K, 1 atm) were -36 to -11.7, -27 to -7.5, and -17.9 to -10.0 kcal/mole for reactions 1-3 respectively. The experimental

entropy values for $\Delta S°_{1,2}$ for reaction 1 and $\Delta S°_{0,1}$ for reactions 2 and 3 were in agreement with those calculated from statistical mechanics.

The values of $\Delta H°_{n-1,n}$ for reaction 3 were in approximate agreement with the theoretical values obtained from classical electrostatic calculations. These calculations took into account ion-dipole, ion-polarizability, ion-atom repulsion, and dipole-dipole repulsion energy terms. The calculations were performed with the assumption that all $K^+ — H_2O$ distances are equal, i.e. the cluster has a single shell of water molecules. The conclusion from these calculations was that the increase in dipole-dipole repulsion energy with cluster size primarily accounted for the increase in $\Delta H°_{n-1,n}$ with increasing n. A special electrostatic calculation indicated that the formation of an outer shell of water molecules becomes energetically favorable for reaction 3 with n = 7 i.e. reaction 6,7.

The clusters $NH_4^+(NH_3)_n$ and $H^+(H_2O)_n$ are more complicated since these clusters could also be $H^+(NH_3)_{n+1}$ and $H_3O^+(H_2O)_{n-1}$ respectively. The smooth change of the thermodynamic values with n for reaction 1 was interpreted to mean that the appropriate formula for the hydrates is $H^+(H_2O)_n$.

In contrast to the thermodynamic values for $H^+(H_2O)_n$, the results for $NH_4^+(NH_3)_n$ had a break in the thermodynamic values. The break appeared between reactions 3,4 and 4,5 as

as a sharp increase in the values. This suggested the existence of an inner cluster $NH_4^+(NH_3)_4$. Since a more distantly bound ammonia molecule will be more weakly bound, the values of $\Delta H°_{4,5}$ and $\Delta S°_{4,5}$ are greater.

From the present results, some comparisons are made to ionic solvation in the liquid phase.

With the experimental value of $\Delta H°_{0,1}$ for reaction 3 and known thermodynamic values, the proton affinity of KOH was calculated to be 262 kcal/mole.

ACKNOWLEDGMENTS

It is a pleasure to acknowledge the guidance and encouragement of Dr. P. Kebarle, who directed this work. The author also acknowledges the work of Dr. A. Zolla who worked jointly with the author in obtaining data on the proton hydration and in performing preliminary experiments on the potassium ion hydration. The project was also influenced by the members of the mass spectroscopy group at the University of Alberta.

The technical staff of the Chemistry Department, especially the Machine Shop, was helpful in solving the instrumental problems which arose.

The author wishes to thank Mrs. Gladys Whittal for typing the manuscript.

The understanding and encouragement of the author's wife, Sharon, is sincerely appreciated. Her care in drawing the figures and proofreading the manuscript was invaluable.

The financial assistance provided by the University of Alberta and the National Research Council is gratefully acknowledged.

TABLE OF CONTENTS

LIST OF FIGURES

LIST OF TABLES

1. INTRODUCTION TO THE GAS PHASE SOLVATION OF IONS

1.1 The Nature of Solvation Reactions

Gas phase ion-molecule reactions have been classified according to reactions 1.1 - 1.5 (1):

1.1	Simple Charge Transfer		$AB^+ + CD \longrightarrow AB + CD^+$
1.2	Charge Transfer Induced Dissociation		$AB^+ + CD \longrightarrow AB + C^+ + D$
1.3	Radical or Atom Abstraction	a.	$AB^+ + CD \longrightarrow ABD^+ + C$
		b.	$AB^+ + CD \longrightarrow A^+ + BCD$
1.4	Ionic Abstraction	a.	$AB^+ + CD \longrightarrow A + BCD^+$
		b.	$AB^+ + CD \longrightarrow ABD + C^+$
1.5	Attachment		$AB^+ + CD \longrightarrow ABCD^+$

Gas phase solvation reactions are ion-molecule reactions of the attachment type. More precisely, they form a sub-class of attachment reactions. These reactions are characterized by the resulting relatively weak bond strengths (of the order of 10 kcal/mole) between the ion and the molecule. The bonding between the ion and the molecule results from the electrostatic attraction of the ion for the molecule. In the present work, in which the solvent molecules were either NH_3 or H_2O, the major attractive forces were ion-dipole and ion-polarizability.

Reactions 1.6 - 1.9 represent solvation reactions where M is the third body required to remove the excess energy which is

due to the heat of reaction. If the cluster has a large number of degrees of freedom, the deactivation of the cluster by the third body may not be necessary. The equilibrium cluster sizes

1.6 $$A^+ + S \underset{\longleftarrow}{\overset{M}{\longrightarrow}} A^+S \qquad (0,1)$$

1.7 $$A^+S + S \underset{\longleftarrow}{\overset{M}{\longrightarrow}} A^+S_2 \qquad (1,2)$$

1.8 $$A^+S_2 + S \underset{\longleftarrow}{\overset{M}{\longrightarrow}} A^+S_3 \qquad (2,3)$$

1.9 $$A^+S_{n-1} + S \underset{\longleftarrow}{\overset{M}{\longrightarrow}} A^+S_n \qquad (n-1,n)$$

formed during the solvation reactions are strongly temperature dependent.

When the ionic charge becomes well shielded by one or more layers of solvent molecules, the reactions might be better termed condensation reactions, 1.10, rather than solvation

1.10 $$S_{(g)} \longrightarrow S_{(\ell)}$$

reactions. This viewpoint considers the cluster A^+S_n equivalent to a liquid drop. In the present work it was found that the thermodynamic values for $\Delta H°$, $\Delta G°$, and $\Delta S°$ for reaction 1.11 were approaching the values for reaction 1.12. The

1.11 $$H^+(H_2O)_{n-1} + H_2O \longrightarrow H^+(H_2O)_n \qquad n = 2\text{-}8$$

1.12 $$H_2O_{(g)} \longrightarrow H_2O_{(\ell)}$$

comparison to a liquid drop can be extended by considering other

properties of the ionic cluster. For example, the dielectric constant of the cluster is expected to be greater than that of the surrounding gas. As the cluster size increases, the dielectric constant is expected to increase and perhaps eventually approach the dielectric constant of liquid water. The dielectric constant of the cluster is relevant to the present work. If the dielectric constant increases rapidly with cluster size, the strength of the "electrostatic ion-solvent molecule bonds" will decrease rapidly with cluster size because of the inverse dependence of the ion-dipole energy on the dielectric constant.

Ion-solvent molecule interactions can also be compared to the liquid phase. Two terms which are used to classify these interactions in the liquid phase are close and distant association. Close association is the association due to solvent molecules which immediately surround an ion and have their dipoles closely aligned with the electric field gradient of the ion. Other solvent molecules which are farther away (distant association) are more free to rotate their dipoles away from the electric field gradient. Since the clusters studied in this work were relatively small (up to seven solvent molecules), the solvation interactions in these clusters were probably predominantly due to close association.

1.2 Instrumentation Used to Observe Solvation Reactions

Mass spectrometers have been used to study ion-molecule reactions, including solvation reactions. A conventional mass spectrometer operates as follows. In the mass spectrometer ion source, an electron beam is used to ionize gas molecules S. The ions which are created include the parent ion S^+ and the lower molecular weight ions which arise from the fragmentation of the parent ion. A positively biased electrode, the repeller, accelerates the ions toward the ion exit slit of the ion source. Outside the ion source the ions are further accelerated and mass analyzed. The mass analyzed ionic species are then individually collected and recorded as an electrical current. When used in routine analytical analyses, the pressures in the ion source are in the range of 10^{-5} to 10^{-7} torr. Under these conditions the fraction of ions undergoing even a single collision is negligibly small. Thus in order to study higher order reactions such as 1.6 to 1.9 the pressure must be greatly increased. The present work used a modified mass spectrometer with ion source pressures from 0.2 to 6 torr. Since the ion acceleration, mass analysis, and collector regions should be maintained at less than 10^{-4} torr for the mass spectrometer to function properly, the mass spectrometer used in the present work used a high capacity pumping system and an ion source with narrow

slits (to reduce the gas flow out of the ion source).

1.3 Thermodynamic Equations Pertinent to Gas Phase Solvation Reactions

At sufficiently high pressures the initial ions in the present work reacted to form solvated ions. Assuming that equilibrium is achieved, the equilibrium constant $K_{n-1,n}$ for the solvation reaction n-1,n (reaction 1.9) can be calculated from equation 1.1 from a knowledge of the partial pressures

$$K_{n-1,n} = \frac{P_{A^+S_n}}{P_{A^+S_{n-1}} P_S} \qquad 1.1$$

of A^+S_n, A^+S_{n-1}, and S. Since the partial pressures of A^+S_n and A^+S_{n-1} in the present work were always at least four orders of magnitude less than the pressure of S, to a good approximation the ion source pressure was equal to P_S. From the mass analysis of the ionic clusters, the ionic pressures can be determined from equations 1.2 and 1.3 where $I_{A^+S_n}$ and $I_{A^+S_{n-1}}$ are the mass analyzed ion currents

$$P_{A^+S_n} = c_1 I_{A^+S_n} \qquad 1.2$$

$$P_{A^+S_{n-1}} = c_2 I_{A^+S_{n-1}} \qquad 1.3$$

of A^+S_n and A^+S_{n-1} respectively. c_1 and c_2 are proportionality constants whose evaluation requires both a knowledge of

the flow rate out of the ion source and a knowledge of the fraction of each ion current which is lost in transmission from the ion source to the ion collector. On substitution of 1.2 and 1.3 into 1.1, equation 1.4 is obtained. Assuming

$$1.4 \qquad K_{n-1,n} = \frac{c_1 \, I_{A^+S_n}}{c_2 \, I_{A^+S_{n-1}} \, P_S}$$

$c_1 = c_2$ reduces equation 1.4 to 1.5. The validity of this

$$1.5 \qquad K_{n-1,n} = \frac{I_{A^+S_n}}{I_{A^+S_{n-1}} \, P_S}$$

assumption is further discussed in Chapter 3.

Other thermodynamic functions can be obtained from $K_{n-1,n}$ values. The free energy change $\Delta G^\circ_{n-1,n}$ is given by equation 1.6. Since the values for $K_{n-1,n}$ in the present work

$$1.6 \qquad \Delta G^\circ_{n-1,n} = - RT \ln K_{n-1,n}$$

were calculated for a standard state of 1 torr, the values for $K_{n-1,n}$ were multiplied by 760 before substitution into 1.6 in order to obtain the other thermodynamic functions in a standard state of 1 atm. A variation of the temperature made it possible to determine $\Delta H^\circ_{n-1,n}$ and $\Delta S^\circ_{n-1,n}$ from equation 1.7.

$$1.7 \qquad \ln K_{n-1,n} = - \frac{\Delta H^\circ_{n-1,n}}{RT} + \frac{\Delta S^\circ_{n-1,n}}{R}$$

1.4 Significance of Gas Phase Solvation Reactions

A. In Ionic Mobility

The significance of gas phase solvation reactions can be realized from the number of fields in which these reactions play an important role. One such field is ionic mobility in which the gas phase transport of ions is studied as a function of gas pressure and electric field strength. Solvation reactions are used to explain the observed ionic mobilities. For example, in a study of the mobility of alkali metal ions in "moist" rare gases, Munson and Tyndall (2) have estimated (as an upper limit) that the number of water molecules attached to Li^+, Na^+, and K^+ are 6.2, 6.0, and 6.3 respectively. The role of solvation reactions in ionic mobility has been reviewed thoroughly by Loeb (3).

B. In the Liquid Phase

One of the reasons Munson and Tyndall carried out mobility measurements was to obtain an estimate of the ion hydration number in the liquid phase. Gas phase solvation reaction studies can also be used to give an indication of the structures of solvated ions. For example, it is concluded from the present results that $H^+(H_2O)_n$ is a better notation for the hydrates than $H_3O^+(H_2O)_{n-1}$. One advantage of working in the gas phase is that the solvation of positive and negative ions can be studied separately.

C. In the Upper Atmosphere

Solvated ions have been observed in the upper atmosphere. From rocket data Narcisi and Bailey (4) determined that the ions $H^+(H_2O)$ and $H^+(H_2O)_2$ account for 35% of the total positive ions in the D region (50 - 85 Km. altitude).

D. In Radiation Chemistry

Lind (5) has briefly reviewed the role of ionic clusters in radiation chemistry. The review states that ionic clusters were postulated by Lind in the early 1900's. However, the postulate lost importance in the 1930's after Eyring, Hirschfelder, and Taylor theorized that free radical mechanisms could more satisfactorily account for radiation chemistry results. More recently, the review continues, Magee and Funabashi have made theoretical calculations which demonstrate the stability of ionic clusters.

The increasing amount of information about ionic clusters (discussed in section 1.5) may lead to a greatly increased use of ionic clusters in explaining certain aspects of radiation chemistry. Anderson, Knight, and Winter (6) and Bansal and Freeman (7) have recently used solvation reactions in some of their postulated mechanisms.

E. In Gas Discharges

Dawson and Tickner (8) have observed the ions $NH_4^+(NH_3)_n$ in the ammonia glow discharge while Knewstubb and Tickner (9) have

observed the ions $H^+(H_2O)_n$ in the discharge of water vapor.

1.5 Previous Work on Gas Phase Solvation Reactions Detected Mass Spectrometrically

Because of the significance of gas phase solvation reactions to the fields mentioned in section 1.4, a number of mass spectroscopists have delved into the study of these reactions. Yang and Conway (10) have investigated reactions 1.6 with n = 2-5 under equilibrium conditions. The $\Delta H°_{n-1,n}$

$$O^+_{2n} + O_2 \rightleftarrows O^+_{2n+2} \qquad 1.6$$

values they obtained ranged from -9.7 to -2.1 kcal/mole. By equating the O^+_2 — O_2 bond energy to - $\Delta H°_{0,1}$, theoretical values of $\Delta H°_{n-1,n}$ were calculated. These values were in satisfactory agreement with the experimental values.

With the use of deuterated compounds, Sieck, Abramson, and Futrell (11) have investigated the mechanisms leading to the formation of $H^+(CH_3OH)_3$ and $H^+(C_2H_5OH)_3$. The investigation used both a high pressure mass spectrometer and a tandem mass spectrometer.

Munson (12) has reported the high pressure mass spectra (up to 0.3 torr) of H_2O, CH_3OH, CH_3OCH_3, and CH_3CHO. The ions $H^+(H_2O)_n$, $H^+(CH_3OH)_n$, $H^+(CH_3OCH_3)_n$, and $H^+(CH_3CHO)_n$ where n = 1-2 for each species were found to constitute a large

fraction of the total ionization of the respective gases at 0.3 torr.

In a second paper by Munson (13) the ions $H^+(CH_3NH_2)_n$, $H^+((CH_3)_2NH)_n$, and $H^+((CH_3)_3N)$ where n = 1-2 were reported to occur at high pressures of the gases CH_3NH_2, $(CH_3)_2NH$, and $(CH_3)_3N$ respectively. In each gas the solvated ions constituted at least 40% of the total ionization at a pressure of 0.3 torr.

Using a field emission ion source at -195°C, Beckey (14) was able to observe the hydrates $H^+(H_2O)_n$ with n as high as ten. By varying the temperature he determined the values of $\Delta H°_{1,2}$ and $\Delta H°_{2,3}$ to each be about 4 kcal/mole. These values are much lower than the values determined in this work. It may be that the excess energy acquired by the ion during field ionization led to non-equilibrium results in Beckey's work.

A number of investigations have been reported from this laboratory dealing with solvation reactions occurring under equilibrium conditions. In references (15,16) the solvation of NH_4^+ by NH_3 is reported. The competitive solvation of NH_4^+ by NH_3 and H_2O and of H^+ by H_2O and CH_3OH has been studied (17,18 respectively). The hydration of H^+ has also been investigated (19,20). In reference (21), the hydration of the halide ions F^-, Cl^-, Br^- and I^- is reported.

2. EXPERIMENTAL

Measurements were made in a 60°, 15 cm radius mass spectrometer which had been specially modified for the study of ion solvation in the gas phase. The primary ions were generated in the electrically field free high pressure ion source (up to 5 torr) by a 100 kev proton beam from a proton accelerator or by thermal ionization from a heated filament. The ions escaped from the ion source by diffusion and mass flow into the high vacuum region containing the accelerating electrodes. High vacuum was maintained by the low conductance of gas out of the ion source and by the high capacity pumping system.

The ions were accelerated and focussed by a modified Nier type acceleration system. Detection, after mass analysis, was obtained by a 17 stage electron multiplier and a Victoreen Femtometer. The apparatus was designed and assembled by G. Collins (22). Features of the instrument of particular importance to the gas phase solvation work are described in the subsequent experimental sections.

2.1 Instrumental Requirements to Observe Solvation Equilibria

The instrumentation required for the study of the gas phase solvation of ions must produce ions, allow them to react at high pressures, and mass analyze the reactant and product ions. Because of its ability to satisfy all three requirements,

a modified mass spectrometer has been used in this study. A conventional mass spectrometer, Figure 2.1, produces ions by electron impact in the ion source. The electrons are emitted by a hot filament and accelerated through a potential difference between the ion source and the filament. The electron beam enters the ion source through the electron beam entrance slit and ionizes the gas molecules in its path as it traverses the length of the ion source. The beam is then collected in a Faraday cup. The ions which are created are accelerated out of the ion source by a positive electric field between the repeller and the ion source.

After the ions pass out of the ion exit slit, they are accelerated by a potential difference, generally equal to 2000 v, and enter the magnetic mass analyzer tube. Each ion is deflected by the perpendicular magnetic field according to its mass to charge ratio m/e. Each m/e can be individually focussed on the ion collector by varying the magnetic field. This current is amplified and displayed on a recorder. Conventional mass spectrometers are more fully described in reference (23).

To investigate gas phase solvation reactions, the ion source pressure must be high. The required pressure can be approximately calculated. To obtain clusters as large as six ligands about the central ion, the ion must undergo six collisions plus additional collisions to remove the excess

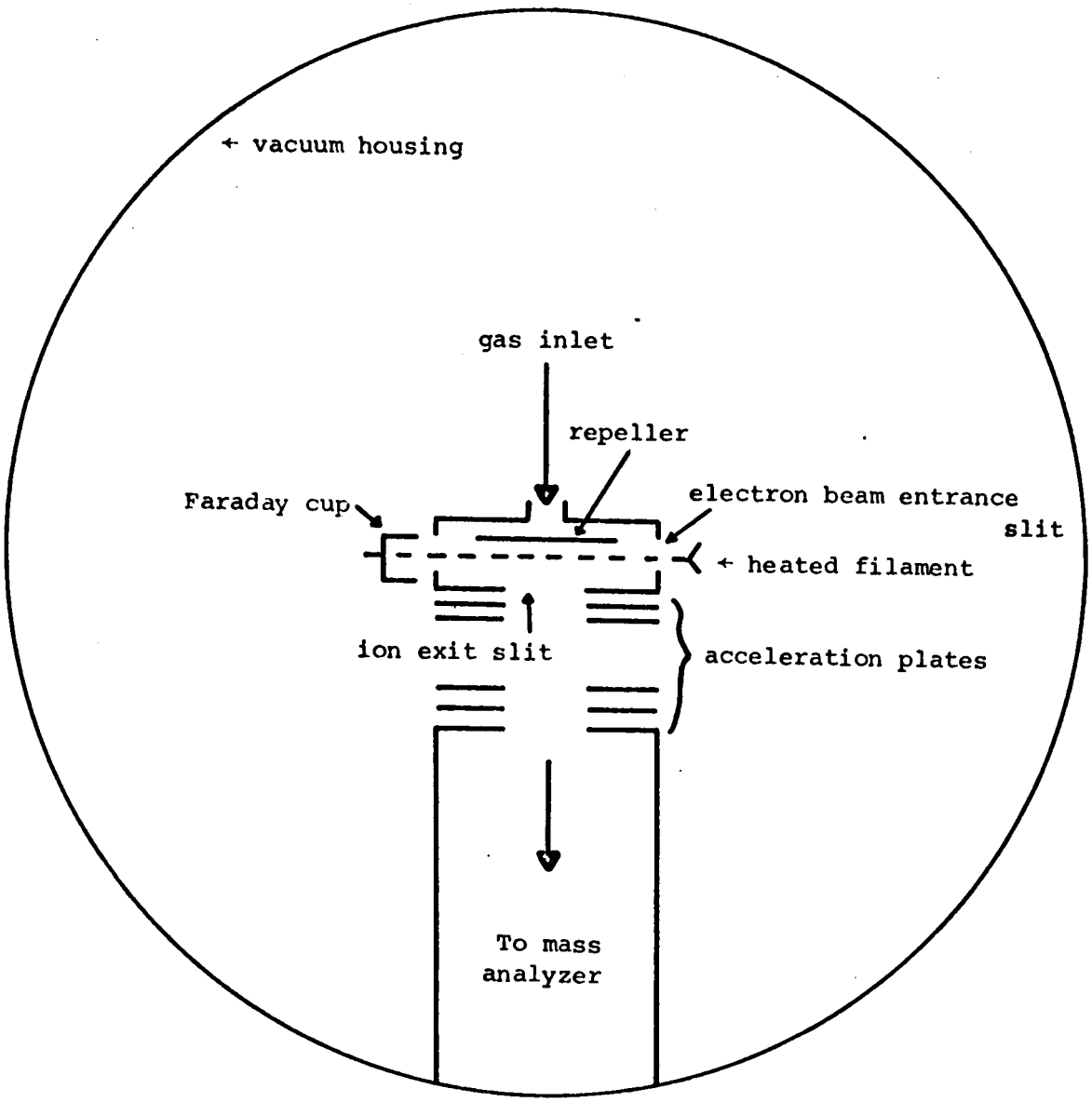

Figure 2.1 Partial view of a conventional mass spectrometer.

energy produced by the condensation reaction. The heat of solvation per condensation of one ligand is in the range 10-40 kcal/mole. If each collision removed half of this excess energy, approximately five collisions per condensation would be necessary to reduce the energy to RT for a temperature of 300°K. If the removal of excess energy is inefficient, the collision number will be higher. For a distance ℓ of 0.5 cm between the point of ionization of a molecule and the ion exit slit, an ion in a static gas undergoes 150 collisions at 0.1 torr. This is an approximate calculation from

$$2.1 \qquad \text{Collision No.} = \frac{\bar{v}\ \ell^2}{\lambda\ 2D}$$

where $\bar{v}$ is the ion velocity, λ is the mean free path of the ion and D is the diffusion coefficient (24). The diffusion coefficient was taken as 500 cm^2/sec as a representative ionic diffusion coefficient at 0.1 torr (25). The average velocity was taken for an ionic mass of 100 at 300°K and the mean free path was calculated from

$$2.2 \qquad \lambda = \frac{1}{\pi N d^2}$$

where N is the gas density and d is the average collision diameter of the two colliding species (26). d was assumed to be 5 A° by averaging the molecular diameter of water, 2.7 A° (27), and the ionic diameter of a typical hexahydrate,

8.0Å (28). Since the ion undergoes approximately 150 collisions at 0.1 torr, the ionic clusters are probably in equilibrium. To test the equilibrium assumption it is desirable to be able to vary the pressure by about a factor of ten i.e. to be able to increase the ion source pressure to 1 torr.

However, the mass spectrometer ion acceleration and mass analysis region must be maintained at less than 10^{-4} torr. Above this pressure the ion beam issuing from the ion source is seriously scattered by collisions. Thus a pressure differential of about 10^4 must be maintained between the ion source and the acceleration and analysis region outside the ion source. This can be achieved by high capacity pumping and by reducing the leakage of gas out of the ion source.

2.2 The High Capacity Pumping System

In the present instrument the total area of the ion source slits has been reduced by about a factor of 100 and the pumping speed at the ion source increased by about 100 over a conventional mass spectrometer. The gas was pumped through a six inch liquid nitrogen baffle and a six inch gate valve by a 1400 L/sec diffusion pump. The manufacturer rates the pumping speed at the entrance of the gate valve as 450 L/sec (29) for air. The reduction in pumping speed is due to the limited conductance of the baffle and valve. Conductances in series add according to equation 2.3

$$2.3 \qquad \frac{1}{F_t} = \sum_i \frac{1}{F_i}$$

where F_t is the total conductance and F_i is the conductance of each component. The reduced pumping speed S is given by

$$2.4 \qquad S = \frac{F_t \times Sp}{F_t + Sp}$$

where Sp is the speed at the diffusion pump (30). By comparison to the manufacturer's rated speed, the pumping speed at the ion source was measured as 350 L/sec for ammonia with the liquid nitrogen baffle uncooled. The speed is calculated from the pressure drop in the gas handling plant reservoir with respect to time and from the pressure in the vacuum housing (measured by an ion gauge). In this measurement the ion gauge pressure was 2.1×10^{-4} at an ion source pressure of 3 torr. Cooling the baffle with liquid nitrogen decreased the ion gauge pressure to 3.8×10^{-5} torr. This indicates a pumping speed increase to 1900 L/sec due to condensation of ammonia on the baffle.

From a knowledge of the pumping speed and the required pressure differential between the ion source and high vacuum region outside the ion source, the maximum gas conductance of the ion source can be calculated. From the equation

$$2.5 \qquad P_1 F = P_2 S$$

where P_1 is the ion source pressure, F is the conductance of the ion source exit slits, P_2 is the vacuum housing pressure,

and S is the pumping speed in the vacuum housing (30), the maximum conductance is 190 cm^3/sec. By equation 2.6

$$F = \frac{\bar{v} A}{4} \qquad 2.6$$

where $\bar{v}$ is the average velocity and A is the area of the slits (30), the maximum total area of the slits is about $10^{-2} cm^2$. The total area of the slits used was about an order of magnitude smaller. Because the ion current is also proportional to the slit area, the slit area cannot be too small lest no ion current be detected at the ion collector.

2.3 The Proton Generator

A. Principles of Operation

Another difference in the present instrument compared to a conventional mass spectrometer was that a 100 kev proton beam was used to ionize the gas in the ion source. The present mass spectrometer was equipped with a proton beam generator for two reasons. First, the ionization of atoms and molecules by fast protons could be studied. This study was completed by Collins (22). Secondly, a high energy beam is required to penetrate through the high pressures of gas in the ion source. At one torr ion source pressure, a 100 kev proton loses 3 kev through collisions in the ion source (31). These collisions result in ionizations and scattering of the proton beam. Use of a lower energy beam

would lead to greater scattering. This means that some of the ionization would occur closer to the ion exit slit and that some of the ions might not reach chemical equilibrium before passing out the ion exit slit.

A Cockcroft-Walton type proton generator, model number 100-1H, Texas Nuclear Corp., was used to supply a beam of 100 kev protons. Because the unit is described elsewhere (32), only a brief description is given here. Figure 2.2 shows the proton generator and mass spectrometer. The protons are created in a hydrogen discharge in a pyrex ion bottle shown in Figure 2.3. The pressure in the ion bottle, 10-100 millitorr, is regulated by a variable leak. A radiofrequency field applied to the two excitor rings ionizes the hydrogen. An extraction electrode, o-5 kv positive with respect to the accelerating potential repels the positive ions out of the bottle and attracts electrons. The electrons cause ionization and sustain the discharge. A longitudinal magnetic field supplied by a solenoid causes the electrons to spiral and ionize more molecules than the straight path.

Upon leaving the ion bottle the protons are focussed by a focus electrode, 0-10 kev negative to the accelerating potential. The beam travels through the accelerator (a series of ten electrodes), a magnetic field from a

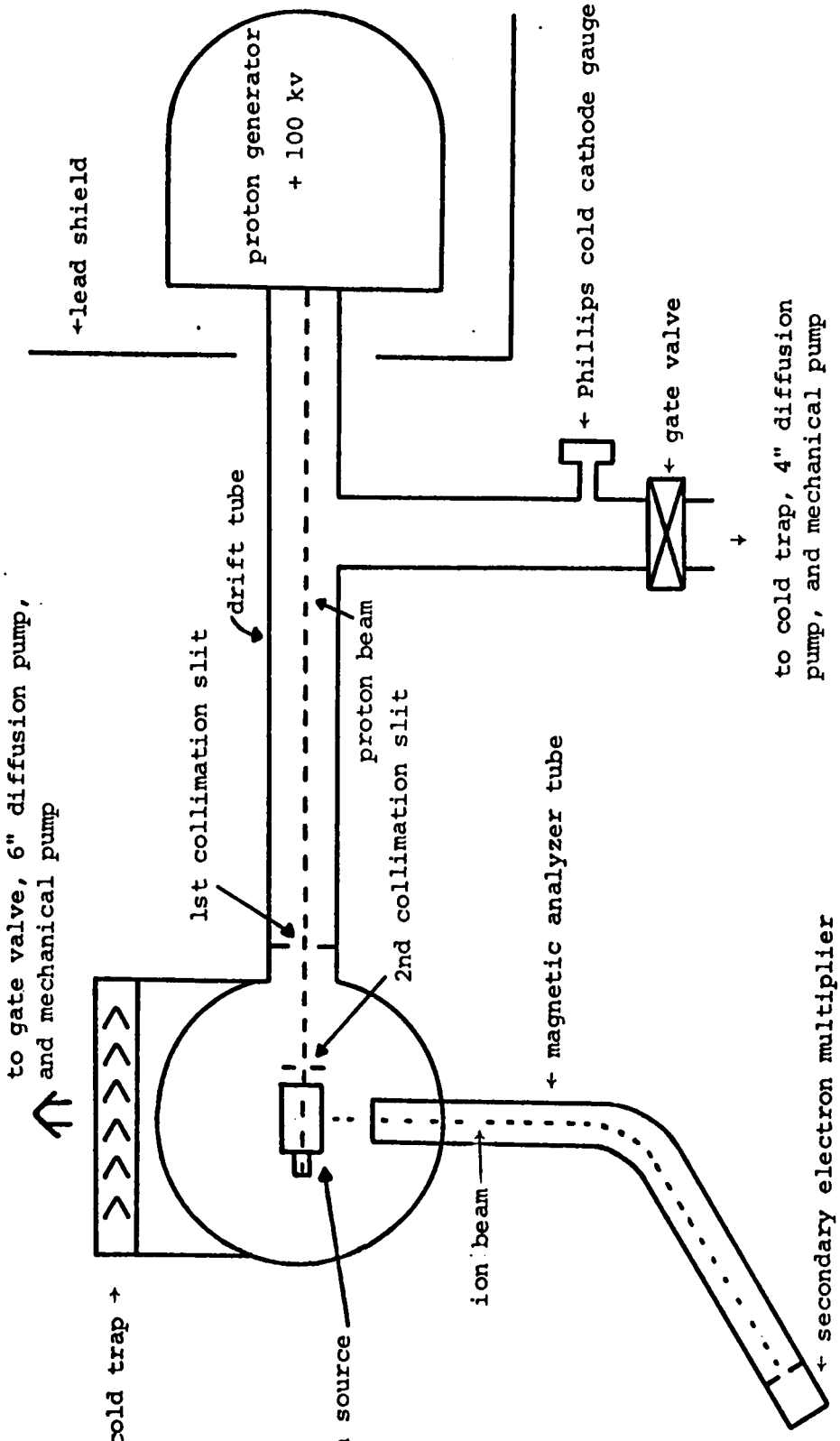

Figure 2.2 Schematic View of Present Apparatus

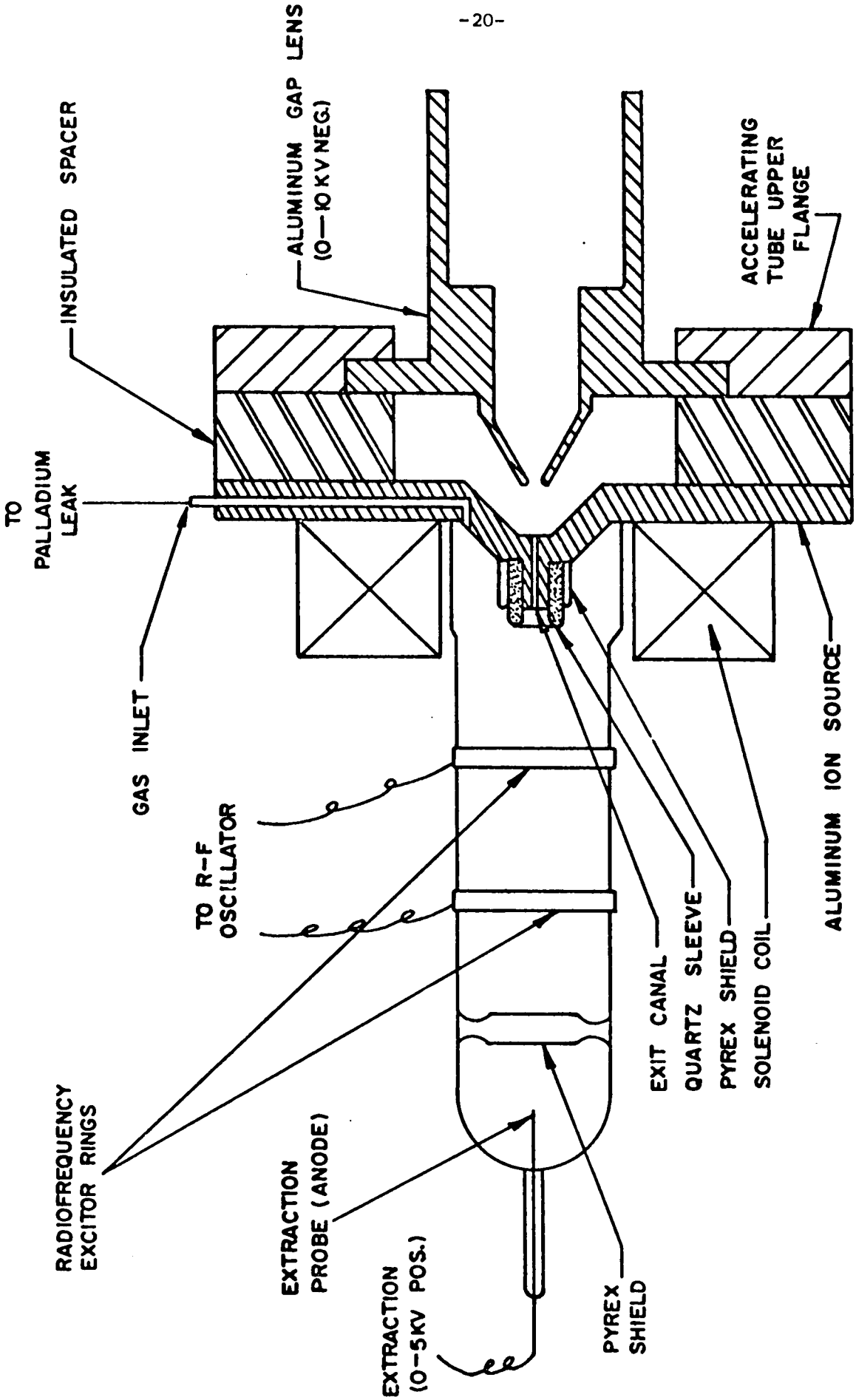

Figure 2.3 Ion bottle of proton generator.

permanent ring magnet, a meter long field free drift tube, and two collimation slits before reaching the mass spectrometer ion source. The magnetic field of the ring magnet which is perpendicular to the proton beam slightly deflects the beam. Adjustment of the ring magnet is used to position the beam onto the ion source proton beam entrance slit. The purpose of the collimation slits is to reduce the beam intensity incident on the ion source. The heat which must be dissipated from the beam is the product of the proton current times the proton accelerating voltage. Since the manufacturer claims a maximum current of 1500 μA (33), a maximum 150 W has to be dissipated. Since heat loss is by radiation and conduction only, a collimator could heat up considerably. The first slit was water cooled. The slit was located about 20 cm from the ion source and had dimensions of 3mmx5mm. The potential of the slit was earth potential. The second slit, which was positioned about 2 cm from the ion source, had dimensions of 0.5mmx3mm. Its potential was +225 v to the ion source potential. This potential collected the secondary electrons which were emitted when the proton beam impinged on the ion source. The presence of secondary electrons in the ion source makes the ionization of the gas in the source more complex. After passing through the ion source the beam is collected

in a Faraday cup. Ion source geometry will be discussed in a later section.

B. Operating Procedure

The effect of the proton beam controls on the proton beam current collected by the Faraday cup in the ion source is shown in Table 2.1. The extraction voltage could be varied over the range 0-5 kv while the focus potential could be adjusted from 0 to -10 kv. The potentials are relative to the proton accelerating potential of 0 - 100 kv. Although the accelerating potential was variable from 0 - 100 kv, all the present work used 100 kev protons.

The data in Table 2.1 indicates the extraction potential was most important in obtaining high proton beam currents at the ion source. The focus and solenoid controls could be left at zero volts and at zero current respectively. Changing the H_2 pressure over the range $1 - 2 \times 10^{-5}$ torr as measured by the Phillips cold cathode gauge varied the proton beam current by a factor of two.

The stability of the proton beam as indicated by the change in mass analyzed ion current with time was normally about $\pm 5\%$ over a 10 minute period. Generally about 10 minutes was required to scan over and measure the required mass analyzed ion currents. Because the stability was sometimes poorer, the first ion current measured was

TABLE 2.1

Effect of Proton Beam Controls on the Proton Current Striking the Faraday Cup of the Ion Source

I. Maximum Beam Conditions

Control	Control Setting	Faraday Cup Current
H_2 Pressure	1.2×10^{-5} torr (on the downstream Phillips cold cathode gauge)	
Extraction	+ 3900 v	
Focus	- 800 v	
Solenoid	0 A	1.9×10^{-7} A

II. Effect of Control Settings at 1.2×10^{-5} torr H_2 Pressure

A.	Focus	- 3200 v	
	Solenoid	0 A	
	Extraction	+ 3400 v	0.2×10^{-7} A
		+ 3600	0.7
		+ 3800	0.8
		+ 4000	0.8
		+ 4200	0.4
B.	Extraction	+ 3800 v	
	Solenoid	0 A	
	Focus	0 v	1.7
		- 400 v	1.7
		- 800	1.9
		- 1200	1.6
		- 1600	1.4

TABLE 2.1 (continued)

		Control Setting	Faraday Cup Current
C.	Extraction	+ 3800 v	
	Focus	- 800 v	
	Solenoid	0.0 A	1.9
		0.3	1.9
		0.6	0.2

always remeasured after the other ion currents were measured. If the two currents did not agree within ±5%, the mass spectrum was remeasured. Any change in the ion source such as temperature or pressure would also have affected the ion current.

C. Proton Beam Deflection Plates

To permit measurement of the ion source residence time of an ion, deflection plates were installed in the proton beam drift tube. A pulsed deflection of the proton beam coupled with a pulsed detection of the mass analyzed ions by a variable time delay can be used to determine the ion source residence time of an ion. From the initial change of ion current with time, the forward reaction rate constant can be determined. When equilibrium is reached, the relative ion currents become invariant with time. This allows calculation of both the equilibrium constant and the reverse reaction rate constant. The pulsing technique has been applied by many researchers (33) at low pressures to determine forward rate constants. At high pressures the technique has been applied to gas phase solvation reactions by Durden, Good and Kebarle (34).

The design of the deflection plates was based on equation 2.7 (the equation can be readily derived from fundamental laws and

$$y = \frac{V_{Defl.}\ \ell\ X}{2V_{ion}\ Y} \qquad 2.7$$

equation 11.5 of Ref. 35).

where y is the deflected distance at a target, X is the distance from the plates to the target, Y is the distance between the plates, ℓ is the length of the plates, V_{ion} is the voltage used to accelerate the ion to the deflection plates and $V_{Defl.}$ is the potential difference between the plates. The plates were made 1.2 cm apart and 19.6 cm long. The center of the plates was 40 cm from the ion source. The calculated deflection which was $3 \times 10^{-3} cm/V_{Defl.}$ agreed with the estimated experimental deflection. To observe the deflection, the second collimation slit, which is located 2 cm in front of the ion source, was coated with a phosphor. The proton beam image on the collimation slit was observed through a plexiglass window.

To make the voltage required to deflect the beam off the ion source entrance slit small enough to use a conventional pulsing unit, the first collimation slit was moved ahead of the deflection plates. The dimensions of the slit were reduced to 0.25 mm x 10 mm.

The observed image of the first collimation slit on the second collimation slit had a width of about 0.5 mm. Applying a static deflection voltage of 50v not only deflected the beam but also approximately doubled the slit image. In spite of this anomalous spread in the width of the proton beam, a 50 v pulsed deflection should be sufficient to produce a pulsed beam in the ion source.

D. X-ray Hazard

If secondary electrons ejected by the proton beam at the first collimation slit are incompletely suppressed, they may enter the stray positive field of the accelerator and be accelerated up to 100 kev. When these fast electrons strike a surface, X-rays are ejected. This is a normal hazard of the accelerator. Since the point of emission of secondary electrons was moved much closer to the accelerator with the installation of the deflection plates, a radiation monitor was used to remeasure the X-ray flux. The readings were similar to those taken previously. The meter read less than 0.01 mrh with the monitor facing the lead shield which surrounds the accelerator. The lead shield was an 1/8 inch thick and 6 feet high. Directly above the shield the monitor read 0.5 mrh. The weekly tolerable dose is 100 mr (36). As long as the accelerator is functioning properly, X-rays should not be a hazard.

2.4 Source of Potassium Ions

A. Introduction

Although the proton beam conveniently produced ions for the study of $H^+(H_2O)_n$ and $NH_4^+(NH_3)_n$, its use for the generation of K^+ proved to be impractical due to the reaction between water vapor and potassium vapor. For this reason it was necessary to generate potassium ions in a source

external to the ion source. An alternative method to ionization by a high energy beam is thermal ionization. The method depends on the fact that evaporation from a surface may occur as the evaporation of a neutral species or a positive ion. The relative probability of evaporation as a positive ion is given by the Langmuir-Saha equation (37)

$$2.8 \qquad \frac{n_+}{n_o} \propto \exp \frac{\phi - I}{kT}$$

where n_+ is the number of positive ions, n_o is the number of neutral particles, ϕ is work function of the surface, and I is the ionization potential of the neutral particle. Because $\phi - I >> kT$, thermal ionization sources operate at high temperatures. The sources which are used in mass spectrometric inorganic analyses operate at 2000°K (23). The difficulty in using a high temperature source of ions is that the source has to be sufficiently distant from the ion source so that the ion source does not heat up. (It was desired to study solvation equilibrium at temperatures as low as 250°K).

From a literature search for a suitable thermal ionization source and from some experimentation, it was decided to use a Kunsman source located in a housing which was gas tight to the ion source. See Fig. 2.4. The thermal ionization in the Kunsman source arises from a specially prepared filament. This set-up had several advantages. Because the operating

temperature was only about 800°K, the filament could be placed very close to the ion source. This meant that the electric field required to transport a sufficient supply of ions to the ion source could be low. Consequently the number of collisions in the ion source required to reduce the energy of the ion to thermal equilibrium is less. By comparison, the alternative to this arrangement is the placement of the Kunsman source at a distance from the ion source. The ions would then have to be accelerated through vacuum into the ion source through an entrance slit. Although this method reduces the heating of the ion source, experimentally this method was found to deliver an insufficient ion current to the ion source. The reason is that the entrance slit had to be very small to maintain the necessary high vacuum in the vacuum housing as discussed in Section 2.1. Even if a sufficient ion current entered the ion source, the potential energy of the incoming ion would have been an order of magnitude higher than with the present arrangement.

B. Manufacture of a Kunsman Thermionic Source

The manufacture of a Kunsman thermionic source is given in a review by Jenkins and Trodden (37). The first step was the fusion of a mixture consisting of 98% Fe_2O_3, 1% Al_2O_3, and 1% KNO_3. The KNO_3 can be replaced by any of the alkali nitrates in order to generate other alkali ions.

In the fused product the Fe_2O_3 was oxidized to Fe_3O_4. The product was ground to a powder before it was fused onto a Pt filament. The filament was made from a strip of Pt 1 mm wide and 2 cm long which was cut from a 0.001 inch thick Pt foil. The width should be uniform or the filament will have hot spots in it when the heating current is passed through. The Pt strip was spot welded to two nichrome studs which were spaced about 1 cm apart. Fusion of the powder onto the filament required special care because the melting point of the powder was close to the melting point of Pt. A layer of powder 1 mm high was first spread uniformly along the length of the filament. A torch provided with a special 3/4 mm hole tip was adjusted to give a fine intense flame. The powder was heated until it just began to melt and flow. Cycles of melting and cooling were used to prevent the Pt from melting. If the coating is not uniform over the filament surface, the surface temperature will be uneven and the ion emission reduced.

Reduction of the surface was the next step. The filament was placed in a glass chamber. The chamber was evacuated and filled with 3-10 torr H_2. The filament wattage was increased until the light emitted by the filament was just visible. The necessary wattage was 15-30W depending on the H_2 pressure. The surface was sufficiently reduced in about 30 min. A longer reduction period did not improve the filament emission.

After the reduction the filament wattage was decreased and the glass chamber pumped out. Increasing the filament wattage brought an onset of positive current at about 10W. The emitted current was collected on a plate with a negative bias. Increasing the wattage until the filament became dull red yielded a positive current of 1-2 μA. If the filament temperature was increased to a bright red, a maximum of 10 μA could be obtained. This high current however, lasted only about 20 min. after which the current dropped well below 1 μA. A high temperature during reduction was also found to be detrimental.

C. Utilization of the Kunsman Source

Figure 2.4 illustrates Sources I and II, the Kunsman sources used in the present work. The two sources were necessary to prove that the reactions were not in thermal disequilibrium due to the heating of the ion source or the gas in the ion source by the filament. (The effect of the different sources on the results is discussed in Section 5.4) Source II was similar to Source I except for location.

The heater current to the filament was controlled by two variable autotransformers in series and regulated by a constant voltage transformer. The constant voltage transformer received 110 V.A.C. from a 3000 v isolation transformer which was plugged into the mains, 110 V.A.C. The power required

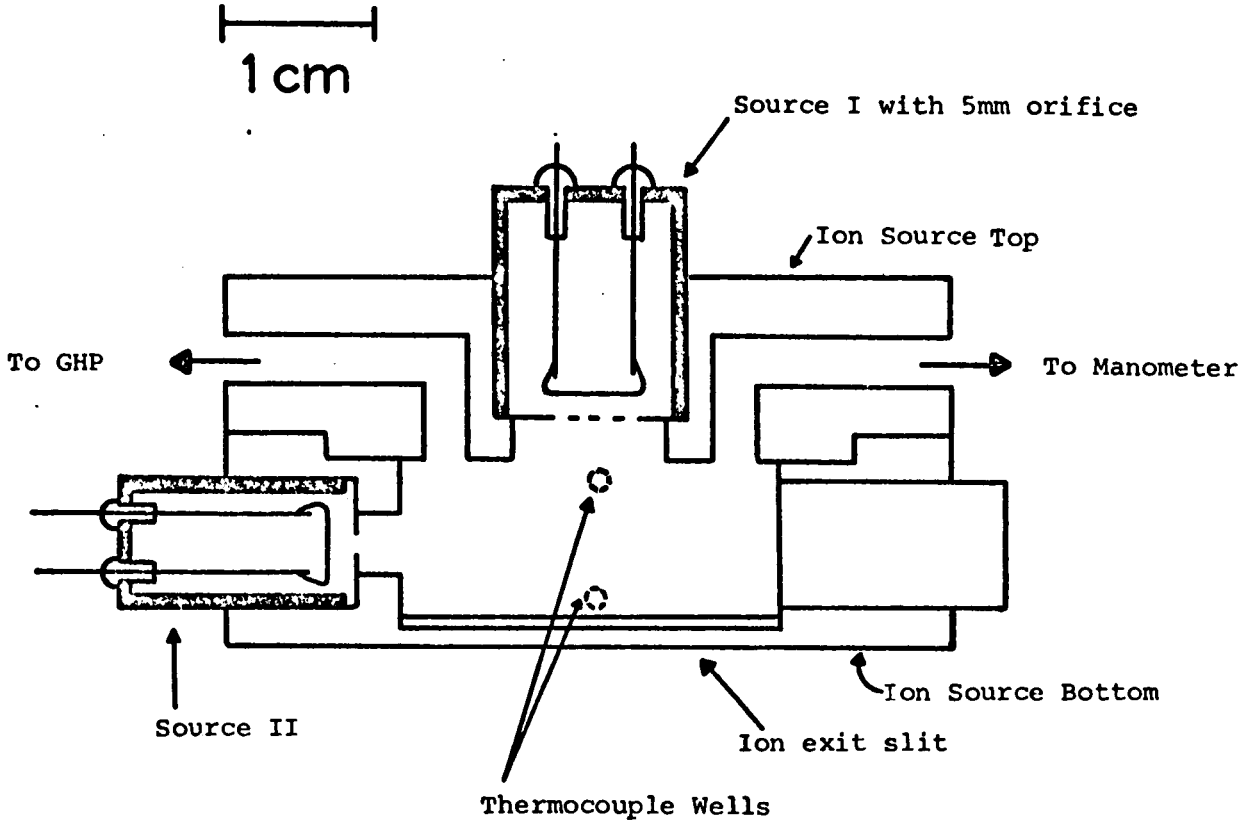

Figure 2.4 Kunsman Sources I and II of K^+ shown installed in the ion source.

to give a sufficient emission of ions from the filament at water vapor pressures up to 1 torr was about 20W.

Because the ions which were emitted by the heated filament diffuse rapidly to the wall, it was necessary to attract the ions to the ion source by a potential difference to obtain a detectable ion current after mass analysis. The potential difference was increased until the ion current after mass analysis was just adequate for accurate measurement. A potential difference of 10 v was found to give a sufficient ion current at all pressures in the ion source. Subsequently this potential was fixed at 10 v. or about 100v/cm for Sources I and II.

After the $K^+(H_2O)_n$ study was completed, research was begun on the $K^+(NH_3)_n$ system. Unlike the $K^+(H_2O)_n$ results, the $K^+(NH_3)_n$ results were affected by a variation in the filament wattage. To investigate the $K^+(NH_3)_n$ system, Source III was made. The $K^+(H_2O)_n$ results were then rechecked at 30°C and found to be in agreement with the previous results. Figure 2.5 shows the design of Source III. The filament was moved from 1 mm from the ion source to 20 mm. A ceramic insulator thermally and electrically isolated the filament housing from the ion source. Heat energy from the filament was reflected by a nichrome reflector backed by a copper plate which dissipated heat energy to the ion source.

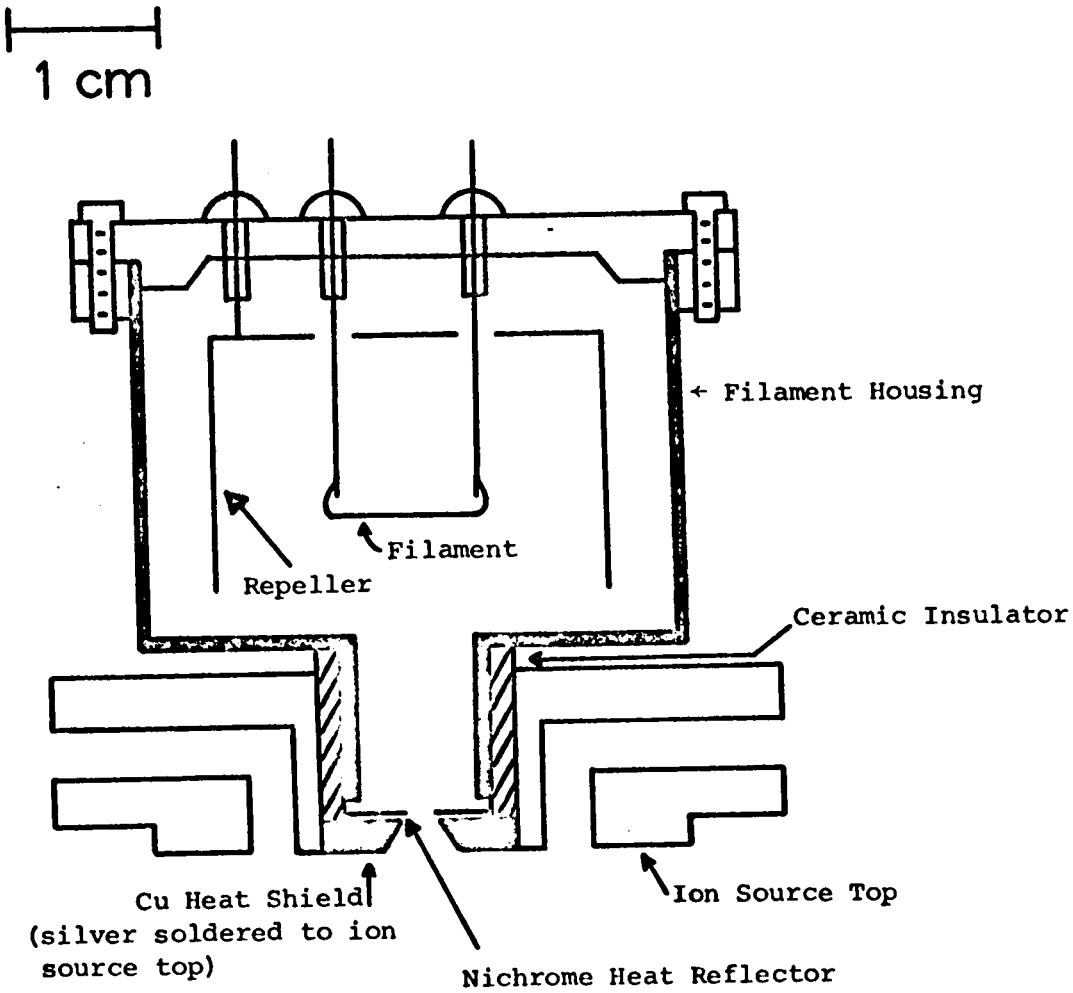

Figure 2.5 Kunsman Source III of K^+ shown with modified Ion Source Top.

Because the filament was farther from the ion source, the problem of obtaining a sufficient steady state concentration of potassium ions in the ion source was more difficult. Because the ion source was farther from the filament than the filament housing, the potential of the ion source had to be sufficiently lower than the filament housing potential to preferentially attract the potassium ions. To repel the ions diffusing away from the ion source, a repeller electrode was installed. Experimentally, the highest K^+ currents to the ion source occurred with the repeller electrode, filament housing, and filament at the same potential. A repulsive potential on the repeller electrode evidently lowered the emission of the filament while an attractive potential on the filament housing collected ions in the long narrow channel to the ion source. A potential of 225 v was necessary to attract a sufficient number of ions per sec. into the ion source. The electric field strength was approximately the same as the electric field strength as used with Sources I and II.

2.5 The Ion Source

The ion source in which the potassium ion clustering reactions occurred is shown in Figure 2.4. The purpose of the ion source was to provide a high pressure ion reaction chamber at a uniform temperature which could be varied over

a wide temperature range. The high pressure requirement was discussed in section 2.1. In that section the maximum total area of the ion source slits was calculated to be $10^{-2} cm^2$. Because the conductance of a slit increases when the mean free path of the gas is smaller than the slit width, it was desired to make the slit width less than 30 μ, the mean free path of water at 1 torr, 273°K. (38) (The increase in conductance is due to a transition from molecular flow to viscous flow (39).

One difficulty in making such narrow slits is that the thickness of foil at the slit edge must be less than the slit width or the ions will discharge themselves on the wall of the slit in passage through the slit. As a result the knife edges of razor blades were used to make the slits. The knife edges, after having been cut to the appropriate size, were placed over a slot, 1 mm x 4 mm, which was in the center of a support which bolted into the ion source.

To make the slit, one half of the slit was spot welded on the center line of the plate. The second half was placed in approximately the correct position and clamped in the spot welder. With a strong light behind the slit, the second half was adjusted until the two knife edges were parallel and the light coming through the slit appeared as a tiny crack.

When the geometry seemed satisfactory, a single spot

weld was made. If the geometry was satisfactory as viewed under a microscope which could measure distance to ±1μ, the spot welding was completed and the slit rechecked under the microscope. The greatest difficulty in the slit construction was vertical displacement. Often the slit had to be rejected because the plane of one slit was as much as 30μ above the other. The microscope could also measure depth. The dimensions of the ion exit slit were generally about 3μ x 4mm.

The finished ion exit slit was then bolted into the ion source. In the case of the experiments utilizing the proton beam, the ion source also had a proton beam entrance slit and collimation slit as illustrated in Figure 2.6. These slits were first made from Ta foil. However, after it was found that the Ta foil reacted with water vapor at high ion source temperatures, the slits were made from razor blades. The inner slit was 0.4 mm x 5 mm and the outer slit was 0.015 mm x 5 mm. The total area of the ion source slits was thus an order of magnitude less than the maximum permissible calculated in section 2.1. Because the vacuum housing pressure as measured by an ion gauge was about 3×10^{-5} torr at 1 torr ion source pressures at 298°K, the ion source could be operated at this high pressure without serious scattering of the ion beam issuing from the ion exit slit.

Besides operation at high pressure, the ion source had to have a uniform temperature. To obtain a uniform

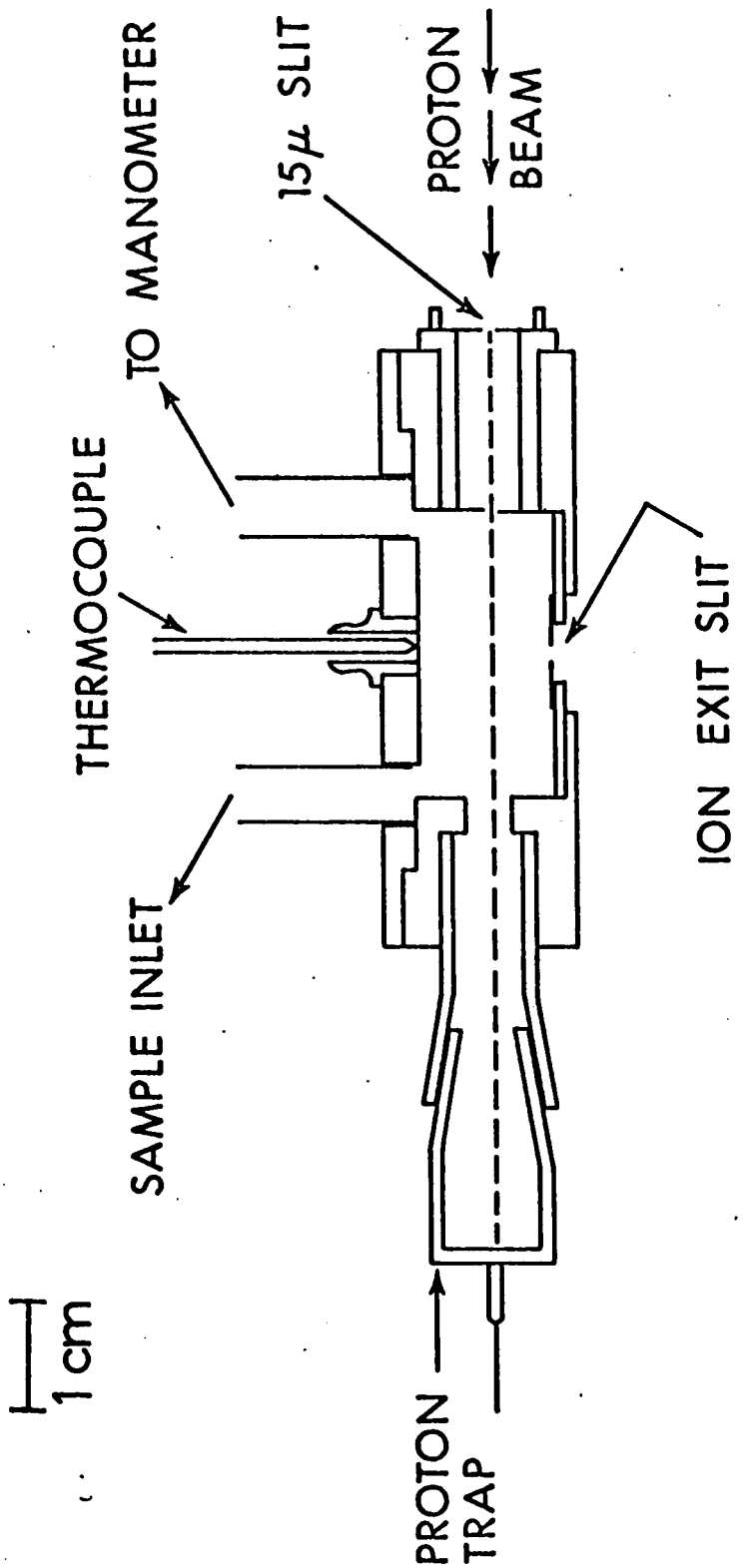

Figure 2.6a Ion Source used with proton beam. Side view.

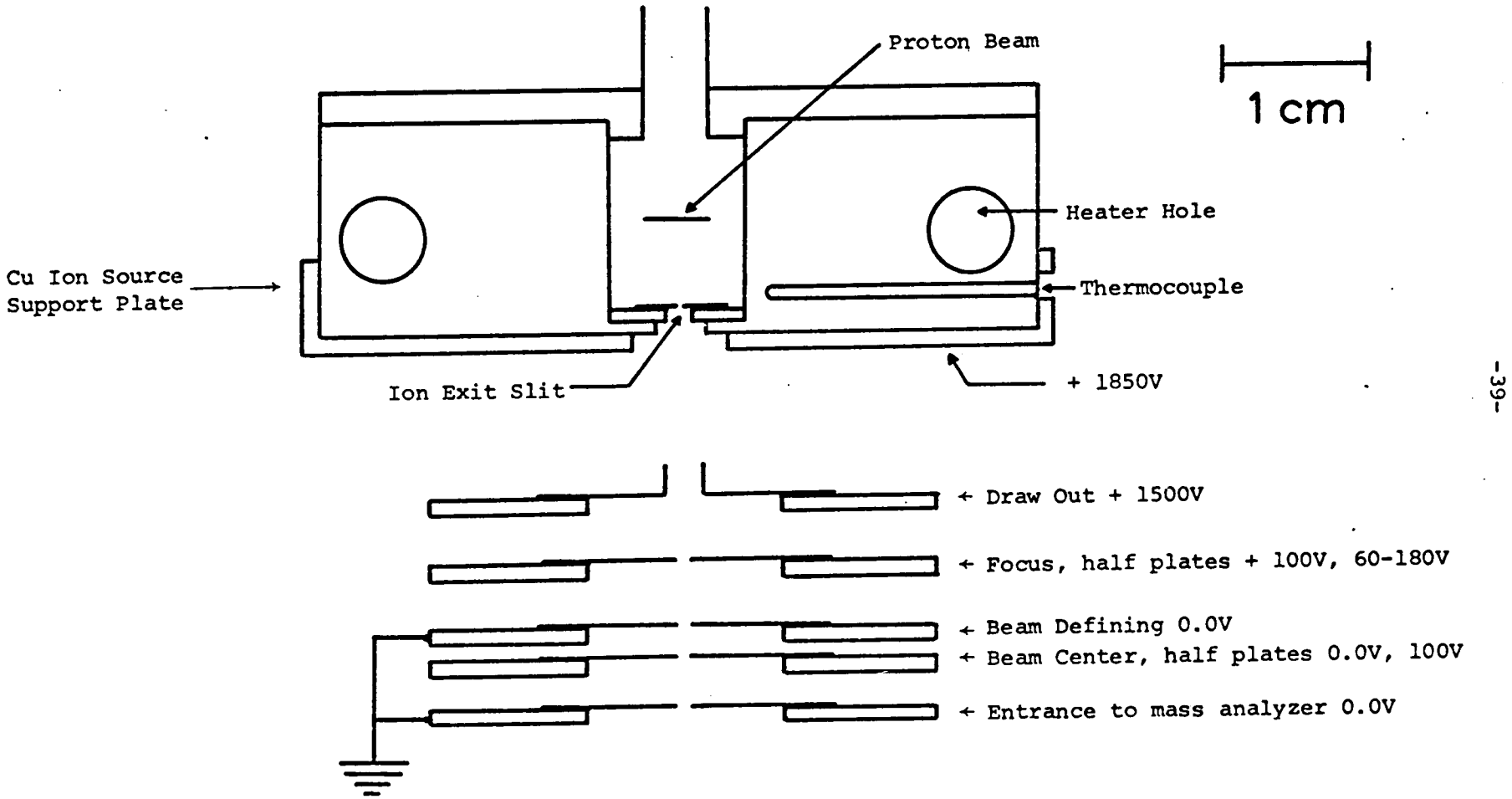

Figure 2.6b Ion Source and Acceleration Plates.

Ion Source Side View, 90° rotated from side view in Figure 2.6a.

temperature the ion source bottom was machined from a single stainless steel block. The heater holes were placed 1.5 cm from the ion source cavity to allow the heat flow to the cavity wall to be uniform. The ion source tops were carefully machined to give a good fit to the ion source bottom. The contact between the ion source top and bottom was improved by securely fastening the two parts together with four heavy bolts. The temperature control and measurement is discussed in sections 2.9 and 2.10.

2.6 Ion Acceleration, Mass Analysis and Measurement of Ion Current

In the high pressure ion source, ions arising either from the proton beam or the Kunsman source reacted to form ionic clusters. After these ionic clusters passed out of the ion source through the ion exit slit, they were accelerated from the ion source potential, +1850 v, to earth potential. Figure 2.6 shows the electrode system, which was a modified Nier design. The first electrode spacing to the ion source was increased from 1 mm to 10 mm. As discussed in detail in section 3.4, the shorter distance prevented the space around ion exit slit from being adequately pumped. The resulting high pressure caused the ionic clusters to undergo disequilibrium collisions outside the ion source.

After acceleration the ions entered the magnetic analysis tube and were deflected 60° to the ion collector. The magnetic analyzer tube entrance slit and exit slit were 0.500 inch x 0.010 inch and 0.500 inch x 0.020 inch respectively. The theoretical resolution is given by

$$\frac{m}{\Delta m} = \frac{R}{d_1+d_2} \qquad 2.9$$

where m is the highest mass which is fully resolved from m+1, R is the radius of curvature of the analyzer tube, 15 cm in the present instrument, and d_1 and d_2 are the analyzer entrance and exit slit widths (40). While the calculated resolution was 200 for the present instrument, the observed resolution was just slightly less.

After the ions passed through the analyzer exit slit, they entered the 17 stage secondary electron multiplier (SEM). In a SEM a positive ion is further accelerated by the potential of the first dynode. On striking the dynode, secondary electrons are ejected and accelerated to the second dynode where each electron ejects more electrons etc. The current amplification of this device is a function of the voltage across its dynodes. The approximate absolute gain is given in Figure 2.7. The gain was measured by collecting the positive ion current on the first dynode of the SEM by suitably changing the dynode potentials, i.e.,

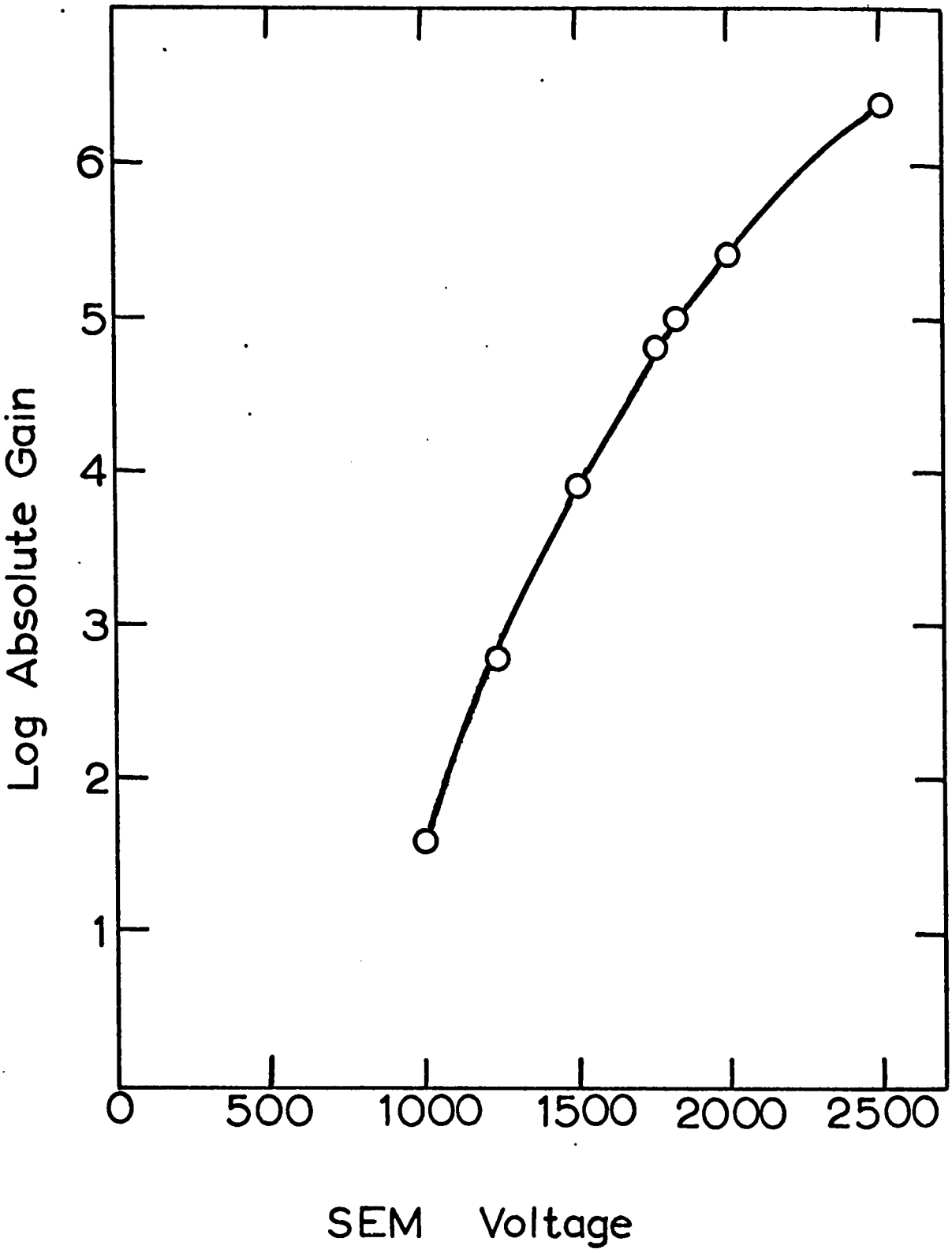

Figure 2.7 Absolute Gain of Secondary Electron Multiplier

the first dynode was at earth potential through its connection to the ammeter. The second dynode had a small positive bias to prevent the positive ions from passing from the first dynode to the second.

Normally there is a uniform potential drop between each dynode, the last dynode being at earth potential by its connection to the ammeter. The ratio of the electron current from the 17th dynode of the SEM to the positive ion current collected from the first dynode is the absolute gain of the SEM. The currents were measured by a Victoreen Femtometer with a 10^{10} ohm input resistor.

2.7 Gas Handling Plant

Introduction of gas into the ion source of the mass spectrometer was done by the gas handling plant (GHP). Figure 2.8 shows the glass reservoirs, valves, mercury manometers, and leaks which made up the GHP. Gases were admitted through a 12/30 ℧ ground glass connection. The valves were a combination of teflon gasketed metal valves and vacuum cup glass stopcocks. Dow Corning grease was used on the glass stopcocks. The system was pumped through a cold trap by a 10L/sec mercury diffusion pump backed by a Welch Duo-Seal forepump.

The handling of water and ammonia was done differently. The ammonia was admitted to the GHP from a tank of anhydrous

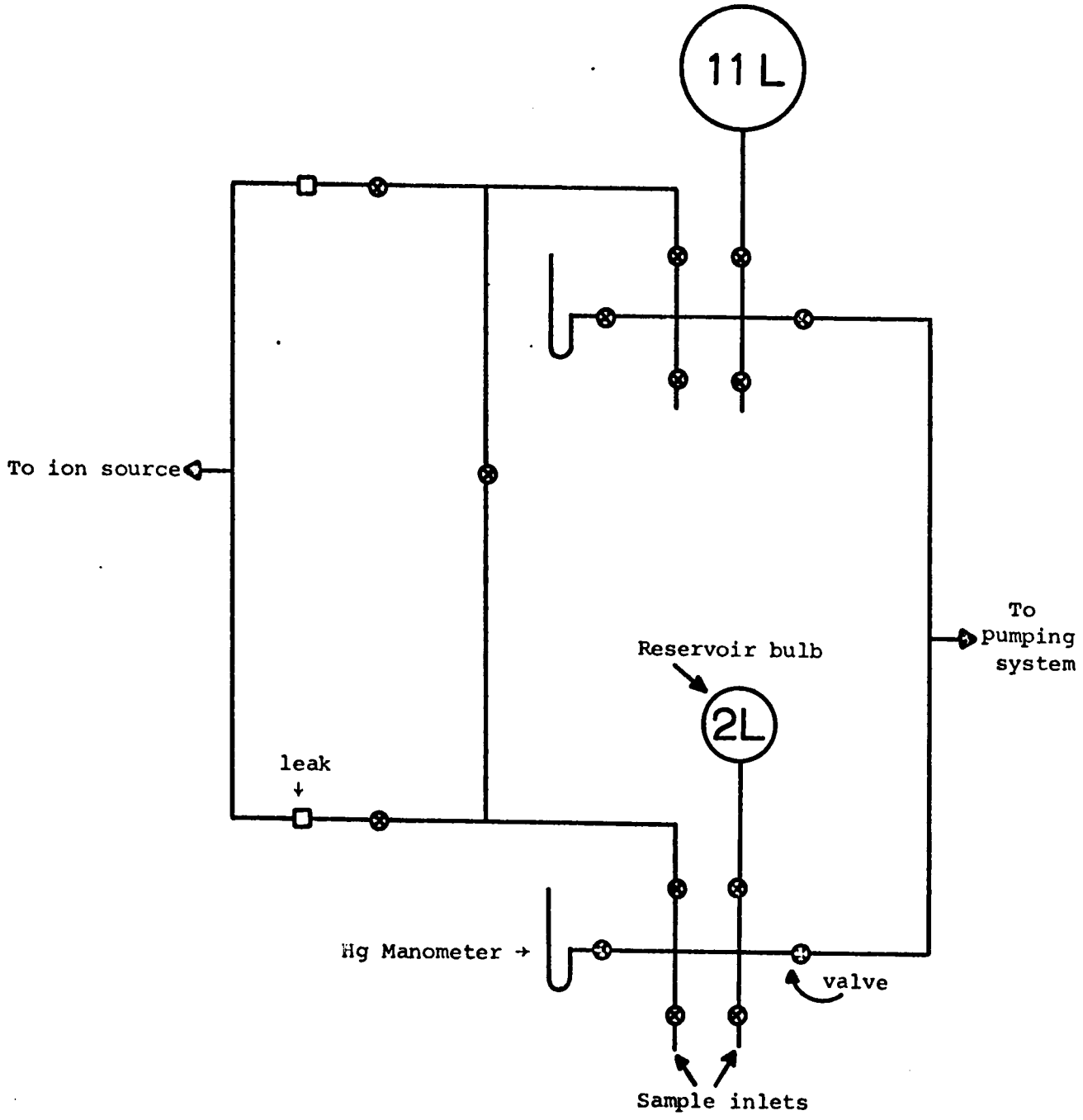

Figure 2.8 Gas Handling Plant for introduction of gases into the ion source.

ammonia. The gas was stored in the 2L and 11L reservoirs and in a 1L bulb which was connected to the GHP. Air was removed by condensing the ammonia in the cold finger of the 1L bulb and pumping off the non-condensable gases.

The ammonia was admitted to the ion source of the mass spectrometer through the 150 Lusec leak*. The leak not only drops the reservoir pressure but also prevents a discharge from the ion source (+1850 v) to a grounded part of the GHP. The pressure in the ion source was varied by changing the ammonia reservoir pressure by condensation of ammonia in the cold finger of the 1L bulb.

In handling water vapor, a gas bulb filled with about 50 ml of degassed doubly-distilled water (liquid) was used as a constant pressure source of water vapor. Temperature control of the bulb by a dewar filled with water or ice-salt mixture varied the water vapor pressure. The vapor was admitted to the ion source by the 70-100μ sintered glass leak (a high conductance leak).

2.8 Measurement of Ion Source Pressures

In earlier work a McLeod gauge had been used to measure the ion source pressure. Since McLeod gauges are suitable only for non-condensable gases, a dibutyl phthalate manometer was used in the present work. Because there was a pressure drop along the gas inlet line between

*One Lusec is one liter-micron/sec.

the GHP leak and the ion source, the dibutyl phthalate manometer had a separate line to the ion source.

When the present work was started, the dibutyl phthalate was degassed by refluxing it under vacuum. To obtain accurate pressure measurements a cathetometer was used to read the height difference to ±0.1 mm which corresponds to ±0.0077 torr ion source pressure. Because ammonia slowly outgassed from the dibutyl phthalate in the manometer arm under vacuum, the vacuum arm was continuously pumped.

2.9 Temperature Control of the Ion Source

Ion source temperatures above room temperature were achieved by two heaters located in the heater holes shown in Figure 2.6. Each heater was made by winding a 0.010 inch diameter Mo wire around a quartz rod and placing the rod and wire coil inside a 5 mm diameter quartz tube. About 30W was needed to heat the ion source to 400°C and 60W was needed to reach 600°C.

For ion source temperatures less than room temperatures, two different cooling methods were used. During the low temperature measurements on the $H^+(H_2O)_n$ and $NH_4^+(NH_3)_n$ systems, the ion source cooled itself by a net radiation loss to the liquid nitrogen baffles. One of these baffles was the one leading to the diffusion pump and

the other was a specially made baffle consisting of a liquid nitrogen reservoir attached to a cylindrical copper surface. Together the baffles virtually surrounded the ion source. Temperature control was possible by passing only a very small current through the heaters.

In the $K^+(H_2O)_n$ studies the cooling method was changed. The heaters were removed and the heater holes in the ion source were used as cooling channels of a circulatory system. Two Kovar seals were soldered to the two heater holes on the same face of the ion source. Each of these seals were glassblown to glass tubing which led out of the vacuum housing through "O" ring seals.

To complete the ion source circulatory system copper tubing was connected to the remaining open ends of the heater holes. Finally the system was checked for vacuum tightness. Either water or acetone was circulated through the ion source by a Colora Ultra-Thermostat which regulated the bath temperature to $\pm 0.01°C$. To achieve temperatures below 0°C, the bath was filled with acetone and cooled with a 2L stainless steel beaker which was filled with dry ice. The depth of beaker immersion in the bath varied the temperature to as low as -77°C. The temperature in the ion source, however, went only to -50°C.

2.10 Ion Source Temperature Measurement

The temperature of the ion source was measured by iron-constantan thermocouples made from number 30 A.W.G. wire. The small diameter wires, 0.010 inch, were used to prevent an erroneous reading due to heat conduction along the wire. The locations of the thermocouples are given in Figures 2.4 and 2.6. In the ion source used with the proton beam, the thermocouples were placed in wells as shown in Figure 2.6. Since the distance from the bottom of each well to the ion source wall whose temperature was desired to be measured was about 0.5 mm, the arrangement was changed before the $K^+(H_2O)_n$ study was begun. To obtain a more accurate measurement of the ion source temperature at the wall, the existing thermocouple well in the ion source bottom was drilled through to the ion source cavity and capped by a piece of 0.005 inch thick nichrome sheet which was spot welded to the wall. A second thermocouple well as shown by Figure 2.4 was made in the same manner.

The thermal emf was measured relative to a 0°C reference thermocouple by a Honeywell potentiometer. The temperature of the thermocouple could be read to within 1°C.

3. ION SAMPLING IN THE HIGH PRESSURE MASS SPECTROMETER

In this research project the thermodynamic functions, $\Delta G°$, $\Delta H°$, and $\Delta S°$ for gas phase solvation reactions were measured. This required a knowledge of the relative ionic concentrations in the ion source. In this section the general events such as ionization, recombination, and diffusion which affect the ionic concentrations are described. In addition the possible relative changes in the ionic concentrations occurring in sampling and measurement are discussed. In general these possible changes alter the ion ratios and therefore affect $\Delta G°$ and $\Delta S°$ but not $\Delta H°$.

3.1 General Reactions in the Ion Source

A. Reactions Initiated by the Proton Beam

Thermal energy ions for the study of $NH_4^+(NH_3)_n$ and $H^+(H_2O)_n$ equilibria were created by the processes given in Table 3.1. The irradiated gases and beam energies shown in the table are not the same as those used in the present experiments since information pertinent to this work is not available in the literature. However, the literature data are sufficiently representative to provide a qualitative picture of the processes to be expected in the present system in which water or ammonia vapor was irradiated by 100 kev protons. Since each 100 kev particle undergoes more than one collision at the high pressures used, reactions 3.3, 3.4, and 3.5 occur in addition to reactions 3.1 and 3.2.

TABLE 3.1

Reactions of a High Energy Beam

	Reaction*	Energy kev	Total Cross Section A^2	Reference
3.1	$\vec{H}^+ + N_2 \longrightarrow [N_2^+] + \vec{H}^+ + e$	100	6	1
3.2	$\vec{H}^+ + N_2 \longrightarrow [N_2^+] + \vec{H}$	100	3	1
3.3	$\vec{H} + O_2 \longrightarrow [O_2^+] + \vec{H}^-$	30	0.3	41
3.4	$\vec{H} + O_2 \longrightarrow [O_2^-] + \vec{H}^+$	30	3	41
3.5	$\vec{H}^- + Ar \longrightarrow Ar + \vec{H} + e$	40	20	42

* The bracketed products represent the sum of all the low energy ion products i.e. N_2^+, N^+, O_2^+, O^+, O_2^-, O^-.

The thermal energy ions created by the high energy beam diffuse to the walls of the ion source where they are discharged. En route to the wall the ions react to form solvated hydrogen ions. Some of the ions undergo recombination with the electrons or negative ions created by the processes represented by reactions 3.1, 3.4, and 3.5.

To calculate the approximate steady state concentration of the positive ions, it is necessary to know the composition of the beam and the cross sections for reaction. Since these facts are not well known, the approximate steady state concentration of the thermal energy ions cannot be calculated with any accuracy. One can estimate, however, that about 10^{12} positive ions/sec are created at 1 torr pressure, 298°K in the plane of the high energy beam directly above the ion exit slit whose length is 4 mm. The ion production calculation assumes a cross section of 3Å^2 and uses a beam intensity corresponding to the proton beam current, 0.05 μA, measured in the Faraday cup of the ion source at background pressure. Under these conditions, each high energy particle undergoes about 10 collisions per centimeter path length.

Since the steady state concentration of positively and negatively charged particles may be high in the ionization region, recombination may be a major loss of ions in this region. However, since there is a long path length, 0.5 cm to the ion exit slit, recombination in the narrow ionization region should not affect the relative ionic

cluster concentrations at the exit slit.

B. Production of the Solvated Potassium Ion

To produce potassium ions for the study of hydrated potassium ions, a heated filament was utilized rather than the proton beam. Consequently the initial reactions are different. The potassium ions after having been ejected from the heated filament were attracted to the ion source by an electric field of approximately 100v/cm. The high field was required to attract a sufficient flow of ions into the ion source to allow ion current measurement after mass analysis. Upon entering the field free ion source the potassium ions had excess translational energy i.e. energy greater than thermal energy.

Because the filament chamber operates at the same pressure as the ion source, the translational energy of the potassium ion can be calculated by Wannier's equation (43),

$$3.1 \qquad E_{ion} = \frac{1}{2} (m_{ion} + m_{neut.}) V^2 + {}^3/2\ kT,$$

for the translational energy of an ion at low X/P where X is the electric field strength, P is the pressure, and V is the drift velocity of the ion.

The ion drift velocity can be calculated from the mobility, the drift velocity per atm - v/cm. Munson, Tyndall, and Hoselitz (44) have measured the mobility of K^+ in the rare gases with up to 2.8% water vapor added at X/P up to

30v/cm - torr. For values of X/P from 0 to 10 v/cm - torr, the mobility was constant. Above 10v/cm - torr, the mobility increased with increasing X/P. The effect of increasing the percentage water vapor was the extension of the constant region of the mobility. Assuming the constant region extends to 100 v/cm - torr at 100% water vapor gives a value of the mobility of 2.2 $cm^2\ sec^{-1}\ v^{-1}\ atm^{-1}$ by extrapolating the data for the mobility of K^+ in moist Ar. Under the experimental conditions of 100 v/cm - torr the drift velocity is then 1.7×10^5 cm/sec. On substitution of the drift velocity value into equation 3.1, the potassium ion energy is 0.74 ev. This means about six collisions are required in the ion source to remove the excess translational energy assuming each collision removes half of the excess energy.

The maximum depth to which an ion penetrates into the ion source can be calculated from the mean free path. The formula for the mean free path λ is

$$\lambda = \frac{1}{\pi N_B (\frac{1}{2}\sigma_A + \frac{1}{2}\sigma_B)^2} \qquad 3.2$$

where N_B is the neutral gas density, σ_A is the collision diameter of the ion and σ_B the collision diameter of the gas molecule (26). Taking σ_A as 2.66Å for the ionic diameter of K^+ (45) and σ_B as 2.72Å for the diameter of the water molecule (27) gives λ equals 0.01 cm at 1 torr, 298°K. At

1 torr the penetration of the unsolvated ion into the ion source is less than 1 mm. At 0.1 torr the penetration increases to 8 mm as calculated by the above considerations. These distances can be compared to the 1.6 cm distance from the potassium ion entrance orifice which is in the ion source top to the ion exit slit. Thus, even at the lowest pressures used, the path length at which the ion is at thermal energy is 3 mm longer than the path length in the study of the $H^+(H_2O)_n$ and $NH_4^+(NH_3)_n$ systems.

3.2 Transport of the Solvated Ions Out of the Ion Source

After the potassium ions lose their excess energy and, in the case of the ions created by the proton beam, after the ions are created, the ions react with neutral molecules as they diffuse toward the wall. During this time the ions should form equilibrium ionic clusters. The average distance traversed by an ion along an axis X is given by

$$\overline{\Delta X^2} = 2Dt \qquad 3.3$$

where $\overline{\Delta X^2}$ is the average mean square displacement, D is the diffusion coefficient, and t is the time of diffusion (24). Setting $\overline{\Delta X^2} = X^2$ as an approximation gives upon rearranging

$$t = \frac{X^2}{2D} \qquad 3.4$$

Substitution of 0.5 cm, the distance between the proton beam

plane and the ion exit slit, for X and taking 50 cm^2/sec as a representative diffusion coefficient at 1 torr, 298°K (25) leads to a diffusion time to the ion exit slit of 2.5 millisec. This time is also an estimate of the ion source residence time of an ion. This estimate is approximate since space charge effects due to presence of the charged particles may alter the diffusion coefficient.

The calculation applies to a static gas. In the ion source the gas flows out the ion exit slit. The flow rate can be approximately calculated by modifying an equation for the flow out of a circular orifice (46). The flow rate is derived from

$$F = -A \frac{dr}{dt} \qquad 3.5$$

where F is the conductance of the slit, A is the area of the hemicylindrical surface illustrated in Figure 3.1 and dr/dt is the flow velocity at a distance r from the center line of the ion exit slit. On substitution for the area and rearrangement, one obtains equation 3.6

$$\frac{dr}{dt} = \frac{-F}{\pi l r} \qquad 3.6$$

where l is the length of the slit. From equation 2.6 the conductance of the ion exit slit is 2 cm^3/sec for a molecular mass of 18, 298°K and slit dimensions of 3μ x 0.4 cm. Use of equation 3.6 indicates that although the gas is flowing,

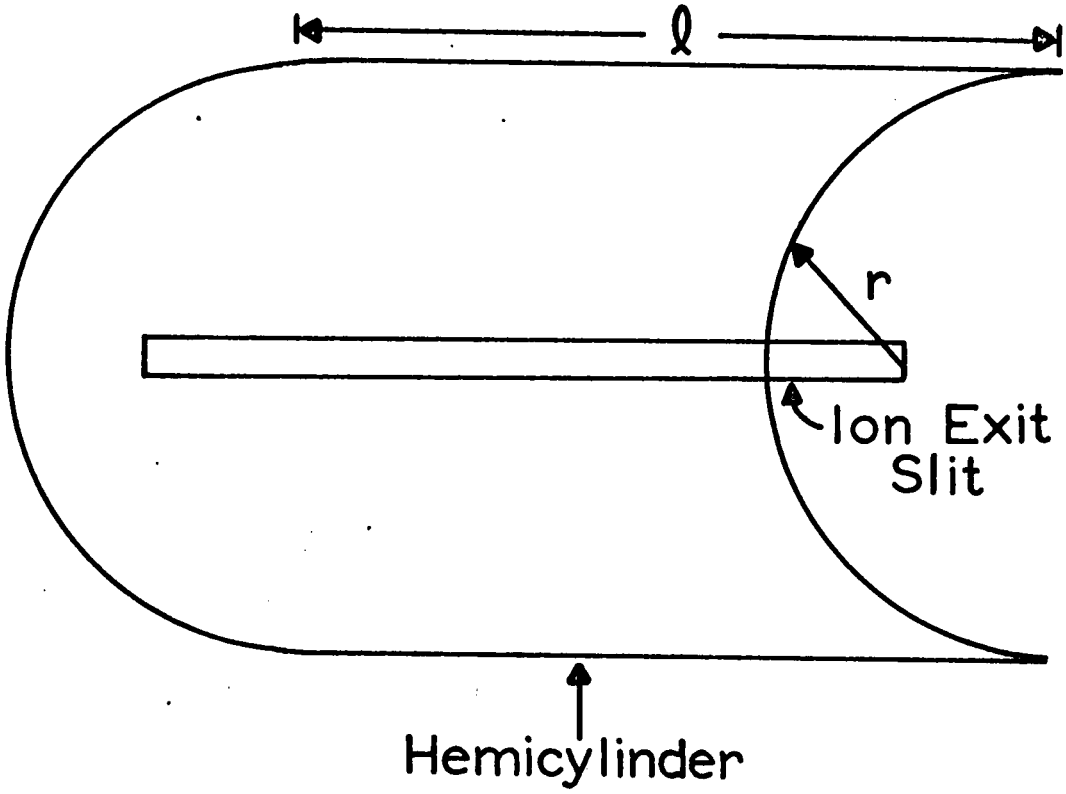

Figure 3.1 Assumed Gas Flow in the Ion Source.

the rate does not become significant (100cm/sec) until about 1 mm from the exit slit. The ion residence time is, therefore, not greatly shortened due to the gas flow.

The major transport of ions then occurs by diffusion. Since the diffusion coefficient is inversely proportional to the molecular mass, ions of lower mass should have a lower ion residence time. This increases the observed per cent total ionizationof the low mass ions. However, if the equilibrium ionic clusters rapidly gain and lose ligands (i.e. fast forward and reverse reaction rates), all ions will have the same average molecular mass. The diffusion process thus need not give a discrimination in the ion sampling process.

One process that may give a discrimination is the passage of ions out of the exit slit. By equation 2.6 low mass ions are favored to exit the ion source. However, the high gas flow rate at the ion exit slit may tend to lessen this discrimination. By equation 2.6 the flow rate at the slit is $1.5 \cdot x\ 10^4$ cm/sec for molecular mass 18, 298°K.

3.3 Collisions Outside the Ion Source

After the ions and gas molecules have emerged from the ion source, any ion-molecule collisions will lead to non-equilibrium. This problem was encountered by Collins (22)

in a preliminary study of the equilibrium reaction

$$3.6 \qquad H^+(H_2O)_{n-1} + H_2O \rightleftarrows H^+(H_2O)_n.$$

Collins found that the ion cluster size began to decrease after a pressure of about 0.3 torr due to ionic cluster-water molecule collisions outside the ion source. Dissociation occurred if a collision occurred since the ionic cluster was electrically accelerated upon leaving the ion source. Since a larger hydrate has weaker ion-ligand bond strengths and may have a larger collision cross section, the larger hydrates were preferentially dissociated. The extraneous collisions were eliminated by increasing the pumping speed at the ion exit slit. The pumping speed at this point was limited by the low gas conductance caused by the close spacing of the ion source and the first accelerating electrode. To improve the conductance, the first accelerating electrode was moved from a distance of 1 mm from the ion source to a distance of 10 mm. Because the conductance is proportional to the distance squared for this pumping geometry (22), the conductance was 100 times greater. Figure 3.2 compares Collins' results with the results from this work.

As shown in Chapters 4, 5, and 6, the calculated equilibrium constants did not change with pressure up to some maximum pressure P after which the equilibrium constant began to decrease. Evidently at higher pressures dis-equilibrium collisions again become significant.

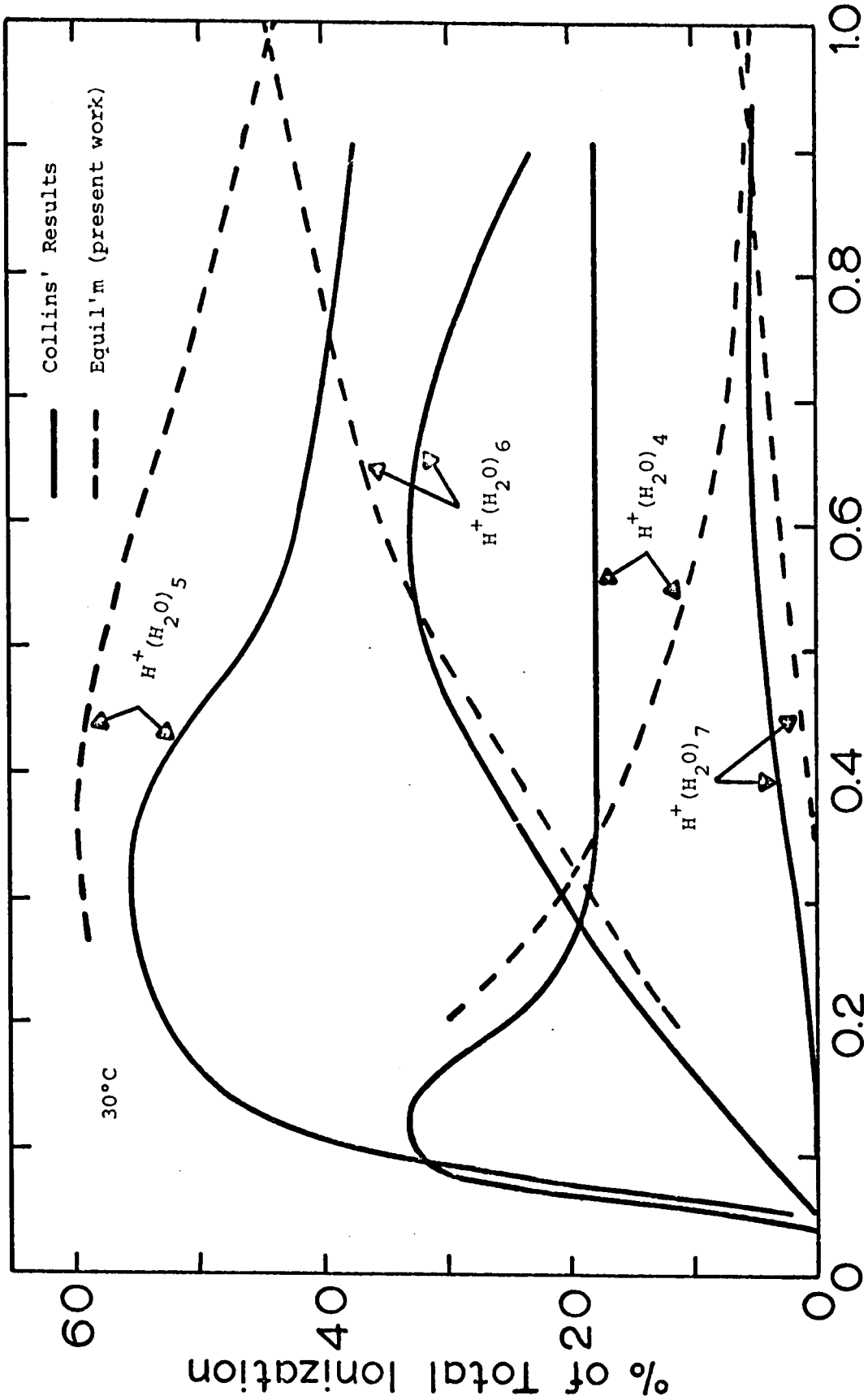

Figure 3.2 Comparison of Collins' results with present results at 30°C. The discrepancy between the results at higher pressures is due to non-equilibrium collisions outside the ion source under Collins' conditions.

At higher temperatures it was found that this maximum pressure P increased. This may be partly due to fewer molecules/sec effusing out of the ion source. As the temperature is increased, the conductance, vol/sec increases by $T^{\frac{1}{2}}$ by equation 2.6 but the molecules/sec effusing out of the ion source per sec decreases by T^{-1} by the ideal gas law. In addition, the cluster sizes are smaller at higher temperatures and so the cross sections are expected to be smaller.

3.4 Ion Discrimination in Acceleration, Mass Analysis and Detection

In the preceding sections some of the possible pitfalls in the ion sampling were described. In addition the mass spectrometer itself can alter the ion ratios. During the ion acceleration either high or low mass ions may be discriminated against. The fact that two mass spectrometers, the proton beam mass spectrometer (operated by A. Zolla and the author) and the alpha particle mass spectrometer (20)(operated by M. Arshadi and J. Scarborough), with two very different sets of acceleration electrodes gave similar results from the study of reaction 3.6 suggests that the discrimination in ion acceleration was not very important.

Discrimination may also occur in the secondary

electron multiplier. The number of electrons ejected from the first dynode by the impacting ion can vary with the ion velocity. To measure the SEM discrimination the relative gain of the SEM was measured for two series of solvated ions. The procedure is given in Section 2.6. From these measurements the relative gains for $H^+(H_2O)$, $H^+(H_2O)_2$, $H^+(H_2O)_3$, and $H^+(H_2O)_4$ were (1.0), 1.1, 0.8, and 0.8 respectively. For $NH_4^+(NH_3)$, $NH^+(NH_3)_2$, and $NH_4^+(NH_3)_3$ the relative gains were (1.00), 0.95 and 0.95 respectively. In the case of the $K^+(H_2O)_n$ series the ion currents were too small to measure directly. However it appears that the SEM introduces a maximum discrimination of 20% in the measurement of ionic clusters.

4. RESULTS AND DISCUSSION OF THE HYDRATION OF K^+ AND COMPARISON OF RESULTS TO ELECTROSTATIC CALCULATIONS

4.1 Introduction

Potassium ions which are ejected by a heated filament drift into the ion source under the influence of an electric field. In the field free ion source the potassium ions lose their excess translational energy and react with water molecules by the following reactions:

4.1 (0,1) $$K^+ + H_2O \xrightarrow{M} K^+(H_2O)$$

4.2 (1,2) $$K^+(H_2O) + H_2O \xrightarrow{M} K^+(H_2O)_2$$

4.3 (n-1,n) $$K^+(H_2O)_{n-1} + H_2O \underset{\longleftarrow}{\xrightarrow{M}} K^+(H_2O)_n$$

Since the attachment of a water molecule to an ion is exothermic, third bodies, which are indicated above as M, are required for the removal of excess energy.

The equilibrium constant for the general reaction is given by equation 4.1 where $I_{K^+(H_2O)_n}$ and $I_{K^+(H_2O)_{n-1}}$

4.1 $$K_{n-1,n} = \frac{I_{K^+(H_2O)_n}}{I_{K^+(H_2O)_{n-1}} P_{H_2O}}$$

are the mass analyzed ion currents. The ion currents are assumed proportional to the corresponding equilibrium concentrations of $K^+(H_2O)_n$ and $K^+(H_2O)_{n-1}$ in the ion source. Determination of $K_{n-1,n}$ at different temperatures is used to obtain $\Delta H^\circ_{n-1,n}$ and $\Delta S^\circ_{n-1,n}$.

4.2 Effect of the Heated Filament and Initial Translational Energy of K^+

To prove that the relative ionic concentrations were not affected by the presence of the hot filament whose temperature ranged from about 200° to 600° above the ion source temperature, three different filament arrangements were used. These are illustrated in Figures 2.4 and 2.5.

In Source I the filament was placed in a separate compartment attached to the ion source top. The location of Source I is such that the emitted ions and infrared radiation were incident on the ion exit slit. To show that the results did not depend on non-equilibrium heating of the ion source by the filament, experiments were done with two different diameter orifices between the filament compartment and the ion source. The larger orifice which was covered by an open grid had a diameter of 5 mm while the smaller orifice was 1.5 mm in diameter. As can be seen from Figure 4.9 the agreement using the two arrangements was satisfactory at higher temperatures. At the lower temperatures at which $K_{2,3}$ was measured, the two sets of points begin to disagree. Apparently the ionic concentrations and water vapor do not achieve thermal equilibrium with the temperature of the ion source wall in the 5 mm orifice arrangement. At 333°K, for example, the 5 mm orifice point would be on the $K_{2,3}$ line if the gas were 8° hotter than the ion source wall

where the temperature was measured. The agreement at higher temperatures is not surprising since under these conditions the filament temperature is closer to the temperature of the ion source walls.

Because the orifice diameter affected the results, a second source of K^+, Source II, was installed to further check the results. In this source, the emitted infrared radiation passed over the ion exit slit in a plane 5 mm above the slit. Ions entered the ion source in the same plane but could diffuse out of the plane after having entered the field free ion source. These ions then had at least 5 mm to equilibrate before passing through the ion exit slit. Figure 4.9 shows that the results obtained with this source are in agreement with the results obtained with the small orifice in Source I.

Another way in which the effect of heat transfer to the ion source can be examined is to vary the filament wattage. Usually the wattage was set at a constant value throughout an experiment. The minimum wattage was used to obtain a sufficient ion current for accurate measurement. On the occasions in which the filament wattage was changed during an experiment, no change in the equilibrium constant was noted. For example, at 58°C, 0.37 torr the wattage was reduced from 22W to 14W. $K_{3,4}$ was measured at both

wattages. The change in $K_{3,4}$ was about 3% which is approximately the experimental error in measuring the ion currents.

When the filament wattage was changed from about 25W to 15W in a study of the solvation of K^+ by NH_3, the equilibrium constants decreased by about 30%. For this reason Source III was installed. This source was similar to Source I but the filament was placed much farther away from the ion source (see Fig. 2.5). The use of Source III gave results in agreement with Sources I and II for the hydration of K^+ and eliminated the change of equilibrium constants with filament wattage in the $K^+(NH_3)_n$ system. The agreement of the results from Sources I, II, and III, therefore, is evidence that the heated filament does not introduce non-equilibrium thermal conditions in the ion source.

A second possibility of non-equilibrium arises from the excess translational energy with which the potassium ions enter the ion source. If this energy is incompletely removed, the measured equilibrium constants will be too low. One proof that this does not occur is the agreement of the results from Sources I and II. In Source I high translational energy ions have a greater chance of reaching the ion exit slit and should thus be sampled with greater efficiency than low translational energy ions. The opposite is true with Source II because with this arrangement the ions are initially directed over the slit rather than at it.

Figure 4.1 shows a plot of the ion ratio $K^+(H_2O)_4/K^+(H_2O)_3$ versus the electric field strength used in Source I to attract the potassium ions into the ion source. The invariance of the ion ratio plot and the theoretical calculations for the ion translational energy in Section 3.1B prove that the equilibrium constants were not affected by ions with excess translational energy.

4.3 Results and General Discussion

A. Results

Some representative data are shown in Table 4.1. The mass spectrum is tabulated for all pressures measured at three temperatures. Figures 4.2 - 4.8 show the plots of $K_{n-1,n}$ versus water pressure obtained at different temperatures.

Van't Hoff type plots of the equilibrium constants are shown in Figure 4.9. Table 4.2 lists values for $\Delta H°_{298}$, $\Delta G°_{298}$, and $\Delta S°_{298}$ for reaction 4.3. The values for $\Delta H°$ and $\Delta S°$ were determined from equation 4.2 by means of a least squares treatment

$$\log K_{n-1,n} = -\frac{\Delta H°_{n-1,n}}{2.3RT} + \frac{\Delta S°_{n-1,n}}{2.3R} \qquad 4.2$$

using values of $K_{n-1,n}$ measured at the various pressures and temperatures. In the case of reaction 5,6 where there is insufficient data to apply the least squares treatment, the thermodynamic values were calculated from the van't Hoff plot shown in Figure 4.9. $\Delta G°_{298}$ was calculated from equation 4.3.

Figure 4.1 Plot of $K^+(H_2O)_4/K^+(H_2O)_3$ with Electric Field Strength Used to Attract the Potassium Ions into the Ion Source.

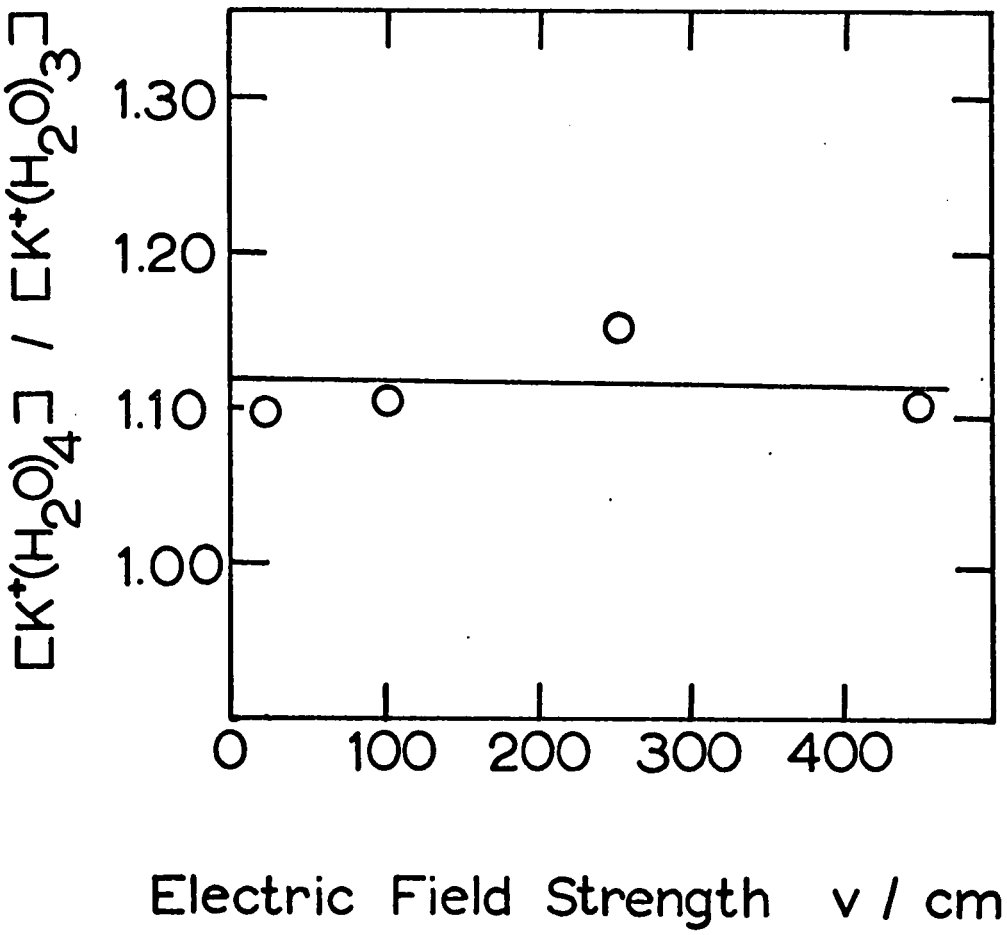

Source I with 1.5 mm orifice

Pressure 0.37 torr

Temperature 58°C

Usual Electric Field Employed: 100v/cm

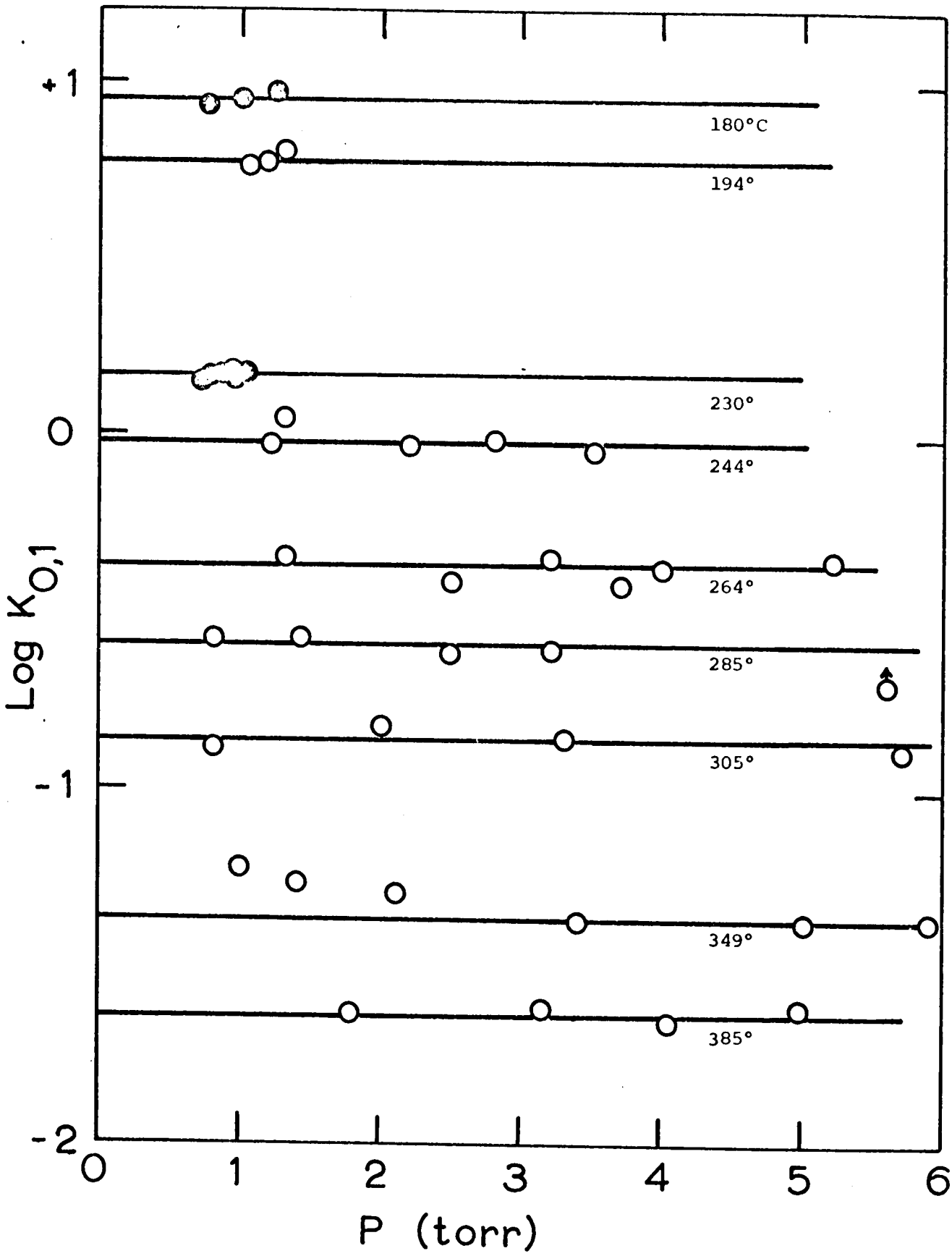

Figure 4.2 Log $K_{0,1}$ at various pressures and temperatures.

O, Source I with 5 mm orifice; ●, Source II

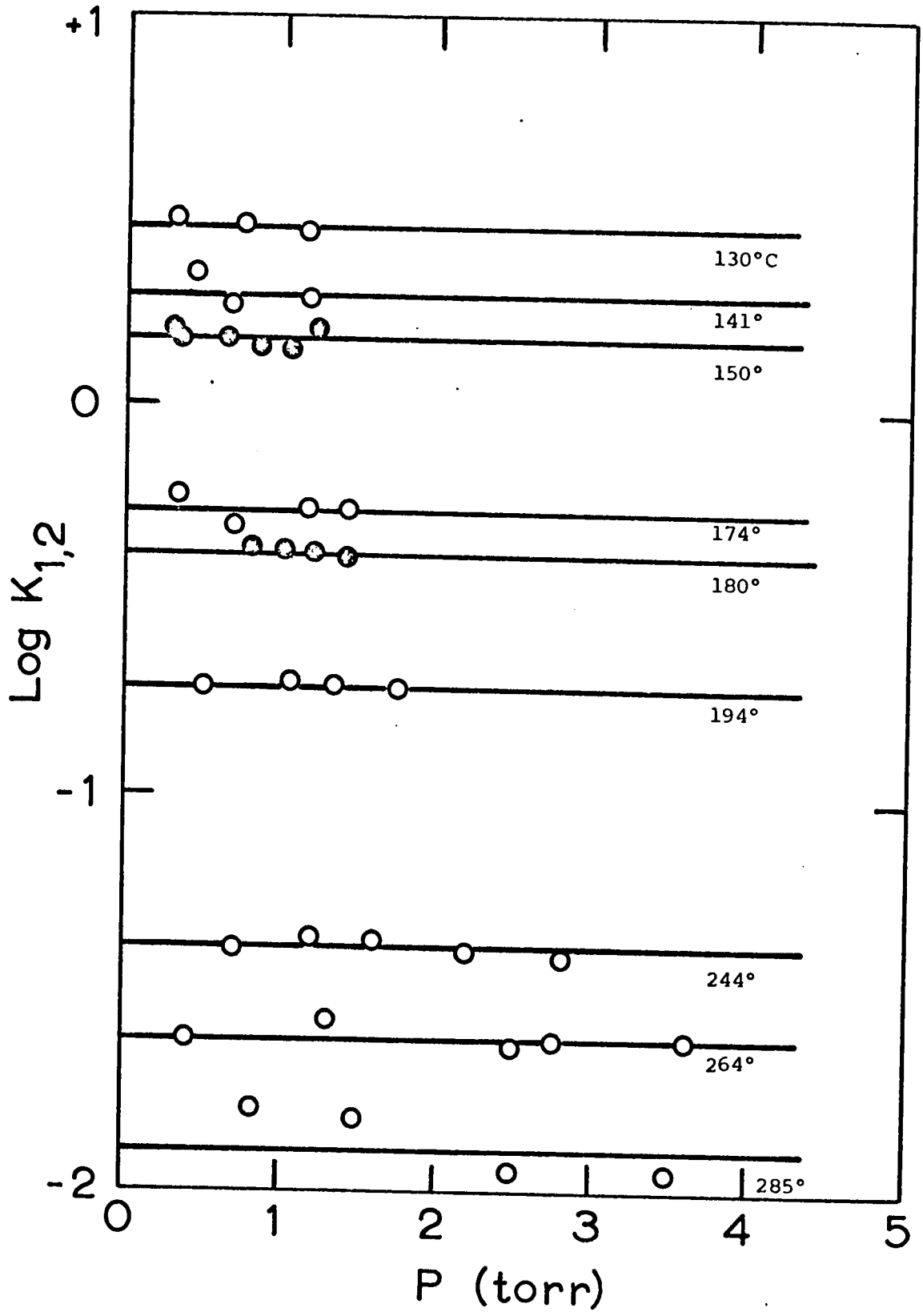

Figure 4.3 Log $K_{1,2}$ at various temperatures and pressures.

O, Source I with 5 mm orifice; ●, Source II

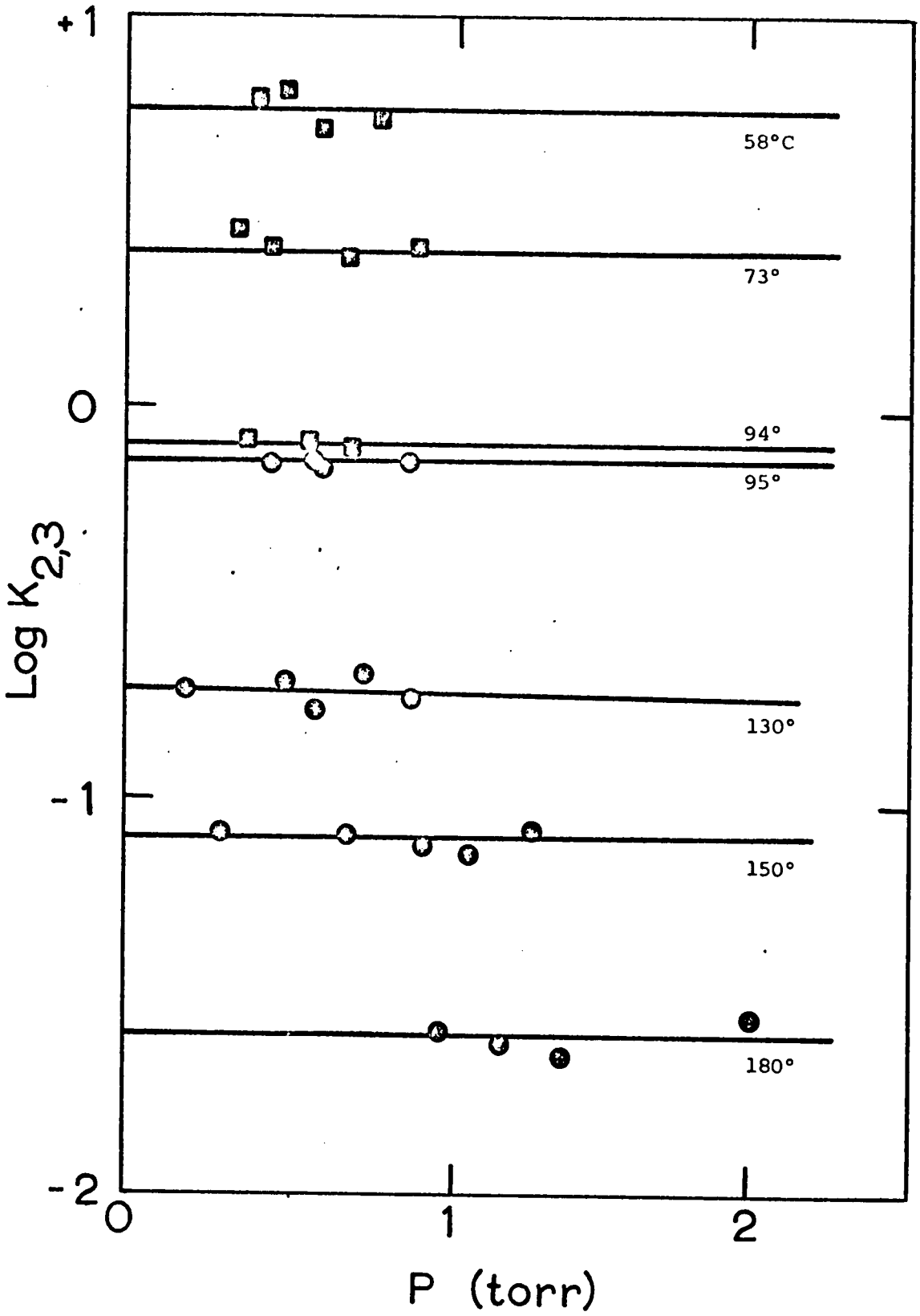

Figure 4.4 Log $K_{2,3}$ at various temperatures and pressures.

▣, Source I with 1.5 mm orifice; ●, Source II

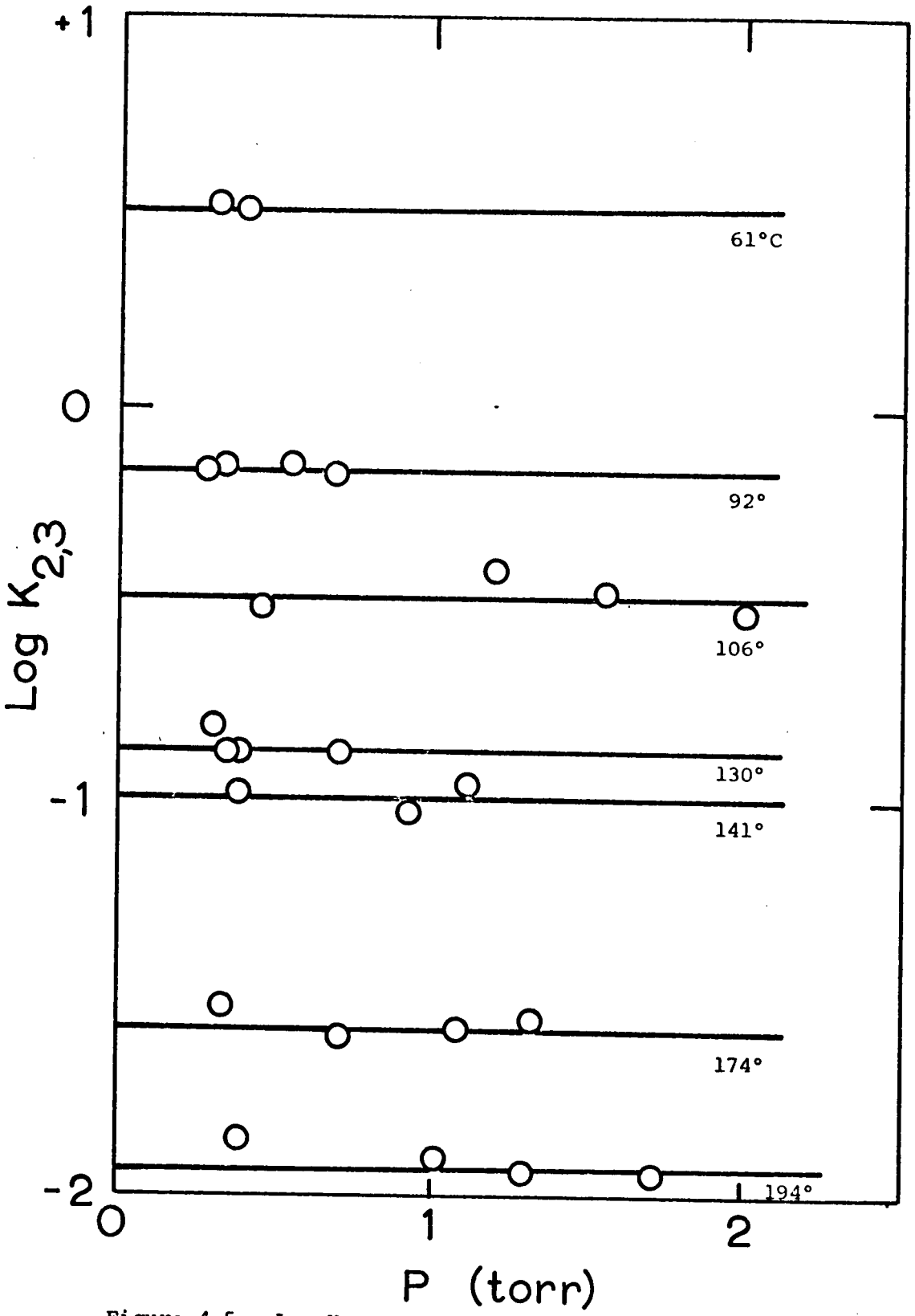

Figure 4.5 Log $K_{2,3}$ at various temperatures and pressures. The data (from Source I with a 5mm orifice) give lower free energy values than the data in Figure 4.4 due to non-equilibrium conditions.

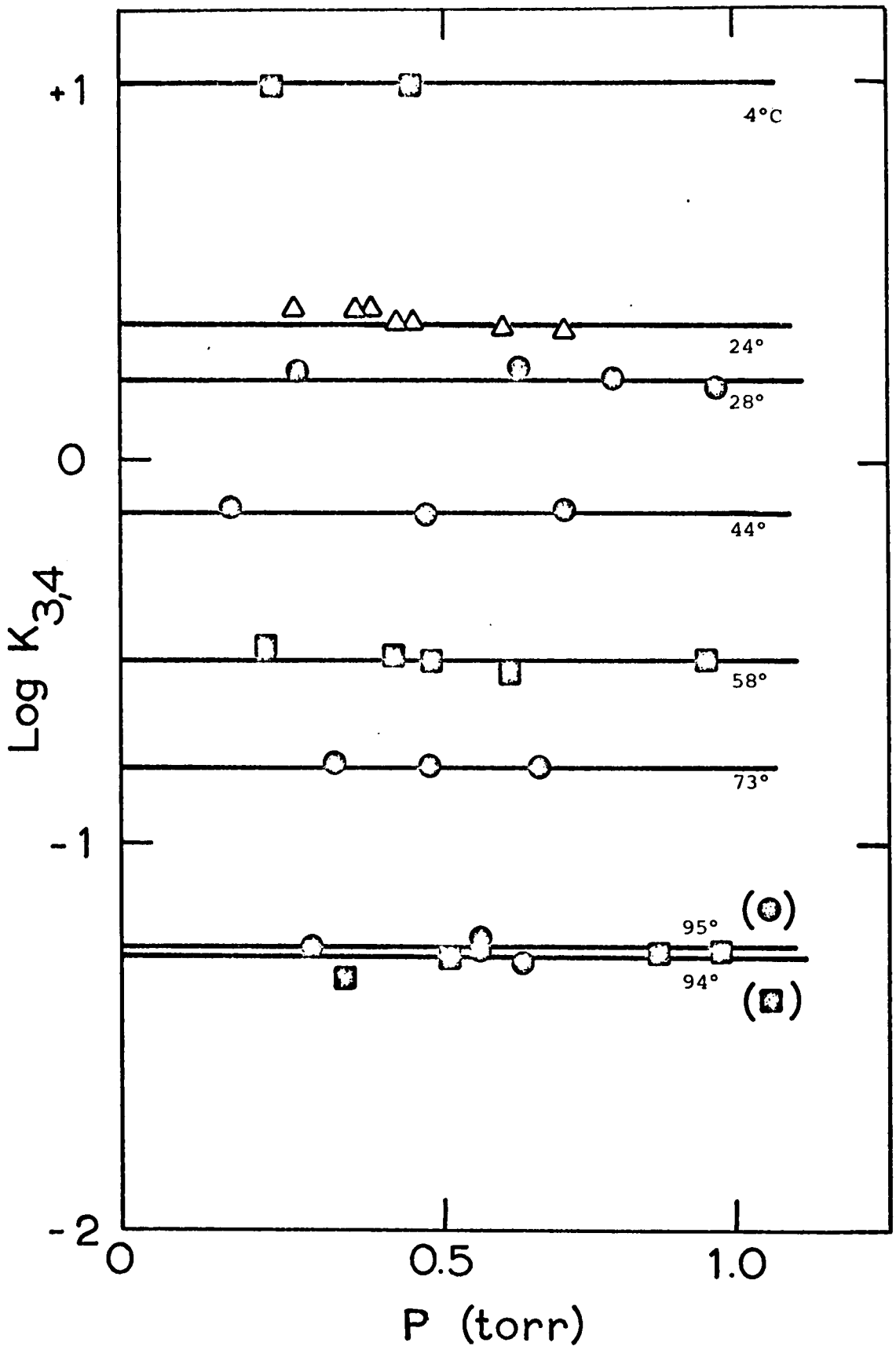

Figure 4.6 Log $K_{3,4}$ at various temperatures and pressures. ■, Source I with 1.5 mm orifice; ●, Source II; △, Source III

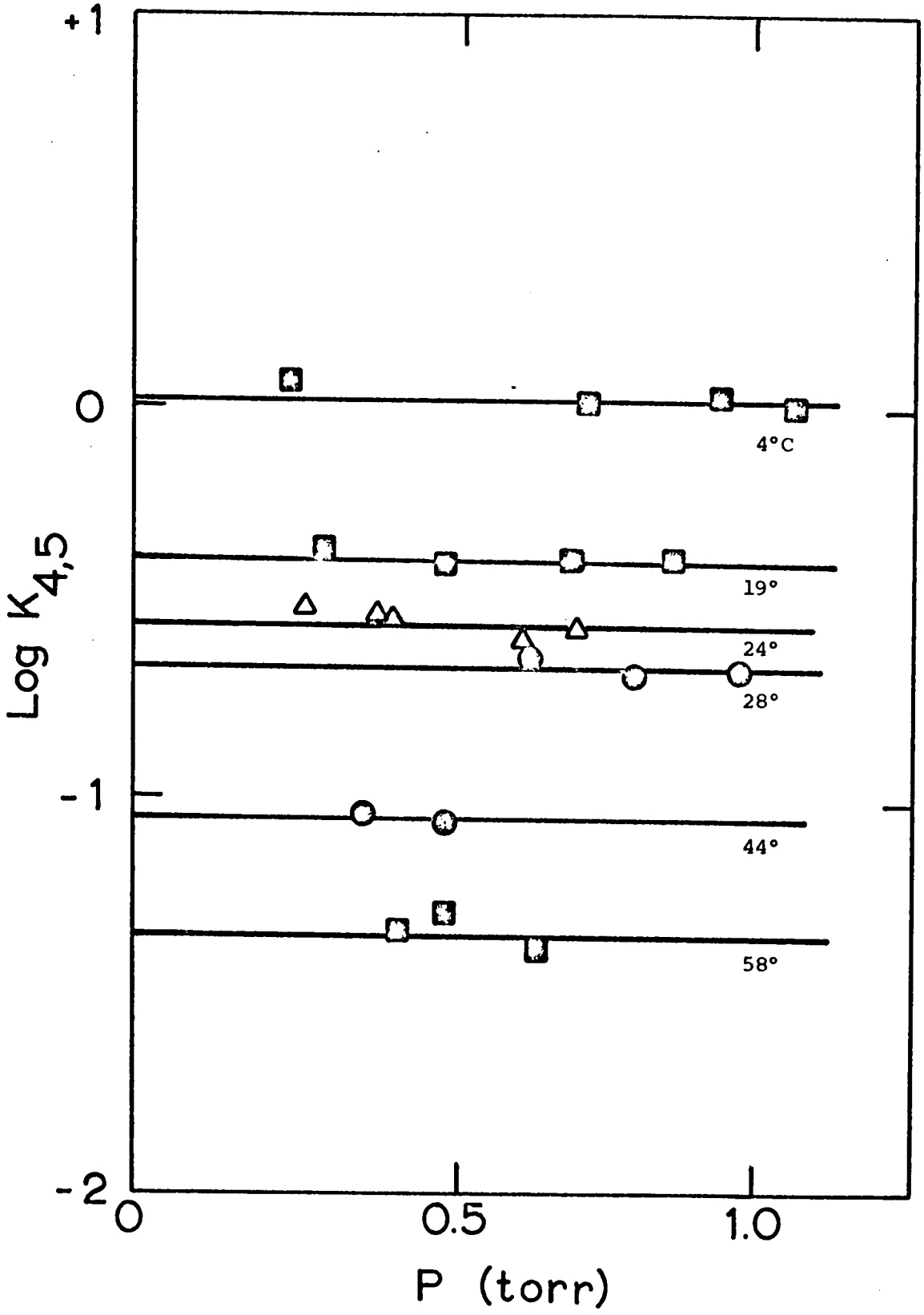

Figure 4.7 Log $K_{4,5}$ at various temperatures and pressures. ⊡, Source I with 1.5 mm orifice; ○, Source II; △, Source III

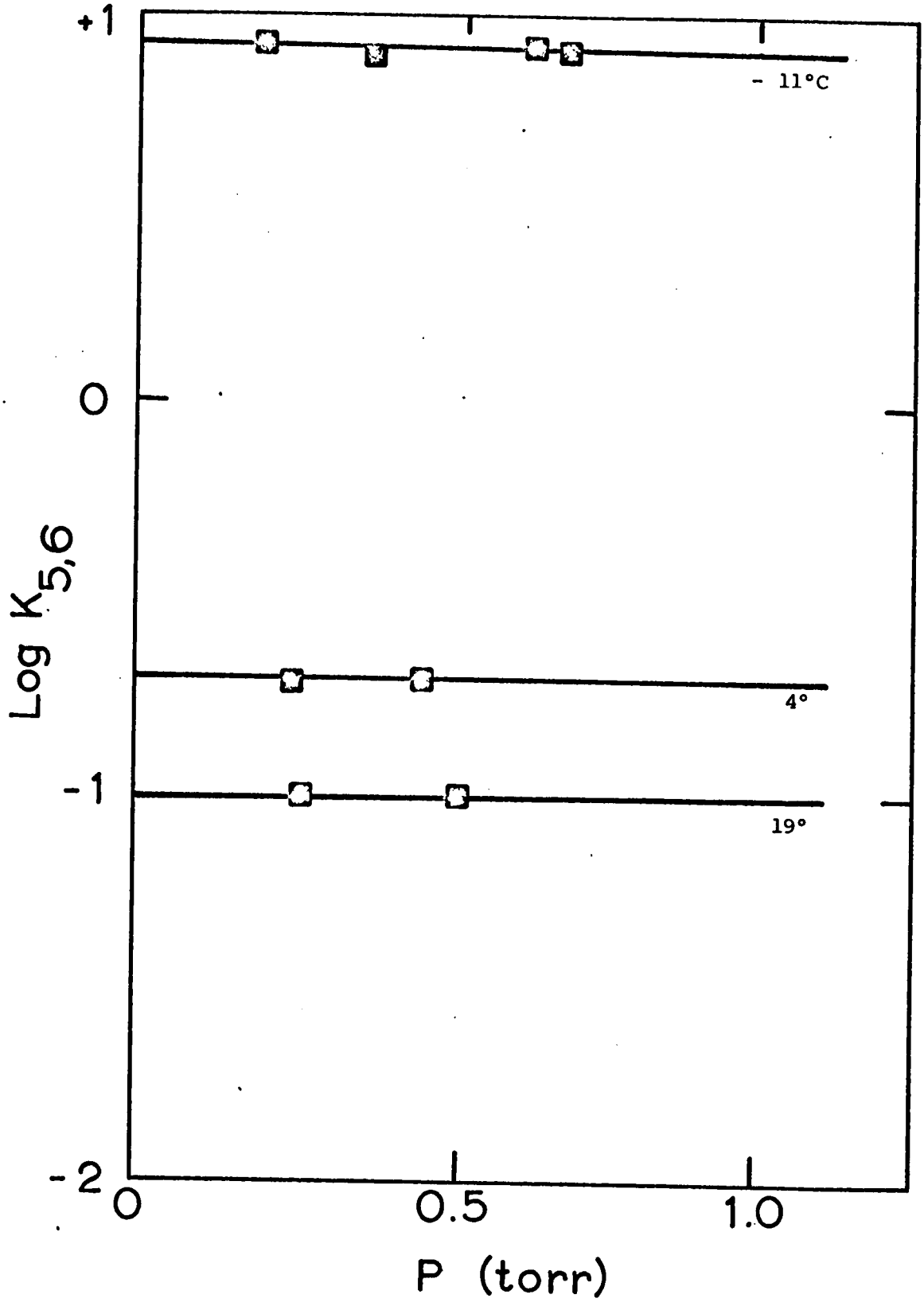

Figure 4.8 Log $K_{5,6}$ as a function of pressure at various temperatures. ◘, Source I with 1.5 mm orifice.

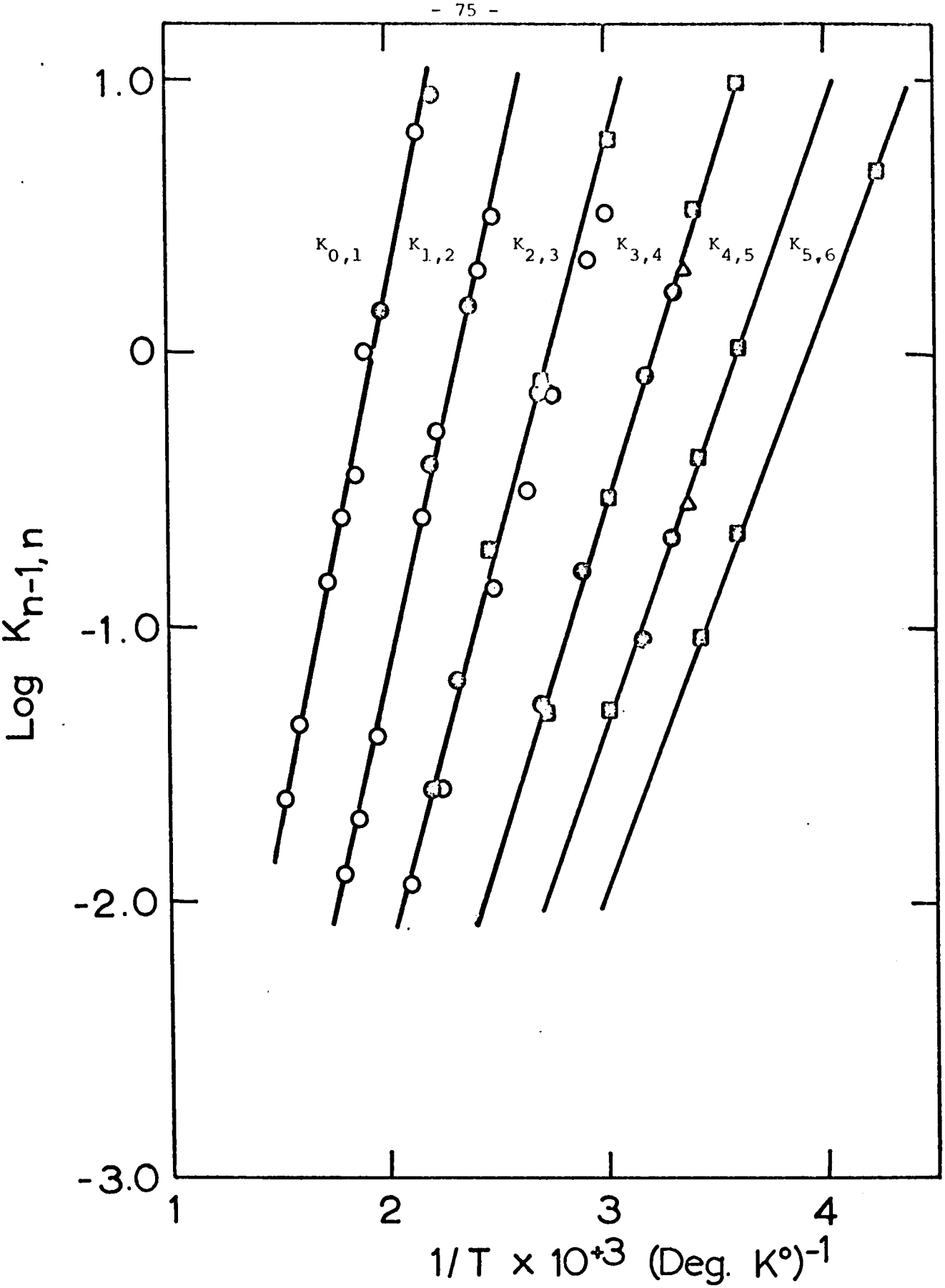

Figure 4.9 van't Hoff plots of equilibrium constants for the hydration of K^+: O, Source I with 5.0 mm entrance to the ion source; ⊡, Source I with 1.5 mm orifice entrance to the ion source; ●, Source II; and △, Source III.

TABLE 4.1

Representative Data for the Hydration of K^+

K^+ Source	Temp. C°	P. torr	Mass Spectrum of $K^+(H_2O)_n$ in % Total Ionization n=0	1	2	3	4	5	6	Total Ion Current x 10^{16} A
I[a]	19	0.31				42.5	50.6	6.87	0.23	0.5
		0.51				31.9	54.4	13.2	0.49	0.2
		0.70				24.7	58.3	17.1		0.07
		0.84				22.8	56.4	20.4		0.04
II	150	0.30			66.4	32.7	0.82			0.1
		0.35			65.2	34.5	1.28			0.1
		0.66			48.7	48.7	2.66			0.07
		0.88			43.4	52.8	3.59			0.05
		1.11			36.7	58.4	4.87			0.04
		1.35			35.4	58.9	5.59			0.03
I[b]	264	0.42	89.6	10.2	0.10					30
		1.28	62.3	36.5	1.20					3
		2.56	48.6	48.6	2.81					0.8
		3.22	39.1	56.5	4.33					0.5
		3.64	40.2	55.0	4.76					0.3
		3.94	35.2	59.9	4.94					0.3
		5.15	30.3	69.7						0.1

[a] Source used with 1.5 mm orifice entrance to the ion source.

[b] Source used with 5 mm open grid entrance to the ion source.

TABLE 4.2

Experimental Thermodynamic Values for the Gas Phase Reactions:

$$K^+(H_2O)_{n-1} + H_2O \rightleftarrows K^+(H_2O)_n \quad (n-1,n)$$

Reaction n-1,n	$-\Delta H°_{n-1,n}$ (kcal/mole)	$-\Delta G°^{a}_{n-1,n(298°)}$ (kcal/mole)	$-\Delta S°^{a}_{n-1,n}$ e.u.	A^b	B^b
0,1	17.9	11.4	21.6	3.89	7.57
1,2	16.1	8.9	24.2	3.50	8.14
2,3	13.2	6.3	23.0	2.87	7.88
3,4	11.8	4.4	24.7	2.57	8.26
4,5	10.7	3.2	25.2	2.33	8.35
5,6	10.0	2.3	25.7	2.18	8.46

[a] At standard state of water, 1 atm.

[b] Constants for the equation $\log (K_{n-1,n}) = (A/T) \times 10^3 - B$.

Data for water pressure in torr.

4.3 $$\Delta G^\circ = \Delta H^\circ - T\Delta S^\circ$$

B. Entropy of the $K^+(H_2O)$ Complex

The experimental entropy value $\Delta S^\circ_{0,1}$ can be compared to a theoretical value obtained from calculation of the translational, rotational and vibrational entropy changes. The values for the other $\Delta S^\circ_{n-1,n}$ could also be calculated but a large number of approximations would have to be made.

The translational entropy of a species in the gas phase is given by the Sackur-Tetrode equation, (47) 4.4,

4.4 $$S^\circ_{tr} = \frac{3}{2} R \ln M + \frac{5}{2} R \ln T - 2.311$$

where M is the ordinary molecular weight (g/mole). The gas constant R must be substituted in cal/mole-degree to obtain the entropy in cal/mole-deg. The change in translational entropy for the condensation reactions considered here is given by 4.5.

4.5 $$\Delta S^\circ_{tr} = \frac{3}{2} R \ln \frac{M_{K^+(H_2O)}}{M_{K^+} \times M_{H_2O}} - \frac{5}{2} R \ln T + 2.311$$

On substitution for reaction 0,1 at 298°K, $\Delta S^\circ_{tr} = -33.6$ e.u.

The rotational entropy change can be calculated from the rotational entropy of H_2O and $K^+(H_2O)$. The appropriate equation (47) is 4.6,

4.6 $$S^\circ_{rot} = RT \frac{d(\ln Q_{rot})}{dT} + R \ln Q_{rot}$$

where Q_{rot}, the rotational partition function (48), is given by

$$4.7 \qquad Q_{rot} = \frac{8\pi^{5/2} kT (8\pi^2 kT I_x I_y I_z)^{1/2}}{\sigma h^3}$$

4.7 where I_x, I_y, and I_z are the three moments of inertia about the three principal axes and σ is the symmetry number. Differentiation of Q_{rot} with respect to T and substitution into 4.6 gives 4.8.

$$4.8 \qquad S°_{rot} = \frac{3}{2} R + R \ln Q_{rot}$$

For the rotational entropy of water, substitution of $\sigma = 2$, and I_x, I_y, and I_z = 1.91, 1.02, and 2.94 x 10^{-40} g cm^2 respectively leads to $S°_{rot}$ = 10.1 e.u. at 298°K.

In order to calculate $S°_{rot}$ for $K^+(H_2O)$ the $K^+ - OH_2$ bond length must be known. As shown in Section 4.4 a reasonable distance between the centers of the potassium ion and oxygen atom is 2.6Å. The moments of inertia are then I_X = 1.91, I_Y = 147 and I_Z = 149 x 10^{-40} g cm^2. The three principal axes for the H_2O and K^+H_2O are shown in Figure 4.10. Substitution of the moment of inertia into 4.8 leads to $S°_{rot}$ = 19.3 e.u. with $\sigma = 2$.

The vibrational entropy change for reaction 0,1 can only be approximately calculated because the fundamental vibration frequencies of $K^+(H_2O)$ have to be estimated to

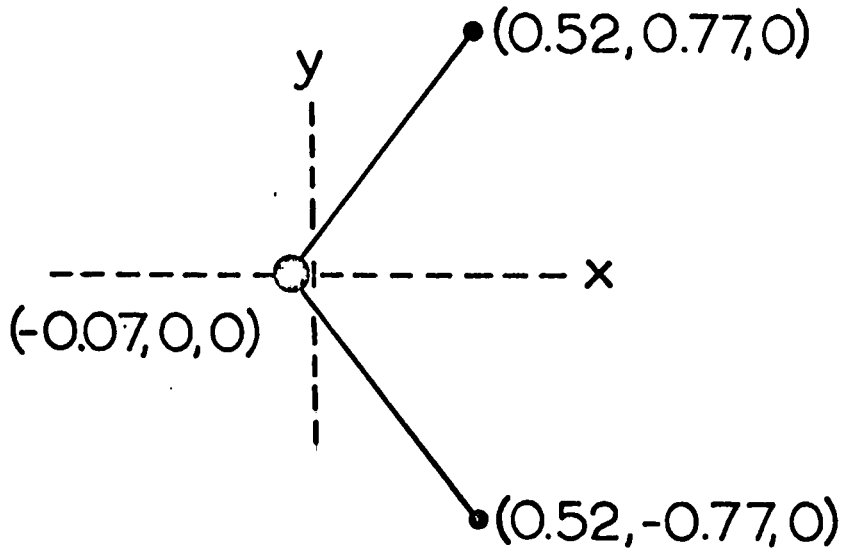

Principal Axes of H_2O

The z axis is mutually perpendicular to the x and y axes and passes through the point (0.04, 0,0).

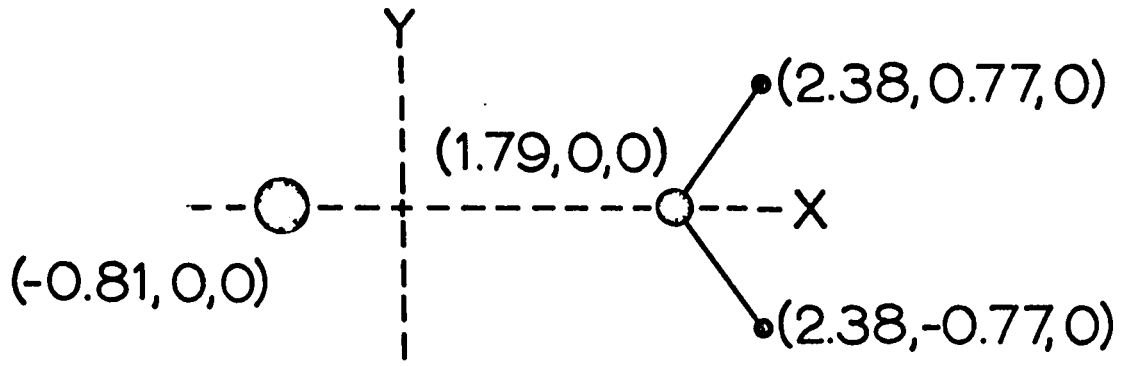

Principal Axes of $K^+(H_2O)$

The Z axis is mutually perpendicular to the X and Y axes and passes through the point (0.02, 0,0)

Figure 4.10 Principal Axes of H_2O and $K^+(H_2O)$ used to calculate the moments of inertia.

calculate $S°_{vib}$. To simplify the calculations the assumption is made that the vibrational entropy of H_2O is unchanged by bonding to K^+. The coordinated H_2O is treated as a rigid molecule which has a vibration along the potassium-oxygen axis. A value for the force constant of the vibration can be estimated from the electrostatic calculations given in the next section.

Thus from the calculated potential energy plot shown in Figure 4.19 the force constant k for the vibration can be calculated to be 5.8×10^4 dyne/cm by fitting equation 4.9 (49) to the bottom portion of the P.E. Curve. From equation 4.10 (49) where ν is the fundamental vibration frequency and μ is the

$$4.9 \qquad \Delta \text{ P.E.} = \frac{1}{2} k (R - R_{eq.})^2$$

$$4.10 \qquad \nu = \frac{1}{2\pi} \left(\frac{k}{\mu}\right)^{\frac{1}{2}}$$

reduced mass, ν is calculated to be 8.47×10^{12} sec^{-1} after substitution for k and μ which was approximated as $(18)(39)/(18 + 39)(6.02 \times 10^{23})$ g/molecule. From $\varepsilon_o = \frac{1}{2}h\nu$ and equation 4.11 (47), $S°_{vibA} = 2.8$ e.u. at 298°K.

$$4.11 \qquad S°_{vib} = \left(\frac{R}{\exp(\varepsilon_{o/kT}) - 1}\right)\left(\frac{\varepsilon_o}{kT}\right) - R \ln (1-\exp(-\varepsilon_{o/RT}))$$

In addition to the vibration along the potassium-oxygen axis, there are two torsional vibrations of the water molecule in the complex about its y and z axes. The fundamental vibration

frequency can be calculated from equation 4.12 (48) where n is the symmetry number, Δ P.E. is the potential energy barrier for rotation, and I is the moment of inertia. The values of

$$\nu = \frac{n}{2\pi}\left(\frac{\Delta \text{ P.E.}}{2I}\right)^{\frac{1}{2}} \qquad 4.12$$

Δ P.E. can be calculated from the coordinates of the molecule in its minimum energy position (Figure 4.10) and in its maximum energy position (rotation by 180° about the y and z axes from the minimum position) by use of equations 4.17, 4.18 and 4.20. The resulting values are 29 and 34 kcal/mole for $\Delta \text{ P.E.}_y$ and $\Delta \text{ P.E.}_z$ respectively. This leads to $\nu_y = 1.59 \times 10^{13}$ sec^{-1} and $\nu_z = 1.03 \times 10^{13}$ sec^{-1}, $E_y = \frac{1}{2}h\nu_y = 0.76$ kcal/mole and $E_z = \frac{1}{2}h\nu_z = 0.485$ kcal/mole, and therefore, by equation 4.11: $S°_y = 1.6$ e.u. and $S°_z = 2.4$ e.u.

The total entropy change can now be calculated by summing the individual contributions. The total calculated value is -17.6 e.u. compared to the experimental value of -21.6 e.u. The difference between the two values suggests that the experimental value may be somewhat smaller than the true value for $\Delta S°_{0,1}$.

C. Distribution of $K^+(H_2O)_n$ Clusters as a Function of Water Pressure

The relative concentrations of species $K^+(H_2O)_n$ can

be calculated at a given water pressure P by using equation 4.13.

$$4.13 \qquad \log [K^+(H_2O)_n] = n \log P + \sum_{i=1}^{n} \log K_{i-1,i}$$

The equilibrium constants $K_{i-1,i}$ at a given temperature are conveniently obtained from the van't Hoff straight lines, equation 4.14.

$$4.14 \qquad \log K_{i-1,i} = \frac{Ax1000}{T} - B$$

Values for A and B are given in Table 4.2. The use of equation 4.13 necessitates knowledge of one of the cluster concentrations. By setting the concentration of K^+ equal to unity the other concentrations can be calculated. Setting the sum of all concentrations equal to 100, one obtains the relative concentrations in per cent of the total. Figure 4.11 illustrates the relative concentrations as a function of pressure at T = 300°K. The plots show a characteristic behavior which is also observed in plots arising from the $H^+(H_2O)_n$ data. At low pressures where the low hydrates are present, the difference between the stability (free energy) of the hydrates is large and the concentrations of one or two hydrated species are dominant. At higher pressures where the higher hydrates become stable, differences between the free energies of the hydrates are small and a number of hydrated species are present simultaneously.

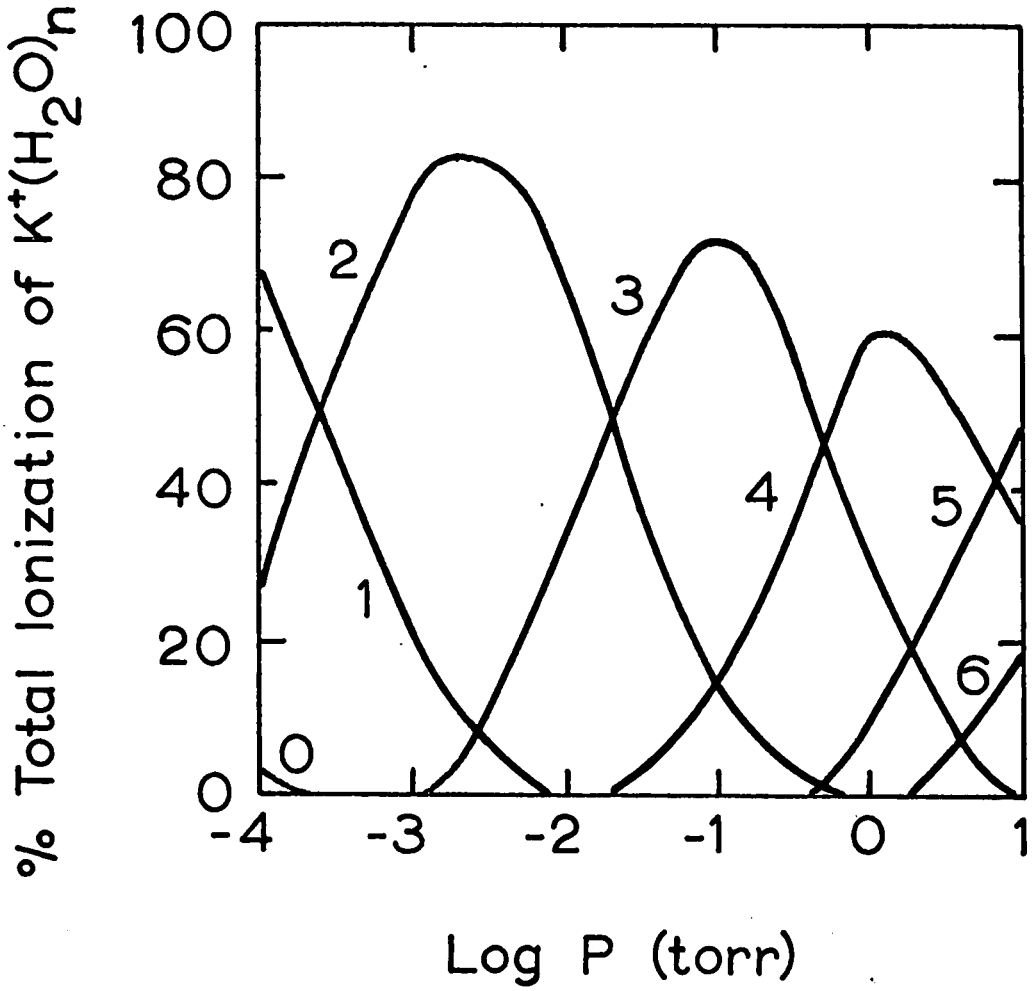

Figure 4.11 Plot of Relative Concentrations of $K^+(H_2O)_n$ with Log P at 300°K.

The effect is more pronounced in the $H^+(H_2O)_n$ results.

D. Comparison with Earlier Work

The equilibrium constant $K_{0,1}$ has been obtained in earlier work by Chupka (50). The possibility of determining this equilibrium constant occurred to Chupka while he was measuring the dissociation energies of gaseous alkali halide complex ions. To produce the ions K^+ and $K^+(H_2O)$ he passed water vapor at a pressure of 2×10^{-3} torr through an oven which was coated with KCl and heated to 570°C. The resulting ions from the thermal ionization and equilibration were mass analyzed. The value obtained in this manner was $K_{0,1} = 1.25$ at 570°C.

Unfortunately the present determinations of $K_{0,1}$ extend only to 385°C so that a direct comparison of the $K_{0,1}$ values can not be made. However a fairly accurate extrapolation can be obtained by use of equation 4.14. The extrapolated value for $K_{0,1}$ obtained in this manner is 0.93 (both $K_{0,1}$ values relate to a standard state of one atm). The agreement between Chupka's and the present $K_{0,1}$ is fortuitously close considering the widely different experimental conditions. Also the Chupka constant was obtained at a single pressure which was not directly measured, but estimated.

E. Proton Affinity of KOH

One interesting result from the present work is that $\Delta H°_{0,1}$ can be used to calculate a value for the proton affinity of KOH. The heat of formation of $K^+(H_2O)$ in the gas phase is given by equation 4.15.

$$4.15 \quad \Delta H_f(K^+H_2O) = \Delta H_f(K^+) + \Delta H_f\ (H_2O) + \Delta H_{0,1}$$

The values for the gas phase heats of formation of the potassium ion and water are $\Delta H_f(K^+) = 122$ and $\Delta H_f(H_2O) = -57$ kcal/mole (51) respectively. Substituting into 4.15 one obtains $\Delta H_f K^+(H_2O) = +47$ kcal/mole. From the value of ΔH_f of KOH(g), -58, and ΔH_f of H^+, 367 kcal/mole, (51), the proton affinity of KOH, represented by reaction 4.4 and equation 4.16 can be calculated to be 262 kcal/mole.

$$4.4 \qquad H^+_{(g)} + KOH_{(g)} \longrightarrow K^+(H_2O)_{(g)}$$

$$4.16 \quad \Delta H_{P.A.} = \Delta H_f\ K^+(H_2O) - \Delta H_f\ H^+ - \Delta H_f\ KOH$$

From a literature search it appears that the proton affinity of KOH has not been previously determined. In comparison the proton affinities of H_2O, CH_3OH, and C_2H_5OH are 169, 180, and 193 kcal/mole respectively (51). In this series the increase in proton affinity is due to the increasing polarizability of the substituent group ($H < CH_3 < C_2H_5$). This makes the oxygen more negative in the protonated species and increases the bond

energy between the proton and the oxygen. The oxygen in KOH is expected to have a high negative charge because the compound is ionic. Consequently the proton affinity should be high.

4.4 Comparison of Measured Enthalpies and Calculated Electrostatic Potential Energy Changes for Hydration of K^+

A. Introduction

Classical electrostatic energy calculations were made for the potential energy changes which occur when water ligands bond to K^+. Δ P.E.$_{n-1,n}$ values were then compared to experimental values of $\Delta H°_{n-1,n}$ at 298°K.

Actually the electrostatic energy corresponds best to ΔH at 0°K because of neglect of all thermal motion in the calculations. The comparison at 298°K assumed $\Delta Cp = 0$. In spite of this assumption, which involves a considerable approximation, it is felt that meaningful conclusions can be made from a comparison of the electrostatic calculations with the experimental enthalpy values.

B. The Electrostatic Calculations

The electrostatic potential energy of an ion surrounded by molecules can be expressed by the following terms: ion-dipole and ion-polarizability attraction and dipole-dipole and ion-atom repulsion. A point charge model which was used in these calculations is shown in Figure 4.12.

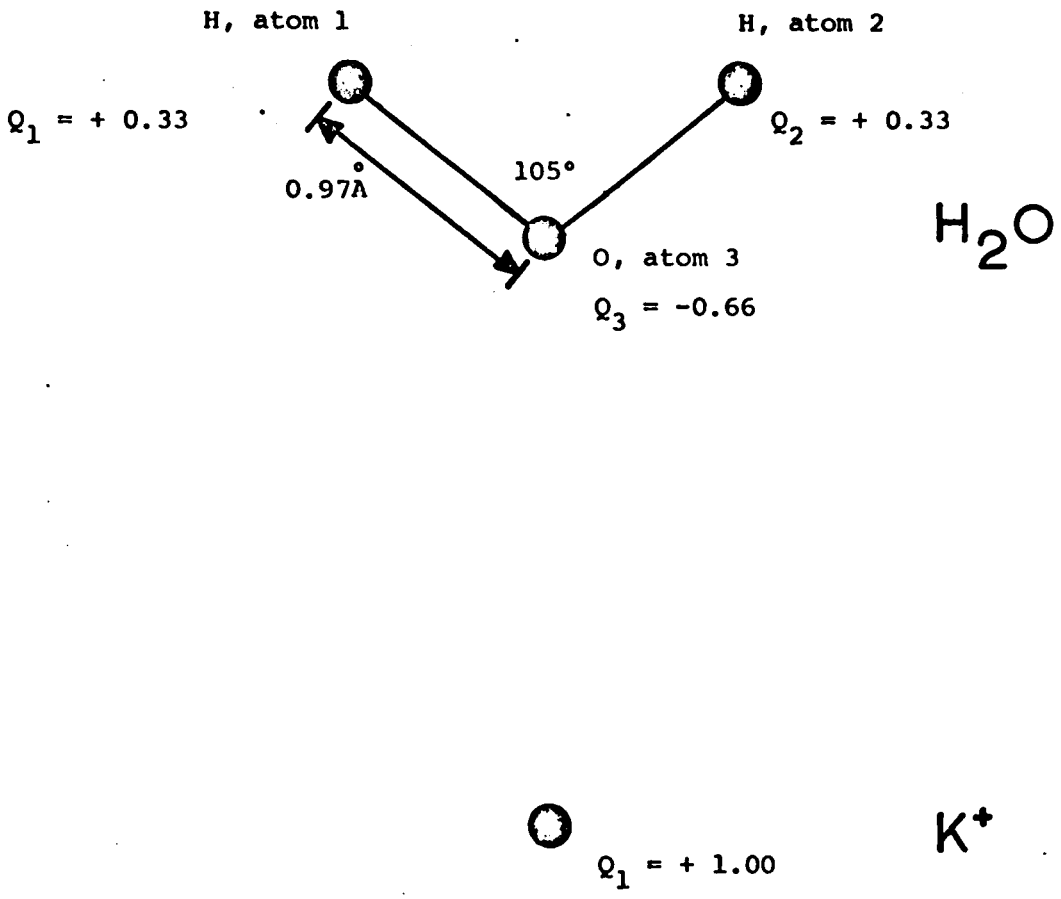

Figure 4.12 $K^+(H_2O)$ model used in the theoretical calculations.

The charge assignment resulted from the separation of the dipole moment of water onto the three point atoms. The model and equations are similar to those used by Doyne and Caldwell (52) who considered the $H_3O^+(H_2O)_n$ system.

Equations 4.17 - 4.21, which are written in a general form, were used to compute the P.E. of $K^+(H_2O)_n$ over a range of K^+—— OH_2 distances by means of an IBM 360 Computer. The program used is given in the Appendix.

4.17 Ion-Dipole

$$EE = \sum_{j=1}^{n} \sum_{i=1}^{p} \frac{(334)(Q_{ion})(Q_{i,j})}{R_{i,j}}$$

4.18 Ion-Polarizability

$$EPOL = - \sum_{j=1}^{n} \sum_{i=1}^{p} \frac{(167)(Q_{ion})^2 \alpha_{i,j}}{R^4_{i,j}}$$

4.19 Dipole-Dipole

$$EDIP = \sum_{\ell=2}^{n} \sum_{i=1}^{p} \sum_{j=1}^{\ell-1} \sum_{k=1}^{p} \frac{(334)(Q_{i,j})(Q_{k,\ell})}{R_{i,j,k,\ell}}$$

4.20 Ion-Atom

$$EREP = \sum_{j=1}^{n} \sum_{i=1}^{p} \frac{A_{i,j}}{R^{12}_{i,j}}$$

4.21 $$E_n = EE + EPOL + EDIP + EREP$$

Q_{ion} is the ionic charge and $Q_{i,j}$ is the charge on the $i^{\underline{th}}$ atom of the $j^{\underline{th}}$ molecule with p atoms per molecule and n molecules per cluster. $R_{i,j}$ is the ion-atom distance while $R_{i,j,k,\ell}$ is the distance between the $i^{\underline{th}}$ atom of $j^{\underline{th}}$ molecule and the $k^{\underline{th}}$ atom of molecule ℓ. α is the atomic polarizability and A is a semi-empirical constant for the ion-atom repulsion whose evaluation will be described later. The numerical factors in equations 4.17 - 4.21 are adjusted to give the energy in kcal/mole for Q in atomic units, R in $\mathring{A}$ and α in $\mathring{A}^3$. In the case of 4.20 the numerical factor is part of A which has the units $\mathring{A}^{12}$ $(\text{kcal/mole})^{-1}$. The α values used were 0.60 for oxygen and $0.44\mathring{A}^3$ for hydrogen (53).

The computed values for the ion-dipole and ion-polarizability potential energies of $K^+(H_2O)$ over a range of $R_{3,1}$ (the distance which corresponds to the distance between the centers of the potassium ion and oxygen atom) from 2.2 to 4.1 $\mathring{A}$ are tabulated in Table 4.3. The numerical values show that in this distance interval the ion-dipole energy is much larger than the ion-polarizability energy. Furthermore the predominance of the ion-dipole energy over the ion-polarizability energy increases rapidly over this range.

For the higher hydrates many structures are possible. The assumed structures are shown in Figure 4.13. In these structures all the K^+—— OH_2 distances are equal. (This

TABLE 4.3

Potential Energies (kcal/mole) for $K^+ - H_2O$ as a Function of $R_{3,1}$

$R_{3,1}$ A°	EE (ion-dipole)	EPOL (ion-polarizability)	EE & EPOL
2.20	-24.04	-6.37	-30.41
2.30	-22.14	-5.42	-27.56
2.40	-20.45	-4.64	-25.09
2.50	-18.95	-3.99	-22.95
2.60	-17.61	-3.46	-21.07
2.70	-16.40	-3.01	-19.42
2.80	-15.32	-2.64	-17.95
2.90	-14.33	-2.32	-16.65
3.00	-13.44	-2.05	-15.49
3.10	-12.63	-1.81	-14.44
3.20	-11.89	-1.61	-13.50
3.30	-11.21	-1.44	-12.65
3.40	-10.59	-1.29	-11.88
3.50	-10.02	-1.16	-11.17
3.60	- 9.49	-1.04	-10.53
3.70	- 9.00	-0.94	- 9.94
3.80	- 8.55	-0.85	- 9.40
3.90	- 8.13	-0.77	- 8.91
4.00	- 7.75	-0.70	- 8.45
4.10	- 7.38	-0.64	- 8.03

Figure 4.13 Assumed $K^+(H_2O)_n$ Structures

A Structures

n=2, linear

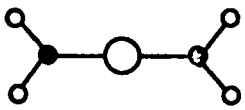

B Structures

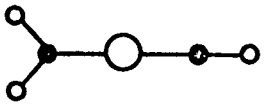

One molecule of the A structure has been rotated by 90° to obtain the B structure.

---

n=3, trigonal

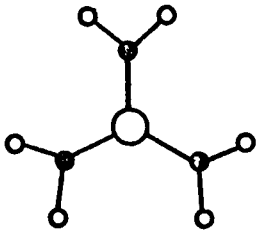

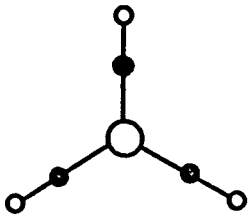

All 3 molecules of the A structure have been rotated by 90° to obtain the B structure.

---

n=4, tetrahedral

"top" view

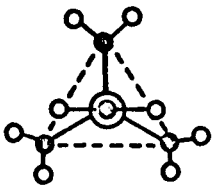

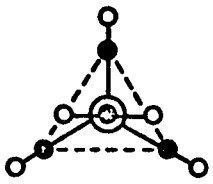

The three molecules which are trigonal to each other have been rotated by 90° from the A structure to obtain structure B.

Figure 4.13 Cont'd.

A Structures

B Structures

n=5, bipyramidal

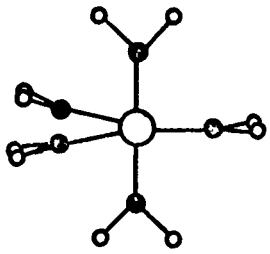

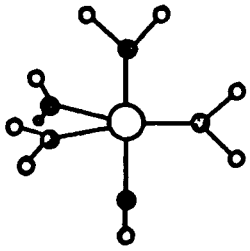

All molecules but the top one have been rotated by 90° to obtain the B structure from the A structure.

---

n=6, octagonal

"top" view

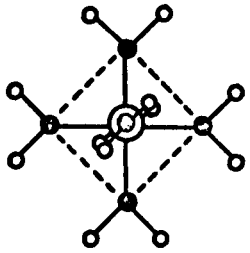

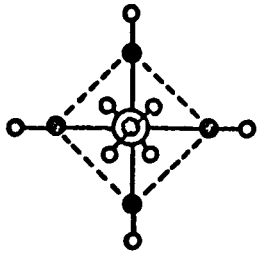

All molecules but the "top" one have been rotated by 90° to obtain the B structure from the A structure.

means that the total energy change calculated from equations 4.17, 4.18 and 4.20 for addition of the $n^{\underline{th}}$ water is the same for each addition of water at a constant ion-ligand separation distance). In general the most symmetrical ligand arrangements were used to minimize the dipole-dipole repulsions. Two different geometries were used for each structure to examine the effect of rotation of the ligands about their dipole axes. Structure B was obtained from A by rotation of some of the water molecules by 90°. The two structure groups did not change the computed dipole-dipole repulsion within the precision of the computation i.e. less than ± 0.05 kcal/mole. Figure 4.14 shows the total dipole-dipole repulsion for each cluster calculated from equation 4.19 as a function of $R_{3,1}$. The increase in dipole-dipole repulsion due to the addition of H_2O to $K^+(H_2O)_{n-1}$ for n=2-6 can be calculated for any assumed $R_{3,1}$ distances for $K^+(H_2O)_{n-1}$ and $K(H_2O)_n$ by using Figure 4.14. Figure 4.15 illustrates the increase in dipole-dipole repulsion calculated from the plots in Figure 4.14 at $R_{3,1} = 2.6\mathring{A}$ which represents an average radius expected for these clusters. It was intuitively expected that the potential energy difference should show a smooth, near exponential increase with increasing n-1,n. The actual plot shows an "S" shape. This can be explained by the following. The number of additional ligand repulsions per addition of the $n^{\underline{th}}$

Figure 4.14 Plot of the total dipole-dipole repulsion energy due to the reaction $K^+ + nH_2O \longrightarrow K^+(H_2O)_n$.

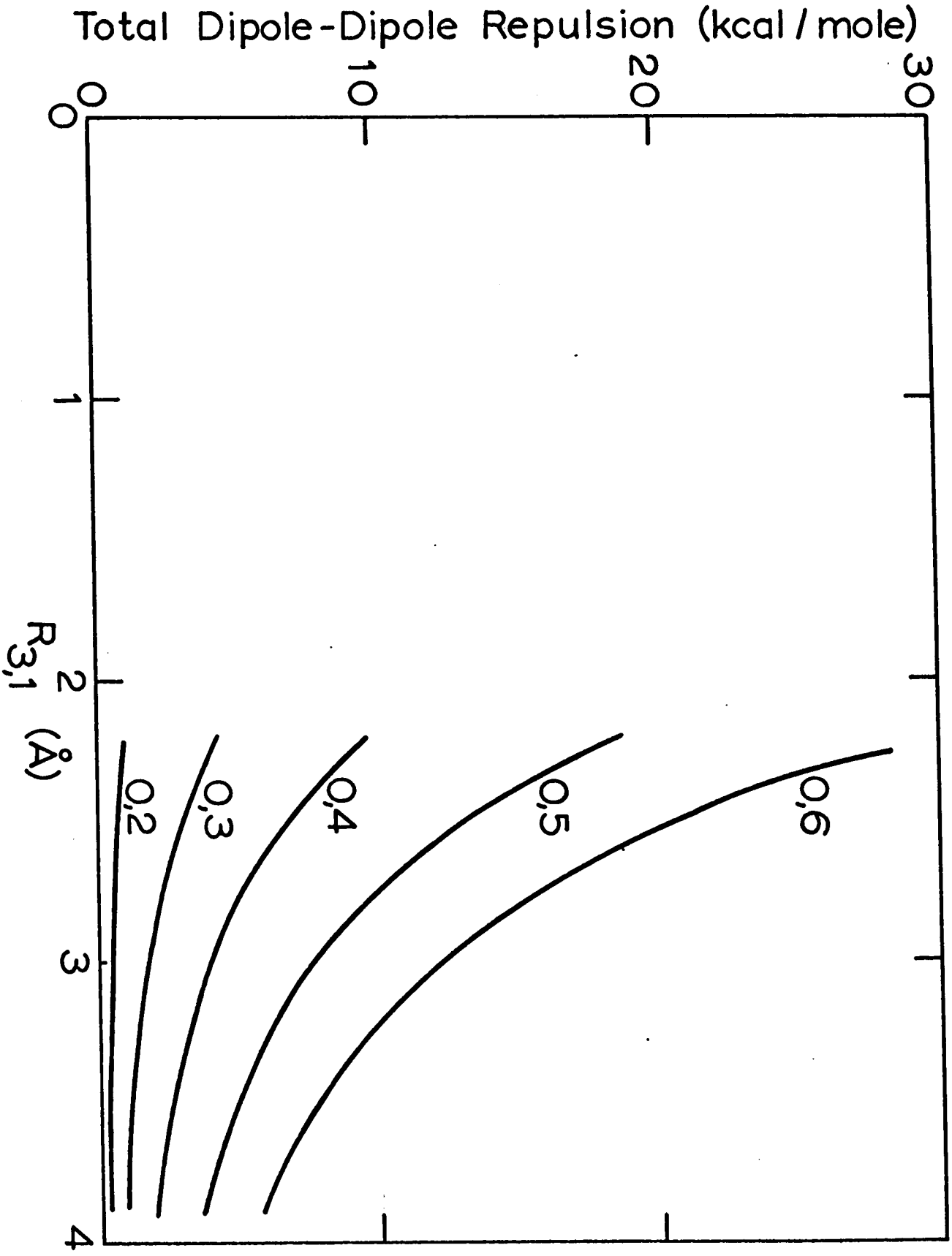

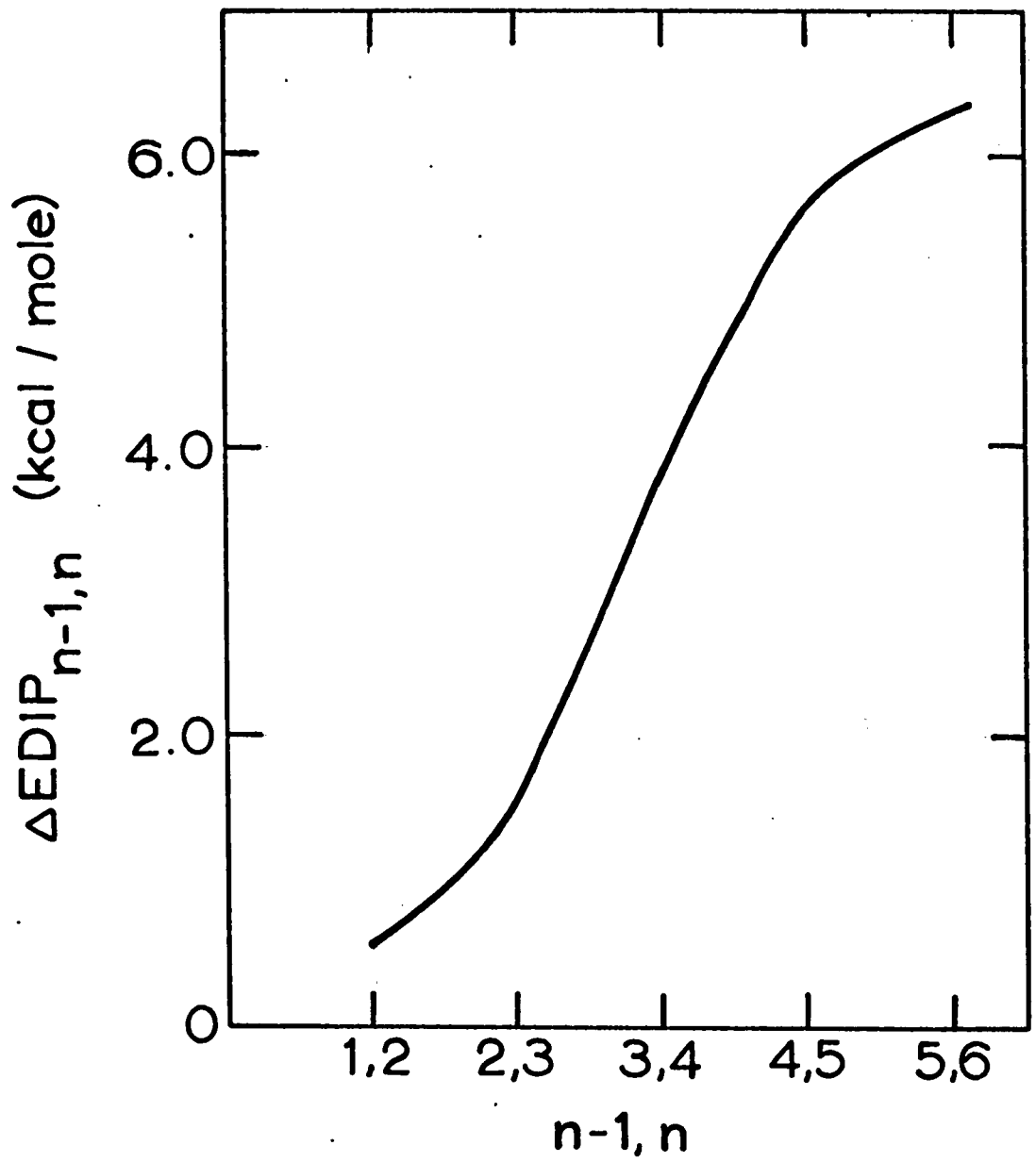

Figure 4.15 Plot of the change in dipole-dipole energy for the reaction $K^+(H_2O)_{n-1} + H_2O \longrightarrow K^+(H_2O)_n$ where

$R_{3,n} = 2.6\mathring{A}$

ligand is n-1. This fact suggests the smooth exponential increase in ΔEDIP with increasing n-1,n. Table 4.4 shows the distances between the centers of the oxygen atoms in the assumed structures at $R_{3,n} = 2.6\text{Å}$. The values in parentheses are the number of distinct interactions with this separation distance. From the table it can be seen that the oxygen atom separation decreases with increasing cluster size in an irregular manner. This is a consequence of the different point group structures for different n. The irregular decrease apparently leads to the shape of the plot in Figure 4.15.

A complete calculation of the P.E. should consider in addition to the electrostatic forces used above, the ion-ligand and ligand-ligand repulsion energies and the ion-ligand and ligand-ligand London dispersion energies. The latter are quite small (less than a few kcal/mole) (52,54) and can be neglected. The ligand-ligand repulsion energy can be expected to be less than the ion-ligand repulsion energy since the repulsion varies with R^{-12} (54,55) and the ligand-ligand distance is in general 50% greater than the ion-ligand distance. Since the ion-ligand repulsion energy is a minor contribution to the total P.E., the ligand-ligand repulsion energy can be neglected.

To calculate the ion-ligand repulsion energy from equation 4.20 it is necessary to assign values to A_O, a constant for the ion-oxygen atom repulsion and A_H, a

TABLE 4.4

Intermolecular Oxygen Atom Separation Distances for $R_{3,n} = 2.6A°$

n	Distance* A°
2	5.20(1)
3	5.07(3)
4	4.26(6)
5	3.67(6), 5.07(3), 5.2(1)
6	3.67(12), 5.20(3)

*The numbers in parentheses are the number of equal, distinct oxygen-oxygen distances in the cluster.

constant for the ion-hydrogen atom repulsion. Minimization of the total P.E. equations for $K^+(H_2O)$ with respect to $R_{i,j}$ leads to equation 4.22 from which A_O can be calculated

$$4.22 \quad \frac{\partial \text{ P.E.}}{\partial R_{i,j}} = -\sum_{i=1}^{3} \frac{(334)(Q_{ion})(Q_{i,j})}{R^2_{i,j}} + 4 \sum_{i=1}^{3} \frac{(167)(Q^2_{ion})(\alpha_{i,j})}{R^5_{i,j}} - 12 \left[\frac{A_H}{R^{13}_{1,1}} + \frac{A_H}{R^{13}_{2,1}} + \frac{A_O}{R^{13}_{3,1}} \right] = 0$$

as a function of $R_{i,j}$ assuming each value of $R_{i,j}$ corresponds to the equilibrium ion-ligand distance. The terms containing A_H may be expected to be negligible compared with the A_O terms. Firstly A_O is expected to be larger than A_H since the repulsion depends on the number of electrons associated with the atom (56). Also, the $R_{1,1}$ and $R_{2,1}$ distances are greater than $R_{3,1}$. Neglecting the A_H containing terms in equation 4.22 one obtains an equation of the general form 4.23 which gives A_O as a

$$4.23 \quad A_O = f(R_{3,1})$$

function of $R_{3,1}$. This function is shown in Figure 4.16. The potential energy of the cluster $K^+(H_2O)$ is given by equation 4.21 which depends on the parameters $R_{3,1}$ and A_O as indicated in equation 4.24. In order to obtain a value for A_O and $R_{3,1}$

$$4.24 \quad E_1 = F(A_O, R_{3,1})$$

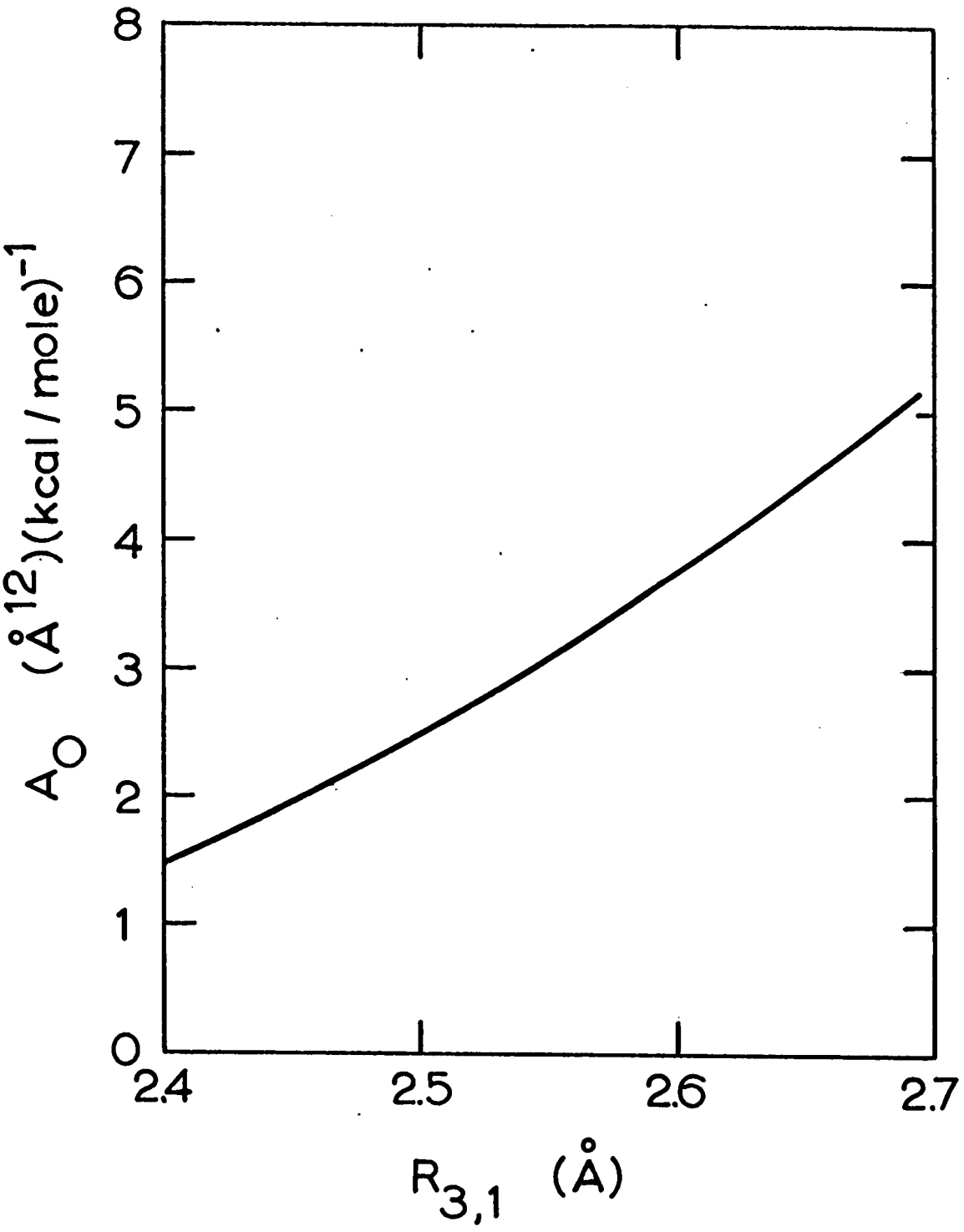

Figure 4.16 Plot of the ion-oxygen atom repulsion constant as a function of $R_{3,1}$. $R_{3,1}$ in this plot represents the ion-atom equilibrium distance as a variable.

at equilibrium we equate E_1 with the experimental $\Delta H_{0,1}$, which leads to 4.25. Expressions 4.23 and 4.25 represent

$$4.25 \qquad \Delta H_{0,1} = F(A_0, R_{3,1}) \qquad \text{(4.25)}$$

a system of two equations with two unknowns $(A_0, R_{3,1\ eq})$ which can be solved graphically. To do this $R_{3,1\ eq}$ is varied. The values of $R_{3,1}$ with the corresponding numbers for A_0 (obtained by 4.23) are substituted into equation 4.24. This procedure leads to the plot E_1 versus $R_{3,1}$ shown in Figure 4.17. The value of $R_{3,1}$ corresponding to the potential energy $E_1 = \Delta H_{0,1} = -17.9$ kcal is 2.56Å, the equilibrium distance. The associated value for A_0 from Figure 4.16 is $A_0 = 3.3 \times 10^{+5}$ Å^{12}/kcal/mole. This derived value of A_0 will also be used to calculate EREP and E_n for the higher clusters.

E_1 is shown as a function of $R_{3,1}$ in Figure 4.19. Also included in the Figure is a plot for E_6. Similar plots were done for the other clusters. The energy minima in these plots corresponding to the total calculated binding energy of the clusters relative to K^+ and H_2O molecules at infinite distance is $E°_n$. Thus $\Delta H_{n-1,n}$ should be compared with $E°_n - E°_{n-1} = \Delta E°_n$. Unfortunately the $E°_n$ values can not be too accurately estimated from the E_n curves (see Figure 4.19). This leads to a large error in $\Delta E°_n$.

To more accurately calculate $\Delta E°_n$, the following

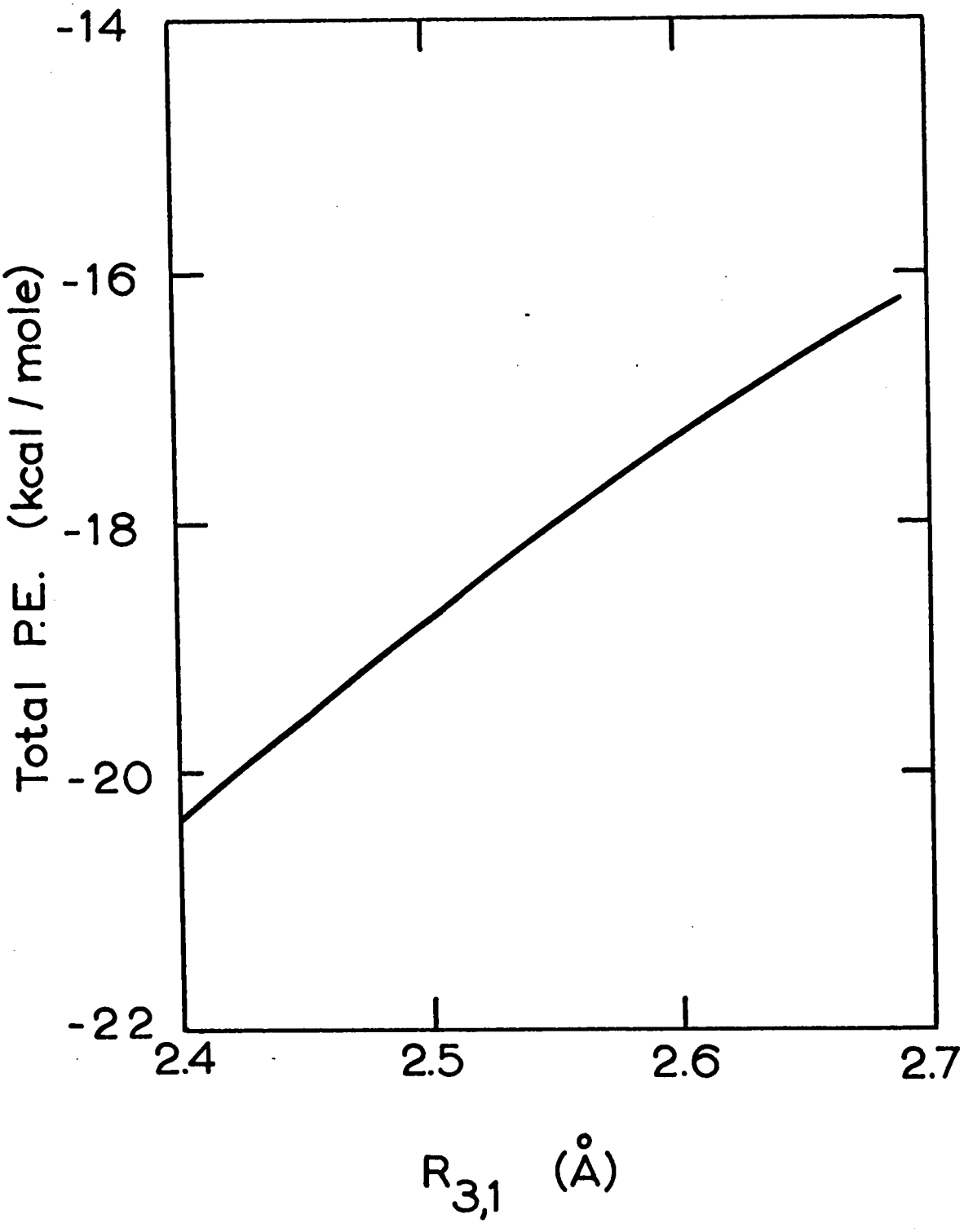

Figure 4.17 Plot of the total P.E. using the values of A_0 derived from Figure 4.16. $R_{3,1}$ in this plot is the equilibrium ion-atom distance.

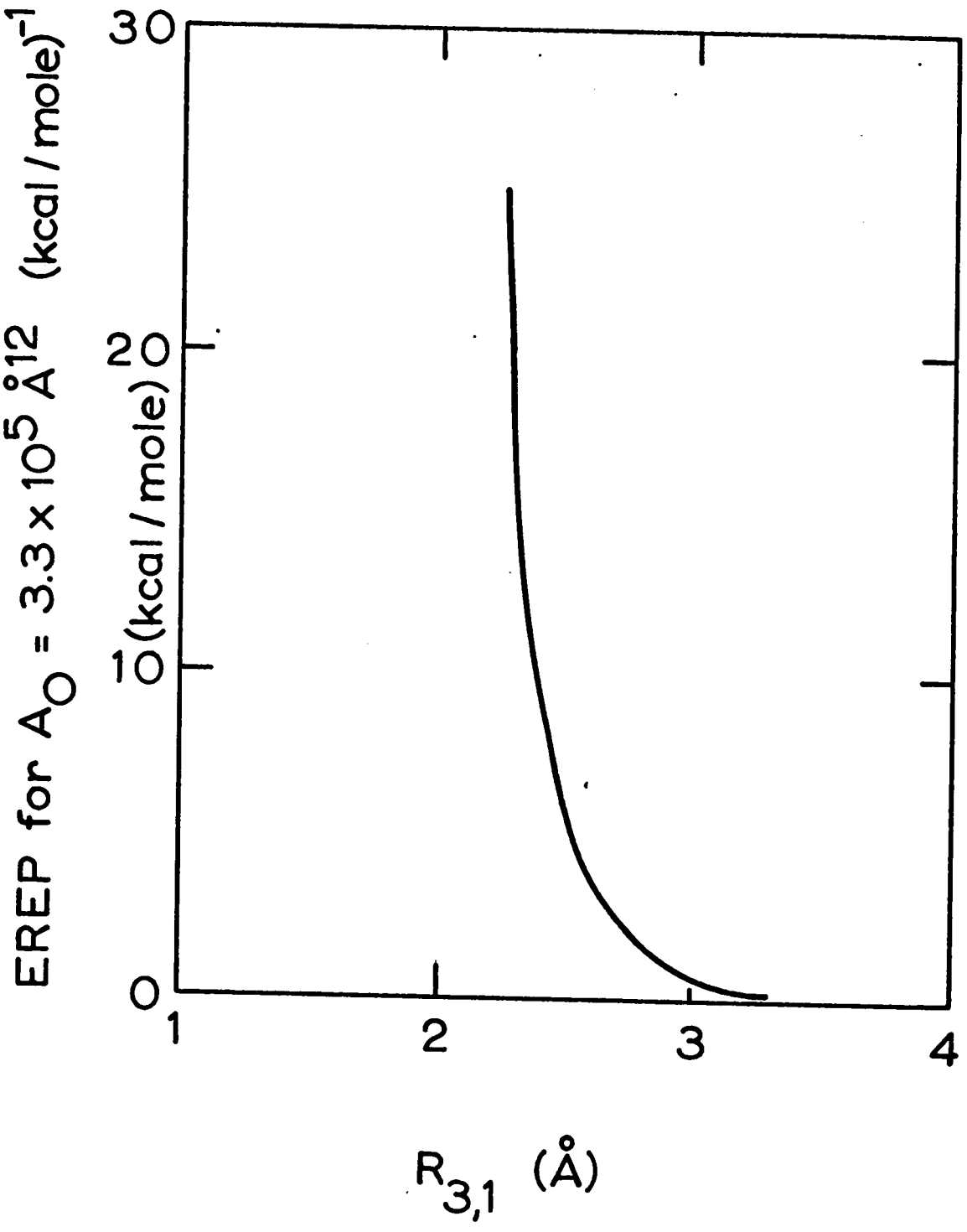

Figure 4.18 Plot of the ion-atom repulsion energy with the derived value for A_O, 3.3×10^5 Å^{12}/ (kcal/mole). $R_{3,1}$ is the ion-oxygen atom distance.

Figure 4.19 Plot of the potential energy evolved for the reactions $K^+ + H_2O \longrightarrow K^+(H_2O)$ and $K^+ + 6\ H_2O \longrightarrow K^+(H_2O)_6$.

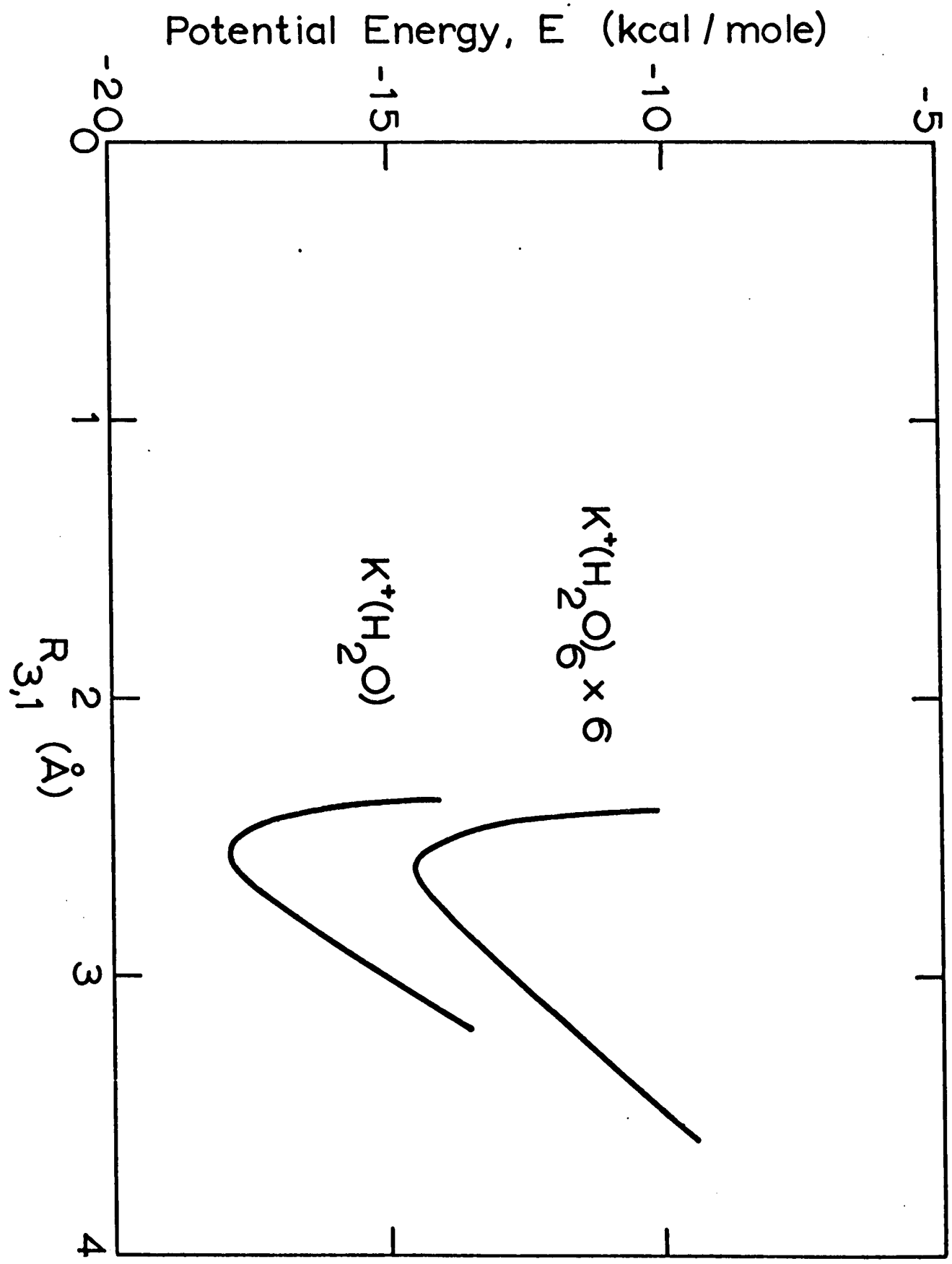

procedure was adopted. The equilibrium ion-ligand distance for all clusters was taken as 2.6Å. This approximation is satisfactory since the equilibrium distance increases only about 0.04Å from $K^+(H_2O)$ to $K^+(H_2O)_6$. The $\Delta E°_n$ calculated at 2.6Å are shown in Figure 4.20 for n=1 to n=6.

C. Comparison of Electrostatic Potential Energies with Previous Calculations

The calculations given in the previous section are similar to those of Garrick (28) who used a point dipole model to calculate the P.E. of a number of hydrated ions including $K^+(H_2O)_6$. The formulas were similar except for ion-molecule repulsion. Garrick used equation 4.26 which

$$\text{EREP} = \frac{n\,\lambda}{\nu-1}\, r^{-(\nu-1)} \qquad 4.26$$

was adapted from Lennard-Jones calculations of inert gas ion-atom repulsions. ν was a force index taken to be 10; λ was a calculated force constant; and n was the number of attached water molecules.

Garrick's *a priori* calculations for the hexahydrate gave the equilibrium distance between the point ion and point molecule as 2.58Å, EREP as 18 kcal/mole and EE + EPOL + EDIP as 102 kcal/mole, and the total P.E. as 84 kcal/mole. In comparison the values from this work are 2.56Å for the ion-oxygen atom distance, 19 kcal/mole for

EREP, 105 kcal/mole for (EE + EPOL + EDIP), and 86 kcal/mole total P.E. Our values are semi-empirical since the repulsive term was fitted so that the total P.E. at the equilibrium internuclear distance equalled the experimental value of $\Delta H_{0,1}$. The agreement between the calculations suggests that the point dipole model, which can be termed point ion-point molecule model is about as good an approximation as is the point ion-point atom model used in the present work.

Besides Garrick, Laidler (54) has performed point dipole P.E. calculations for a number of complex ions including $K^+(H_2O)_4$. Unfortunately the $K^+(H_2O)_4$ results were presented as a total of a cycle dealing with the heat of hydration of the potassium ion. However the individual energy contributions to the cycle are given for the ion $Rb^+(H_2O)_4$. Since the ionic radius of Rb is only 0.16Å larger than the radius of K^+ (45), one would expect the electrostatic energy of formation of $Rb^+(H_2O)_4$ to be slightly smaller than the energy of formation of $K^+(H_2O)_4$. The total P.E. for $Rb(H_2O)_4^+$ by Laidler's calculations is -61 kcal/mole while the corresponding energy for $K^+(H_2O)_4$ by the present calculations is -66 kcal/mole. One can also compare Laidler's values for the repulsion energy of $Rb(H_2O)_4^+$ (-7.6 kcal/mole), and $Li(H_2O)_4^+$ (-9.1 kcal/mole) to that of $K^+(H_2O)_4^+$ (-12 kcal/mole). Since both Laidler and this author used the same dependence of the repulsion, i.e.

equation 4.20, Laidler's value of A_o (which was not given in the paper) is either somewhat lower or $R_{3,1}$ somewhat higher than that derived in this work.

D. Discussion of Calculated $E°_n$ and Experimental $\Delta H°_{n-1,n}$

The purpose of the theoretical calculations was to provide an explanation for the observed changes in $\Delta H°_{n-1,n}$. Figure 4.20 shows a plot of $\Delta H°_{n-1,n}$ and $\Delta E°_n$ in function of n. According to the theoretical model, the decrease of $-\Delta E°_n$ with n is due to an increase in dipole-dipole repulsions. As can be seen from Figure 4.20 the electrostatic calculations result in values of $\Delta E°_n$ which qualitatively agree with the experimental $\Delta H°_{n-1,n}$. Thus the changes in $\Delta H°_{n-1,n}$ should be mostly due to increases in dipole-dipole repulsions.

In comparing the two plots shown in Figure 4.20 more closely, it is apparent that $-\Delta H°_{n-1,n}$ decreases more rapidly initially than $-\Delta E°_n$. This effect may be partly due to the naïve model used in the calculations. For example it has been proposed that the lone-pair oxygen electrons can screen the cation charge (57). The coordination of each succeeding water molecule will, therefore, involve a smaller release of energy. The inclusion of this effect in the electrostatic calculations would be expected to make the plot of

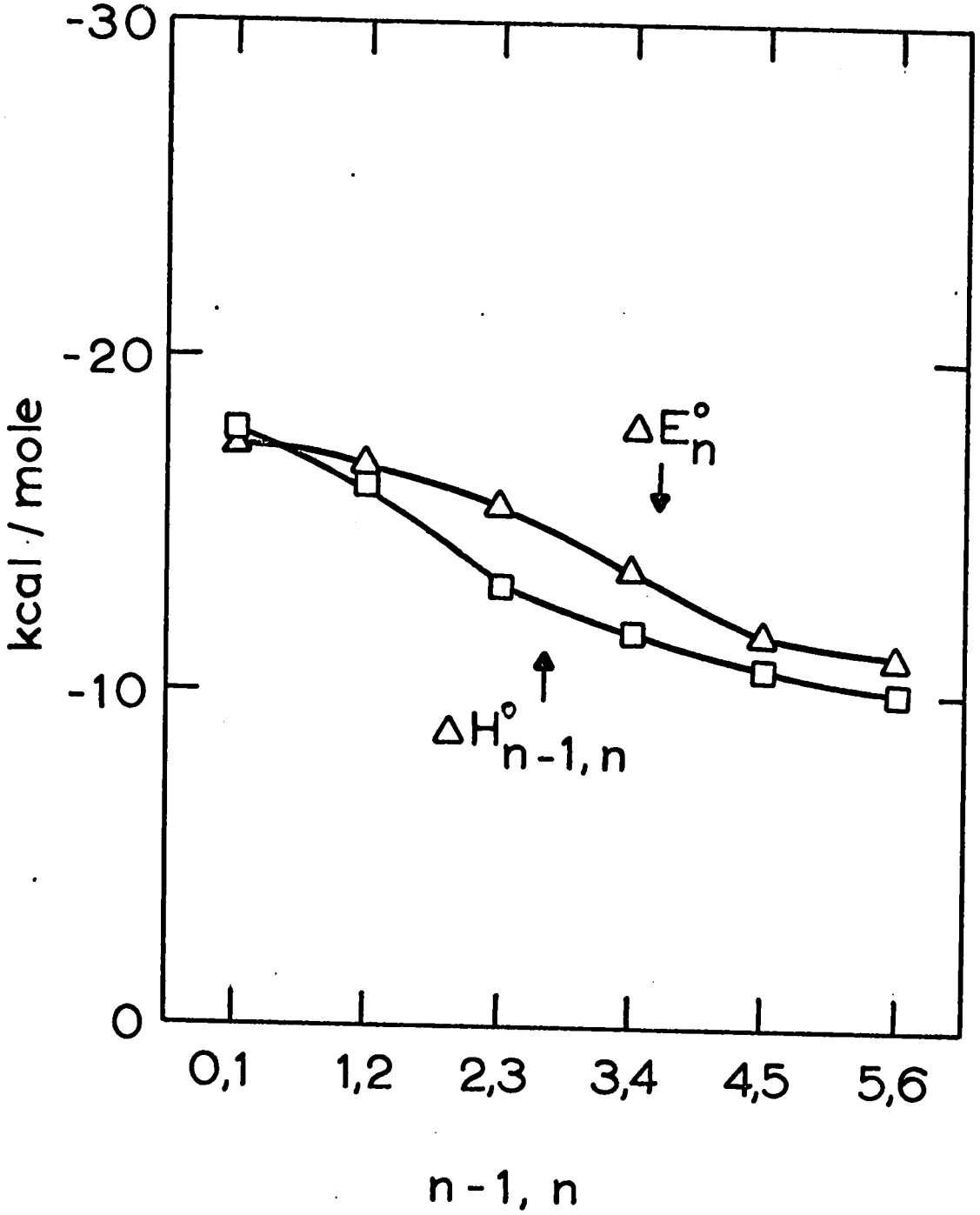

Figure 4.20 Comparison of the theoretical potential energy changes to the experimental $\Delta H^{\circ}_{n-1,n}$ for the reaction

$$K^{+}(H_2O)_{n-1} + H_2O \longrightarrow K^{+}(H_2O)_{n}$$

ΔE°_n vs. n-1,n more similar in shape to $\Delta H^\circ_{n-1,n}$ vs. n-1,n.

At n-1,n values greater than 5,6 it is expected that ΔE°_n will decrease much more rapidly due to rapid increases in dipole-dipole repulsion. As stated earlier the overall shape of ΔEDIP vs. n-1,n should be an exponentially increasing function. Since, by analogy to the $H^+(H_2O)_n$ results up to n = 8, the $\Delta H^\circ_{n-1,n}$ values are expected to be almost constant at high n-1,n, the present model would be unsatisfactory at high n-1,n. However, under these conditions the model should be modified to allow for the formation of an outer shell i.e. one in which the incoming water molecule hydrogen bonds to an existing ligand. The value of ΔE°_n can be calculated from the existing equations and use of the model shown in Figure 4.21. The model was chosen somewhat arbitrarily. The outer water molecule has been placed at a distance and a position corresponding to a normal hydrogen bond (58). From equations 4.17, 4.18, 4.20 and 4.21 the total energy release in coordination of the outer water molecule is -10.3 kcal/mole of which -4.8 kcal/mole is due to the hydrogen bond formation. The value -4.8 kcal/mole for the hydrogen bond formation compares to an experimental value of -5.0 kcal/mole (59). The formation of an outer complex would not be energetically expected to occur until equation 4.27 holds.

$$4.27 \quad -5.5 \text{ kcal/mole} + \Delta EDIP_{outer} \leq -17.6 \text{ kcal/mole} + \Delta EDIP_{inner}$$

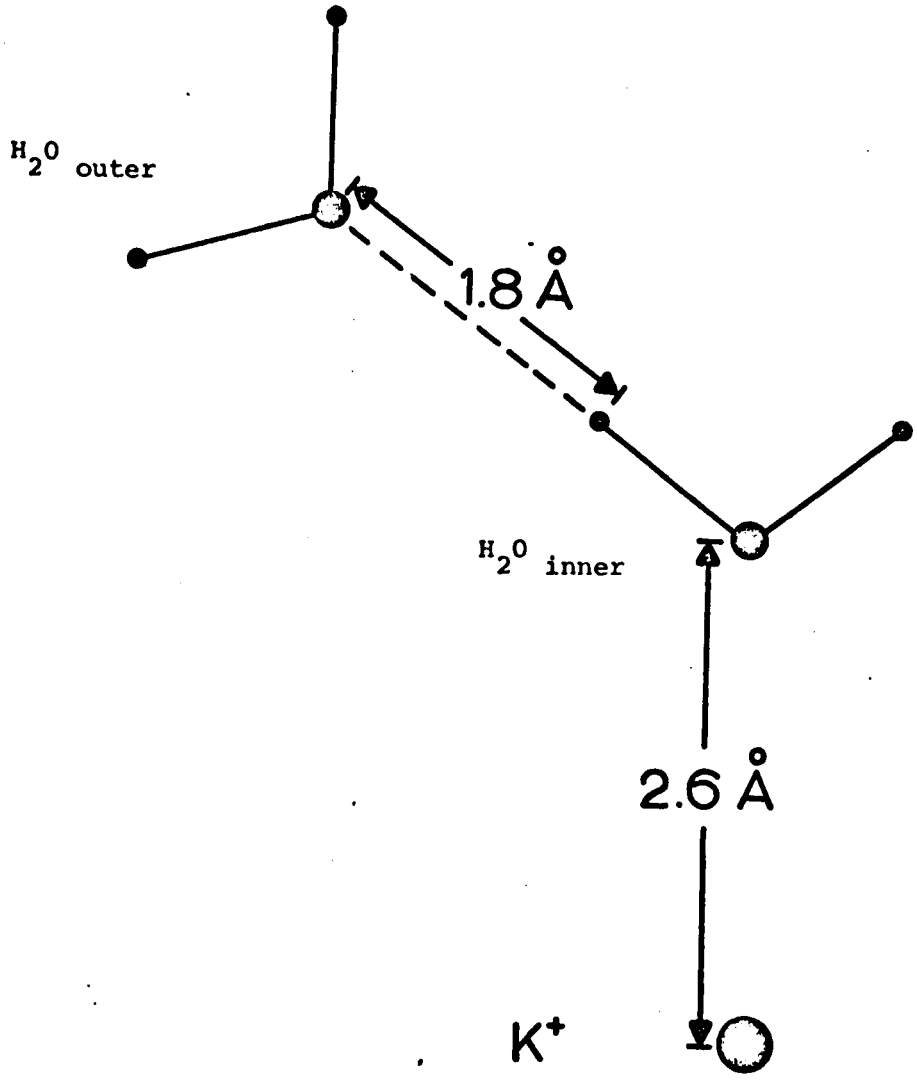

Figure 4.21 Model used to calculate the potential energy evolved for the reaction

$$K^+(H_2O)_{inner} + H_2O \longrightarrow K^+(H_2O)_{inner}\ (H_2O)_{outer}$$

In 4.27 $\Delta EDIP_{outer}$ is the increase in dipole-dipole repulsion in formation of the hydrogen bonded ligand while $\Delta EDIP_{inner}$ is the increase in dipole-dipole repulsion in coordination of the water molecule to the ion at the usual distance, $R_{3,n} = 2.6\mathring{A}$. The value -17.6 is the energy release exclusive of $\Delta EDIP$ in formation of the ion-water bond at $2.6\mathring{A}$ while -5.5 is the energy release exclusive of $\Delta EDIP$ in formation of the outer complex. From the model and the usual equations, the formation of the outer complex is 1.2 kcal/mole energetically unfavourable relative to the inner coordination for the addition of the 6^{th} water molecule. This suggests that the addition of the 7^{th} water may result in an outer complex. The plot of $\Delta E°_n$ vs. n-1,n would then be fairly constant at n-1,n greater than 5,6 in agreement with the expected trend in $\Delta H°_{n-1,n}$.

5. HYDRATION OF THE PROTON

SUMMARY

The hydrates $H^+(H_2O)_n$ were observed at water vapor pressures from 0.1 to 6 torr and temperatures of 25° to 600°C. The values of $K_{n-1,n}$, $\Delta H°_{n-1,n}$, $\Delta G°_{n-1,n}$, and $\Delta S°_{n-1,n}$ were determined for the reactions $H^+(H_2O)_{n-1} + H_2O \rightleftarrows H^+(H_2O)_n$ where n varied from 2 to 7.

These results are in general agreement with the values measured on a second mass spectrometer (AMS) by M. Arshadi and J. Scarborough (20). The AMS was operated at somewhat higher pressures over the temperature range from -17° to 125°C. Consequently the results from the AMS were for the reactions with n equals 4 to 8.

5.1 Reactions Leading to $H^+(H_2O)_n$

The main primary ions formed in the 100 kev proton beam are H_2O^+ and OH^+. These ions react rapidly to give H_3O^+.

5.1 $$H_2O^+ + H_2O \longrightarrow H_3O^+ + OH$$

5.2 $$OH^+ + H_2O \longrightarrow H_3O^+ + O$$

Using the thermal rate constant 6.0×10^{-10} cm^3/molecule sec (60), one can calculate that 99% of the primary ions react at 1 torr in 0.3 μsec. to yield H_3O^+. The further reactions of H_3O^+ are reactions 5.3 - 5.7.

5.3 $H_3O^+ + H_2O \xrightarrow{M} H^+(H_2O)_2$ (1,2)

5.4 $H^+(H_2O)_2 + H_2O \xrightarrow{M} H^+(H_2O)_3$ (2,3)

5.5 $H^+(H_2O)_3 + H_2O \xrightarrow{M} H^+(H_2O)_4$ (3,4)

5.6 $H^+(H_2O)_4 + H_2O \underset{\leftarrow}{\overset{M}{\rightarrow}} H^+(H_2O)_5$ (4,5)

5.7 $H^+(H_2O)_{n-1} + H_2O \underset{\leftarrow}{\overset{M}{\rightarrow}} H^+(H_2O)_n$ (n-1,n)

Since the attachment of water molecules to the ion is exothermic, third bodies indicated above as M are required for removal of the excess energy. A somewhat more detailed mechanism is given by equations 5.8 - 5.11

5.8 Association $H^+(H_2O)_{n-1} + H_2O \underset{\leftarrow}{\rightarrow} H^+(H_2O)_n^*$

5.9 Deactivation $H^+(H_2O)_n^* + H_2O \underset{\leftarrow}{\rightarrow} H^+(H_2O)_n + H_2O^*$

5.10 Dissociation $H^+(H_2O)_n + H_2O \underset{\leftarrow}{\rightarrow} H^+(H_2O)_{n-1} + 2H_2O$

5.11 Dissociation $H^+(H_2O)_n + H_2O \underset{\leftarrow}{\rightarrow} H^+(H_2O)_{n-1} + (H_2O)_2$

$H^+(H_2O)_n^*$ represents the species still containing the energy released by the condensation reaction. Dissociation may occur by the reverse reaction of 5.8, by 5.10 or by a lower energy path (relative to 5.10) through hydrogen bond formation as represented by reaction 5.11.

Provided that equilibrium is achieved, the relationship given by the following equation should be observed.

$$5.1 \qquad K_{n-1,n} = \frac{I_{H^+(H_2O)_n}}{I_{H^+(H_2O)_{n-1}} P_{H_2O}}$$

$I_{H^+(H_2O)_n}$ and $I_{H^+(H_2O)_{n-1}}$ are the mass analyzed ion currents of $H^+(H_2O)_n$ and $H^+(H_2O)_{n-1}$ respectively. P_{H_2O} is the water vapor pressure in the ion source.

5.2 Results

A. Values for $K_{n-1,n}$

Some representative data used to calculate $K_{n-1,n}$ is shown in Table 5.1. The mass spectrum is tabulated for various pressures and temperatures. Figures 5.1 - 5.7 show all the measured values for the equilibrium constants as a function of pressure. As illustrated by the plots, the equilibrium constants do not change significantly over the experimental pressure range.

B. Values for $\Delta H°_{n-1,n}$, $\Delta G°_{n-1,n}$, and $\Delta S°_{n-1,n}$ at 298°K

Values for $\Delta H°_{n-1,n}$ were determined from van't Hoff plots, log $K_{n-1,n}$ versus 1/T. The plots are shown in Figure 5.8. The results obtained by M. Arshadi and J. Scarborough (20), on a different mass spectrometer (AMS) are also shown. According to the van't Hoff relationship, equation 5.2, the slope of the plotted lines equals $-\Delta H°_{n-1,n}/2.3R$. Since within experimental error $\Delta H°$ was constant with temperature,

TABLE 5.1

Representative Data Given as the Mass Spectra in Per Cent Total Ionization

No.	Temp.* C° a	b	P. torr	Mass Spectrum of $H^+(H_2O)_n$ n=1	2	3	4	5	6	7	Total Ion Current A x 10^{14}
1	55	63	0.19			3.15	81.3	15.3	0.29		4
			0.30				74.3	25.0	0.70	0.015	7
			0.53				65.2	33.2	1.71	0.029	8
			0.59				58.4	39.3	2.37	0.036	6
			0.76				54.2	42.6	3.32	0.041	4
			1.50				46.4	48.6	5.0	0.081	0.6
	55	63	2.10				42.3	51.4	6.4		0.2
2	93	105	0.18			31.6	67.5	1.15			7
			0.34			16.8	80.4	2.77			12
			0.47			13.3	81.8	4.92			18
	92	105	0.65			11.9	83.0	5.16			6
			0.92			7.67	83.6	8.66			6
			1.45			8.92	81.0	10.0			2
			1.60			9.65	78.8	11.6			1
	93	108	2.30			10.3	75.5	14.3			0.2
3	232	235	0.38	59.4	40.5	0.25					3
			0.69	45.1	54.2	0.80					17
			0.85	24.2	74.3	1.39					19

TABLE 5.1 (Cont'd.)

No.	Temp.* C° a	b	P. torr	Mass Spectrum of $H^+(H_2O)_n$ n=1	2	3	4	5	6	7	Total Ion Current A x 10^{14}
			1.55	26.9	71.2	2.01					9
			1.95	24.6	75.4						8
			2.85	22.5	77.5						4
	232	235	3.50	20.7	79.3						3
4	335	315	0.85	2.86	89.6	7.54					90
			2.20	0.43	84.9	15.7					130
			3.30	0.82	79.5	19.7					70
			5.43		67.8	32.2					15
	333	315	6.21		65.1	34.9					11
5	600	493	0.80	78.6	21.4						55
			1.82	59.5	40.5						50
			2.17	56.2	43.8						30
	598	512	2.54	52.3	47.7						20
			3.24	46.1	53.9						15
	595	521	4.23	38.4	61.6						15

* a is the temperature of the thermocouple in the ion source bottom while b is the temperature of the thermocouple in the ion source top.

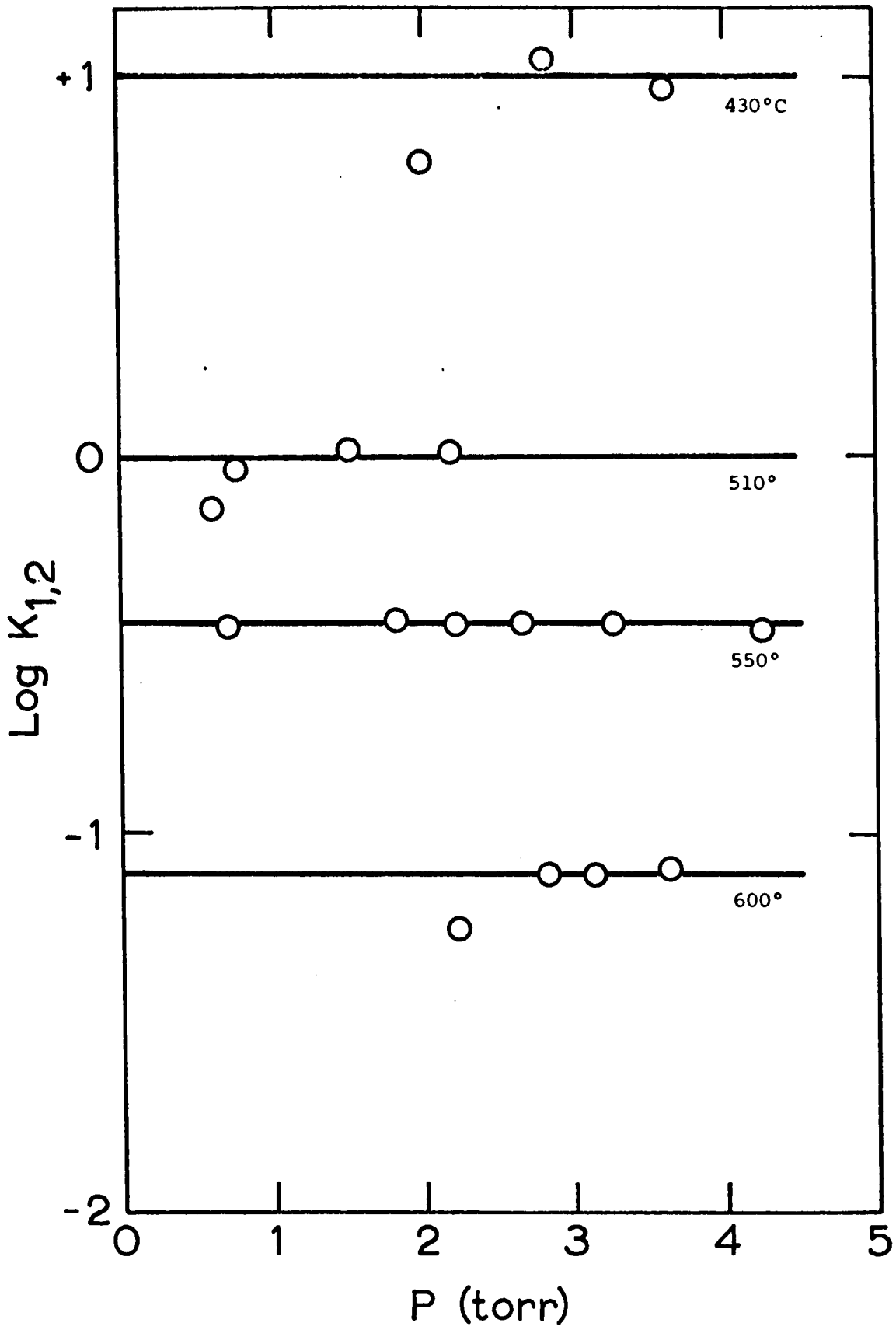

Figure 5.1 Plots of log $K_{1,2}$ versus pressure at various temperatures.

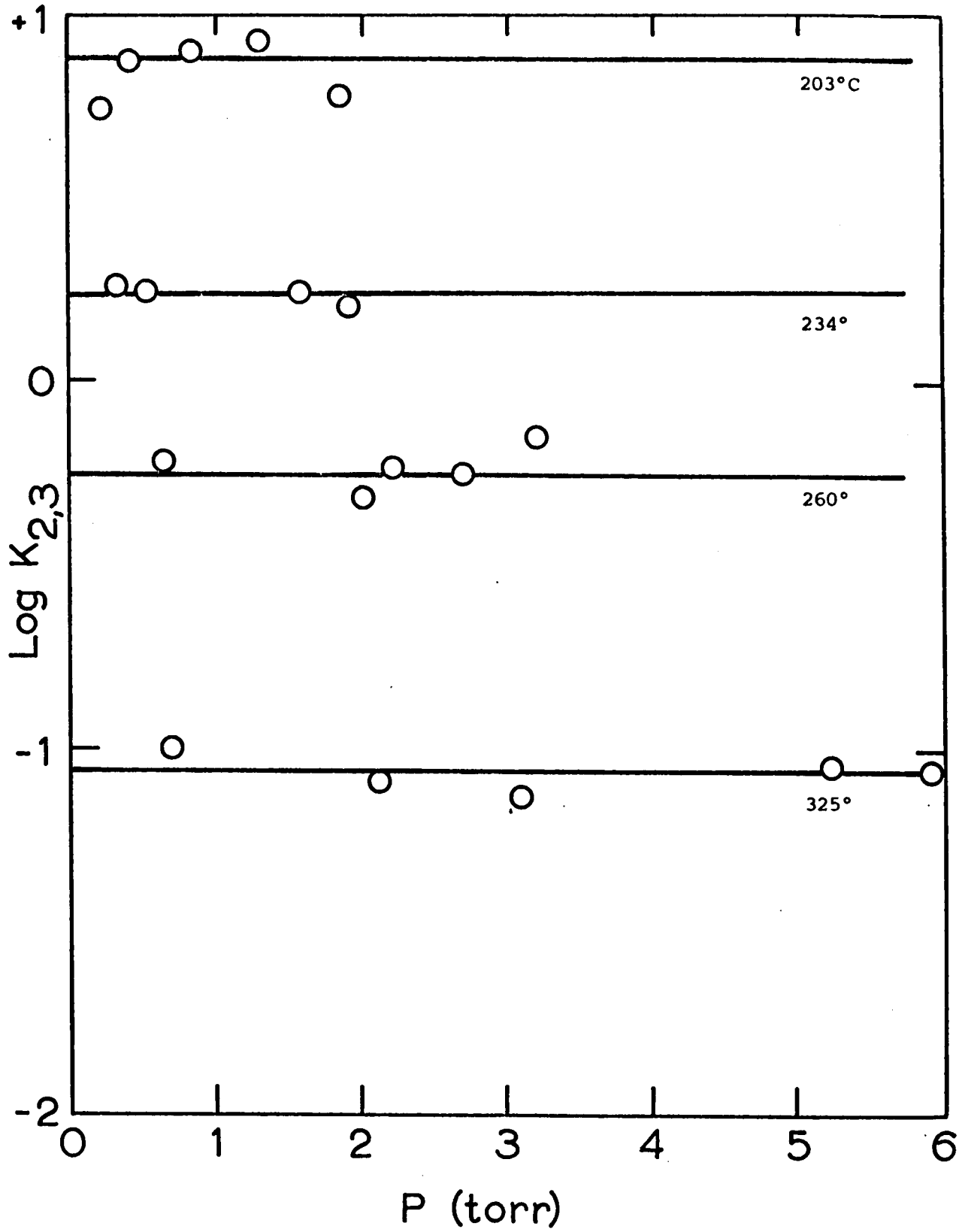

Figure 5.2 Plots of log $K_{2,3}$ versus pressure at various temperatures.

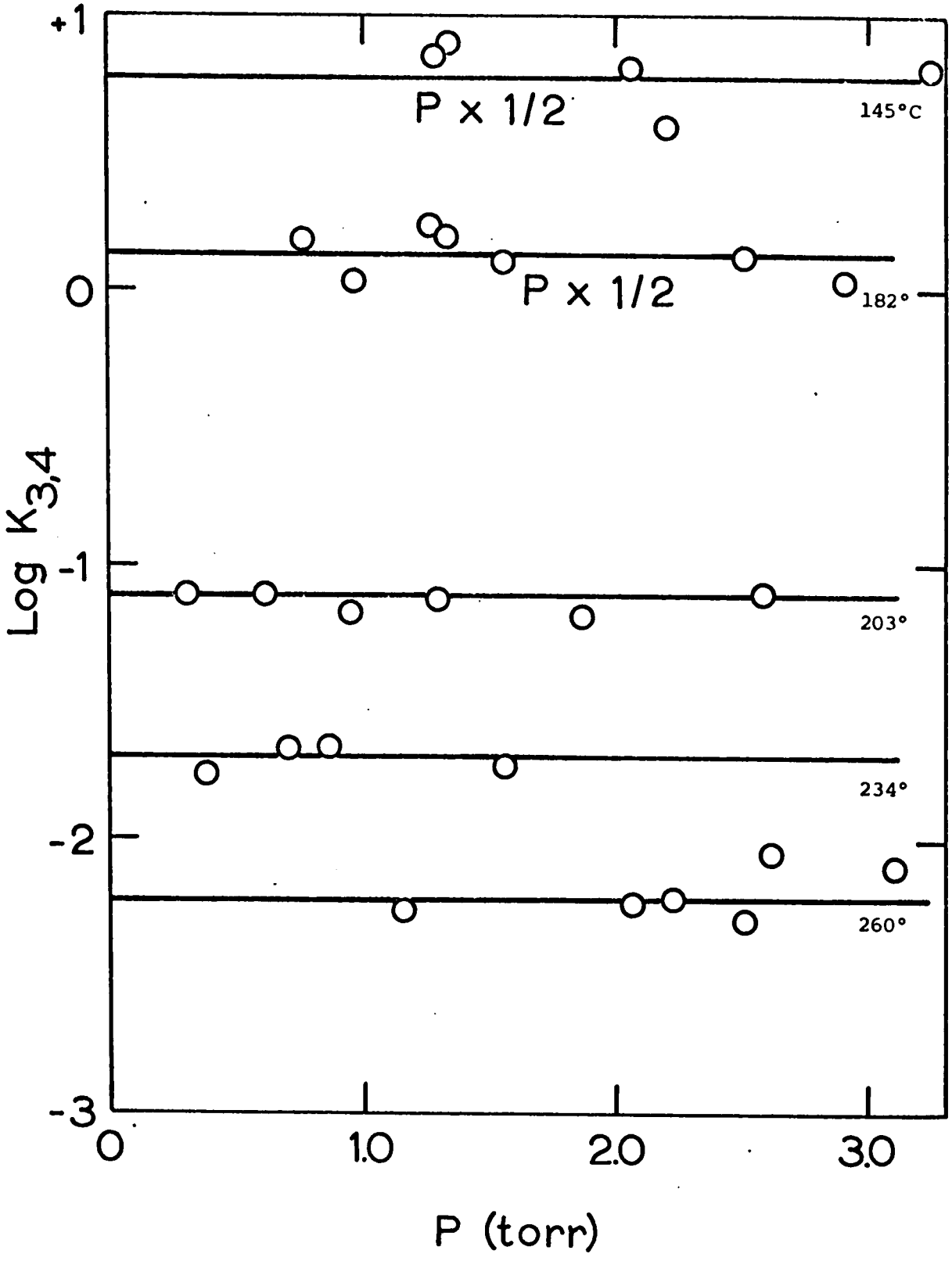

Figure 5.3 Plots of Log $K_{3,4}$ versus pressure at various temperatures.

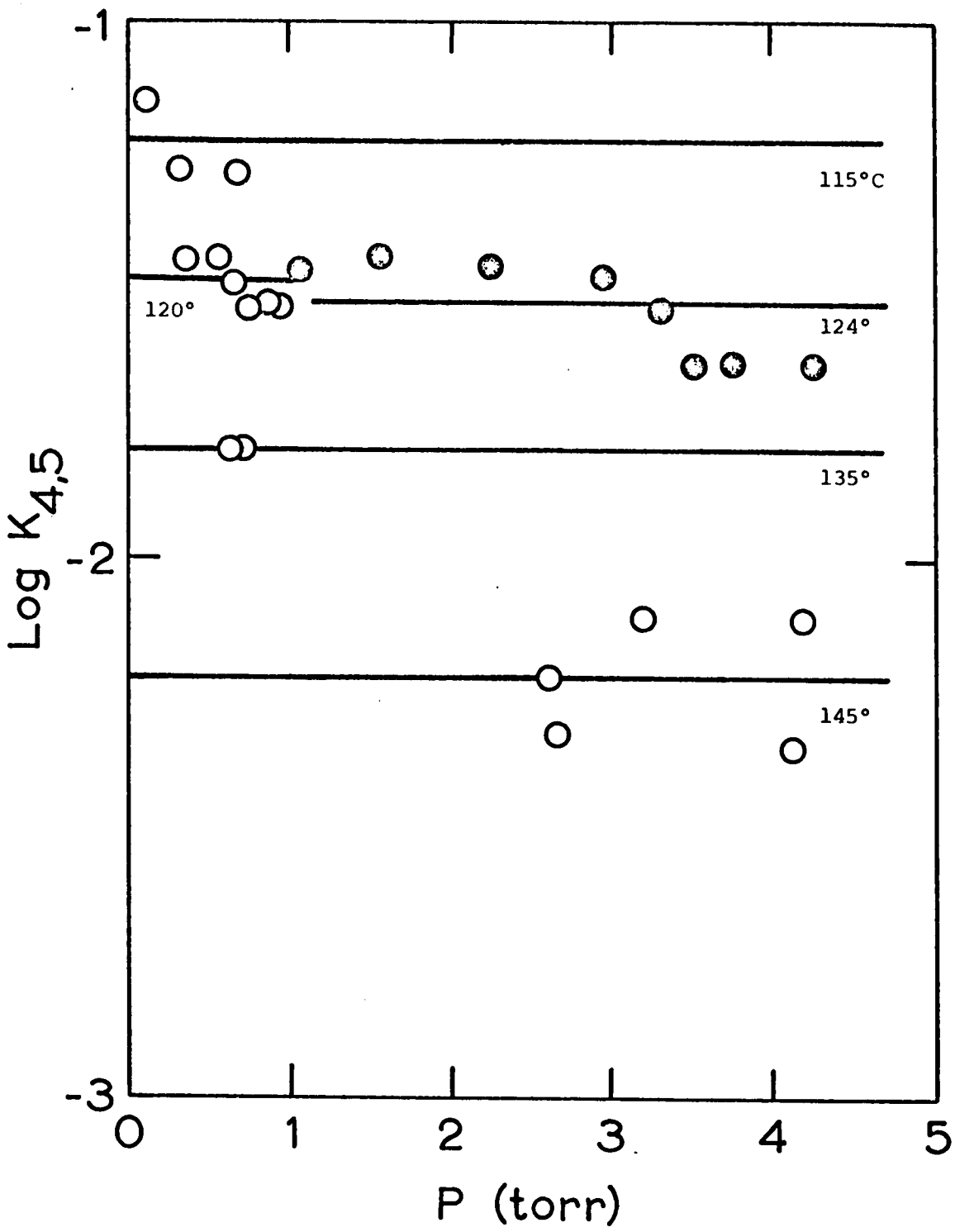

Figure 5.4 Plots of log $K_{4,5}$ versus pressure at various temperatures. Plots of log $K_{4,5}$ are continued on Figure 5.5.

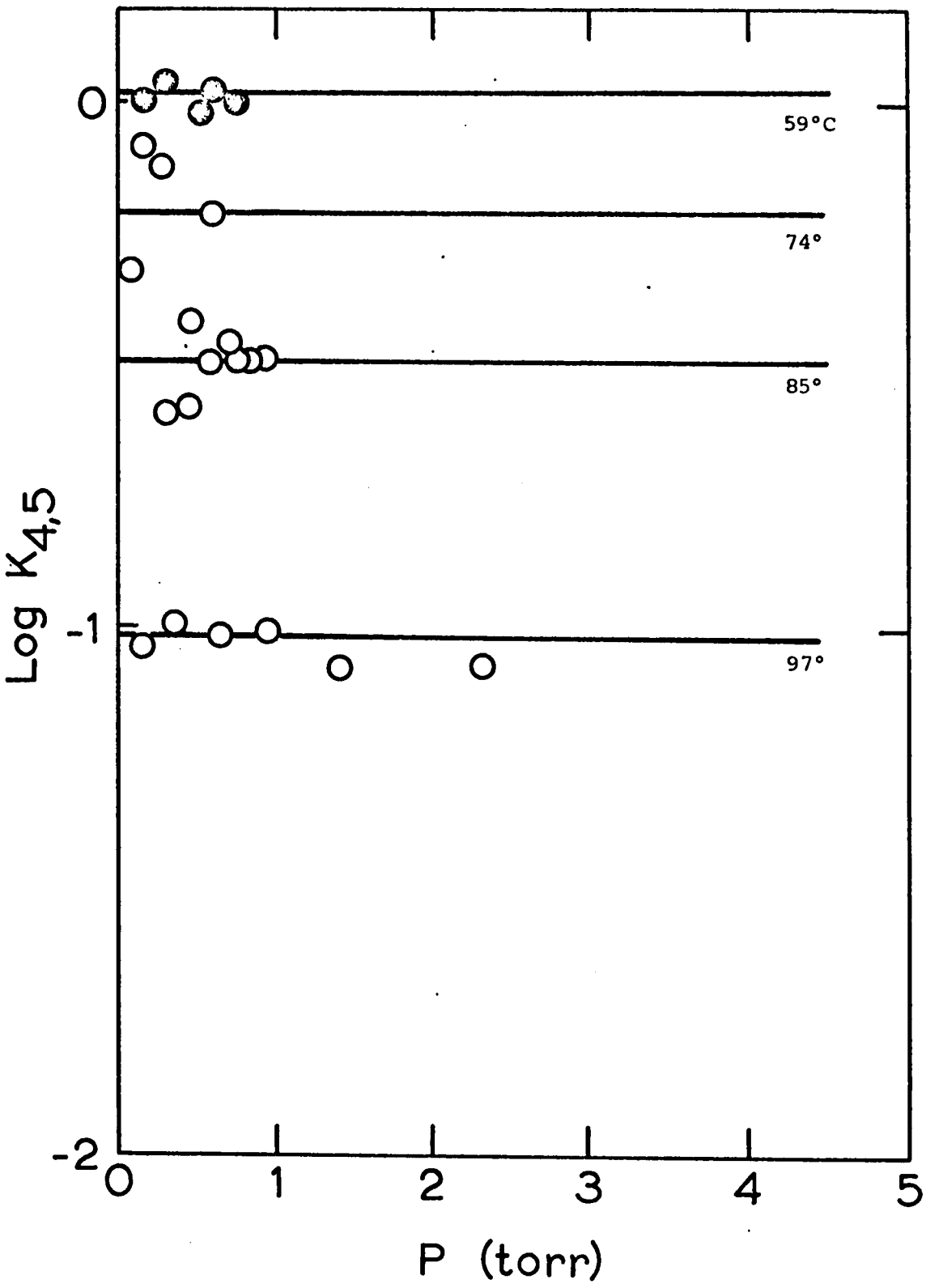

Figure 5.5 Continuation of log $K_{4,5}$ plots from Figure 5.4.

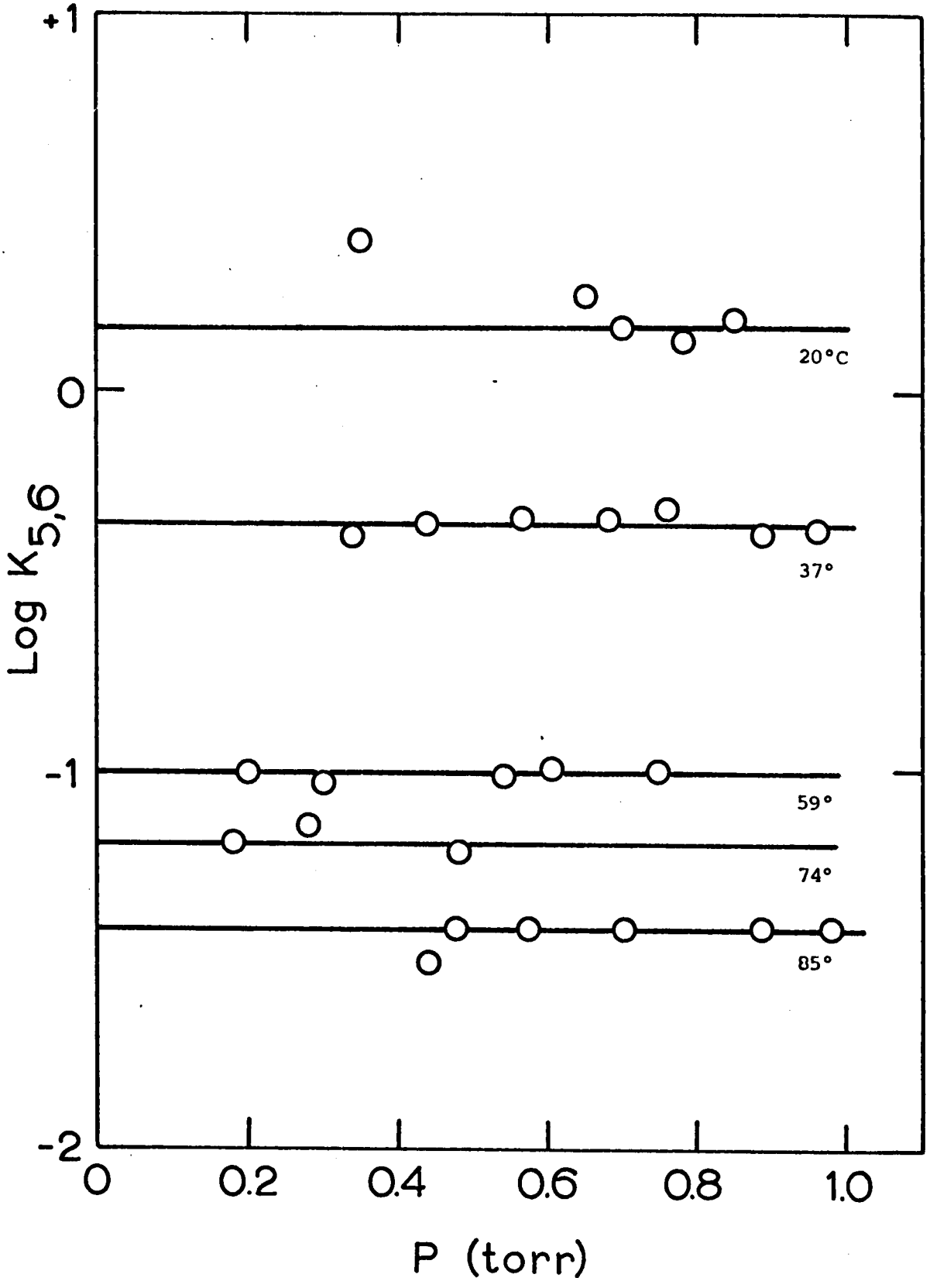

Figure 5.6 Plots of log $K_{5,6}$ versus pressure at various temperatures.

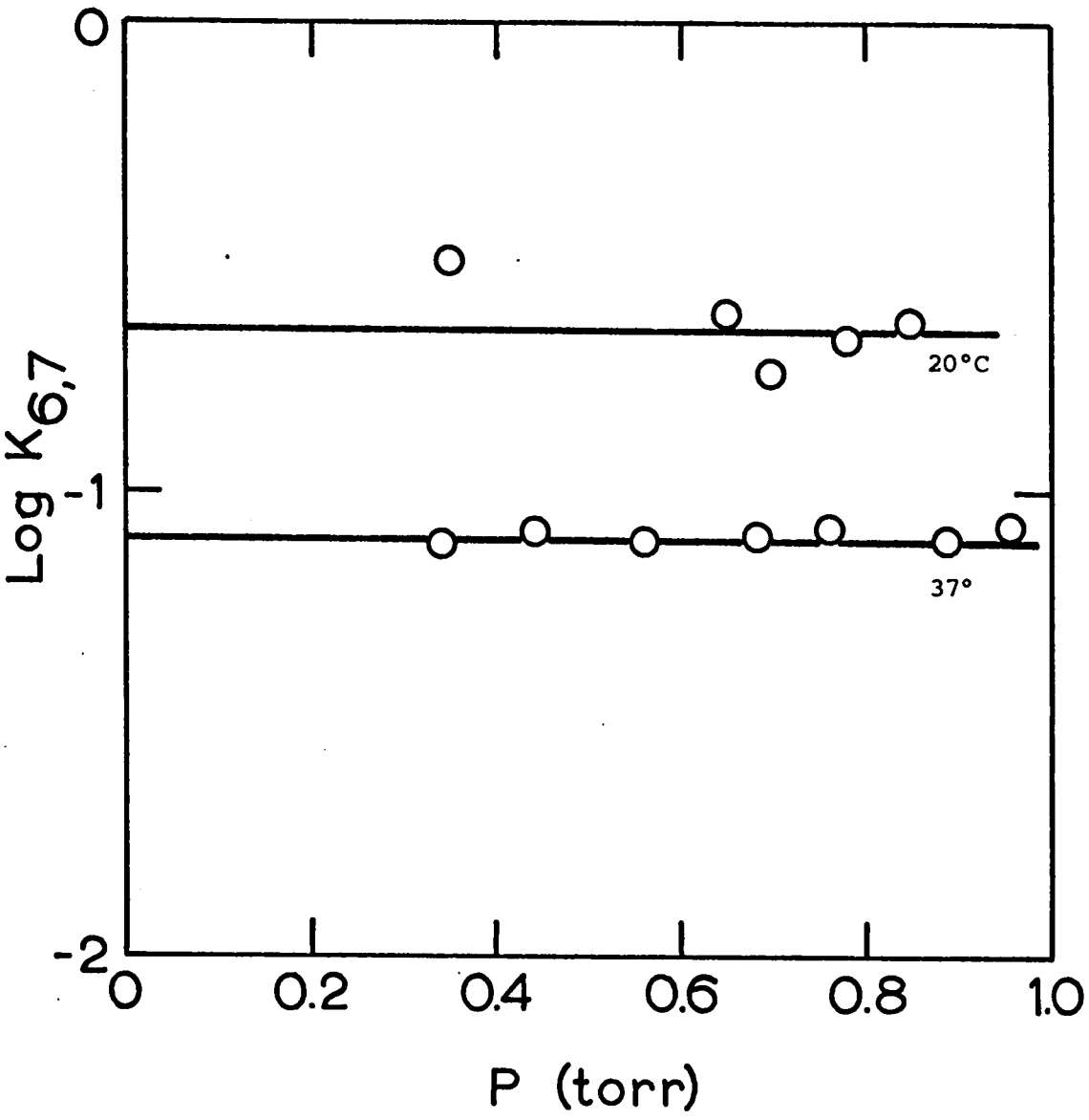

Figure 5.7 Plots of log $K_{6,7}$ versus pressure at various temperatures.

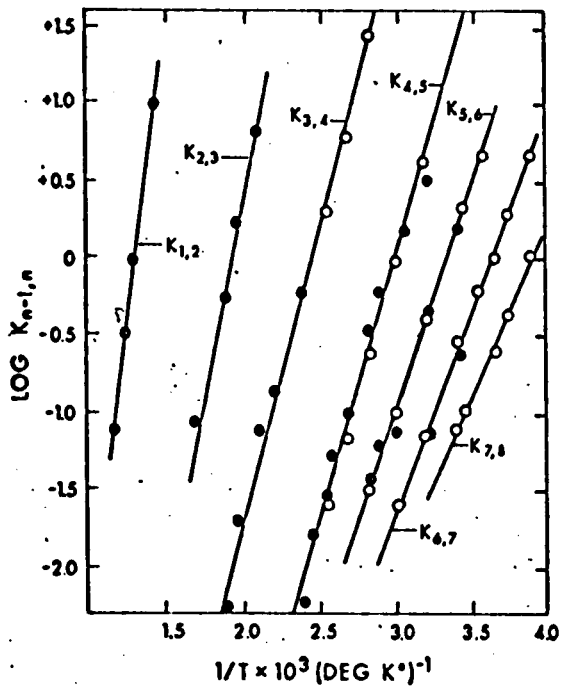

Figure 5.8

Van't Hoff-type plots of the equilibrium constants. O, AMS; ●, present results.

$$5.2 \qquad \log K_{n-1,n} = -\frac{\Delta H^\circ_{n-1,n}}{2.3\ RT} + \frac{\Delta S^\circ_{n-1,n}}{2.3\ R}$$

$\Delta H^\circ_{n-1,n}$ at 298°K is obtained from the slope and $\Delta S^\circ_{n-1,n}$ at 298°K is obtained from the intercept. $\Delta G^\circ_{n-1,n}$ at 298°K results from extrapolation of the straight line plots. The values for these thermodynamic functions are listed in Table 5.2.

C. Interpretation of the Van't Hoff Plots

Some comments are in order on the reliability of the values determined by the van't Hoff plots. First, because $\log K_{1,2}$ varied rapidly with K, the error in the slope due to the uncertainty in the temperature measurement (for example, the average temperature deviation in experiment 4 of Table 5.1 is 10° and in experiment 5 is 50°) leads to maximum uncertainties in ΔH°_{298}, ΔG°_{298}, and ΔS°_{298} of ±15%, ±20%, and ±25% respectively. The percentage error of ΔH was calculated by drawing error bars for the temperature on the van't Hoff plot and calculating $\Delta H^\circ_{1,2}$ from the steepest and shallowest lines which could be drawn through the error bars of all the points. The errors in ΔG°_{298} were obtained by extrapolation of the lines corresponding to the maximum and minimum values of ΔH°_{298}. The errors in ΔS°_{298} were calculated from the maximum ΔH°_{298} and ΔG°_{298} and minimum ΔH°_{298} and ΔG°_{298} values.

TABLE 5.2

Values for the Thermodynamic Functions for the Hydration of the Proton

	$-\Delta H°_{n-1,n}$ (kcal/mole)			$-\Delta G°_{298(n-1,n)}$ (kcal/mole)			$-\Delta S°_{298(n-1,n)}$ (e.u.)		
n-1,n	Combined	AMS	PMS*	Combined	AMS	PMS*	Combined	AMS	PMS*
0,1	169**								
1,2	36		36	25		25	33		33
2,3	22.3		22.3	13.6		13.6	29		29
3,4	17.2	18.3	18.8	8.5	9.6	9.5	28	32	32
4,5	15.3	15.7	15.3	5.5	5.6	5.5	33	34	33
5,6	13.0	13.3	13.0	3.9	3.9	3.9	30	31	30
6,7	11.7	11.7	11.7	2.8	2.8	2.8	30	30	30
7,8	10.3	10.3		2.2	2.2		27	27	

* PMS is the present work.

** From Reference (51).

In the van't Hoff plot for $K_{2,3}$ the line has been drawn more steeply than the "best" straight line through the points to make $\Delta S°_{298}$ fall in the range in which the other entropy values fell. $\Delta H°_{298}$, $\Delta G°_{298}$, and $\Delta S°_{298}$ for the "best" straight line are numerically smaller by 1.7 kcal/mole, 0.8 kcal/mole, and 3 e.u. respectively.

Combining the results from the two mass spectrometers has both an inherent advantage and disadvantage. If the deviation of the results from the best straight line through all of the points is due to random measurement errors, combining the points from the two instruments increases the accuracy of the results. However, if there is a systematic error between the two sets of results, combining the points increases the error. In the $K_{3,4}$ plot, separate lines drawn through each set of points results in a $\Delta H°_{3,4}$ value of -18.3 kcal/mole for the AMS and -18.8 kcal/mole for the PMS (the present results). The real value could be between -18.3 and -18.8 or it could be -17.2 kcal/mole considering the line through the combined results. Fortunately this is an extreme example since the other results in which both instruments were used to measure $K_{n-1,n}$ have better agreement either separately or combined.

5.3 Discussion of Results

A. The Hydrates as a Function of Pressure

As explained in section 4.3 the relative hydrate concentrations can be calculated by use of equation 4.13 and 4.14. The values for A and B are given in Table 5.3. Figure 5.9 illustrates the change in the hydrate concentrations with pressure at temperatures of 300° and 400°. This type of information is useful to radiation chemists studying the gas phase radiolysis of a polar molecule. For example Anderson (6) has attempted to explain a temperature effect in the γ-radiolysis of water vapor by the variation in the cluster size with temperature. The reactions which he considers are 5.12 and 5.13. The variation in cluster size is, therefore,

5.12 $$H_3O^+(H_2O)_n + e^- \longrightarrow H + (n+1)\ H_2O$$

5.13 $$H_3O^+ + e^- \longrightarrow 2H + OH$$

partly responsible for changing $G(H_2)$, according to Anderson.

B. Entropy Changes

As shown in section 4.3 a value can be theoretically calculated for the entropy loss in a condensation reaction. Comparison of the experimental and theoretical values gives an indication of the validity of the experimental results. Since the calculations depend on assumed structures, it is only practical to calculate the simplest case, $\Delta S^\circ_{1,2}$. The

TABLE 5.3

Constants for the Determination of $K_{n-1,n}$

Standard State 1 torr

n-1,n	A	B
1,2	7.82	10.1
2,3	4.76	9.05
3,4	3.63	8.86
4,5	3.33	10.0
5,6	2.84	9.46
6,7	2.53	9.24
7,8	2.17	8.50

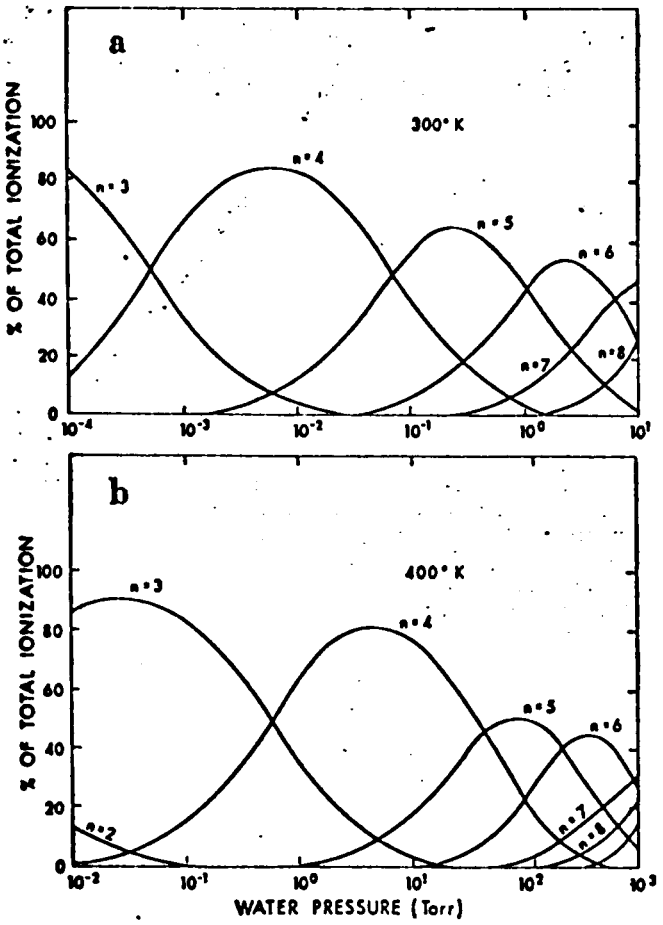

Figure 5.9

Equilibrium distributions of clusters $H^+(H_2O)_n$ predicted by experimental data; logarithmic scale used for water partial pressure in order to accomodate a wide pressure range: (a) 300°K, (b) 400°K. Distributions at other temperatures can be simply calculated from data in Table I.

translational entropy loss by the Sackur-Tetrode equation is -33 e.u. (See section 4.3 for an example of this type of calculation).

Using the assumed structures for H_3O^+ and $H^+(H_2O)_2$ shown in Figure 5.10, the rotational entropy change can be calculated from the type of equations given in section 4.3. The calculated moments of inertia are also given in Figure 5.10. The resulting theoretical rotational entropies are 14.2 e.u. for H_3O^+ and 9.8 e.u. for $H^+(H_2O)_2$. Using the value of 10.1 e.u. for H_2O calculated in section 4.3 $\Delta S°_{rot\ 1,2} = -5.7$ e.u.

In addition to the overall rotation there is an internal rotation $S°_{int\ rot}$ of the two H_2O groups in $H^+(H_2O)_2$ about their ion-dipole axes. The corresponding entropy term can be calculated from the partition function for free rotation (48) Q_{Fr} by equation 5.3 where the reduced

$$Q_{Fr} = \frac{1}{\sigma}\left(\frac{8\pi^3 I_r k T}{h^2}\right)^{\frac{1}{2}} \qquad 5.3$$

moment of inertia I_r is given by equation 5.4. For the complex under consideration I_1 equals I_2 equals

$$I_r = \frac{I_1 I_2}{I_1+I_2} \qquad 5.4$$

the moment of inertia about the ion dipole axis, 1.91×10^{-40} g cm^2.

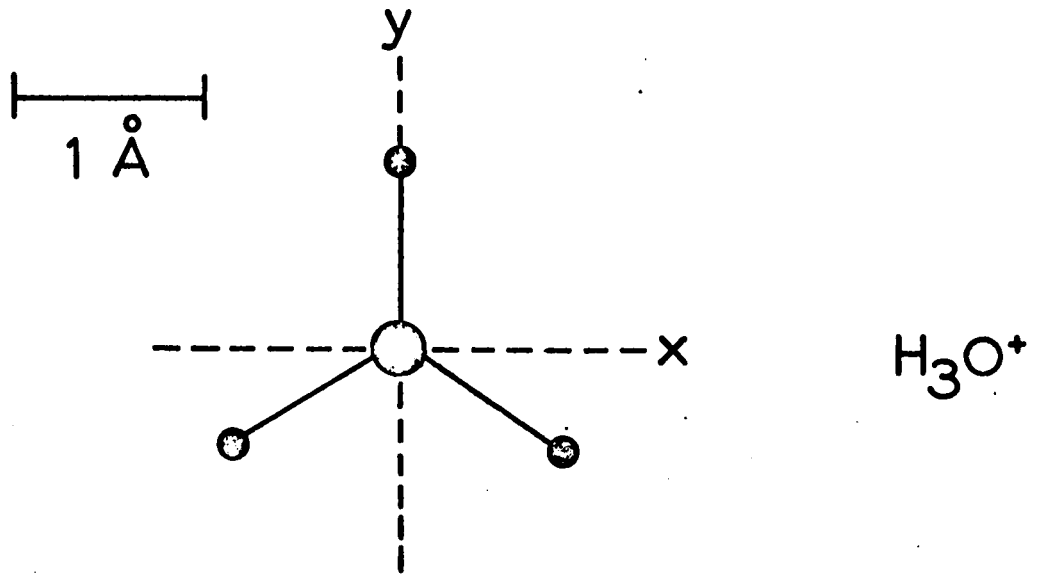

$I_x = I_y = 2.32$ $\qquad$ $I_z = 4.63 \times 10^{-40}$ g cm^2

$\sigma = 6$

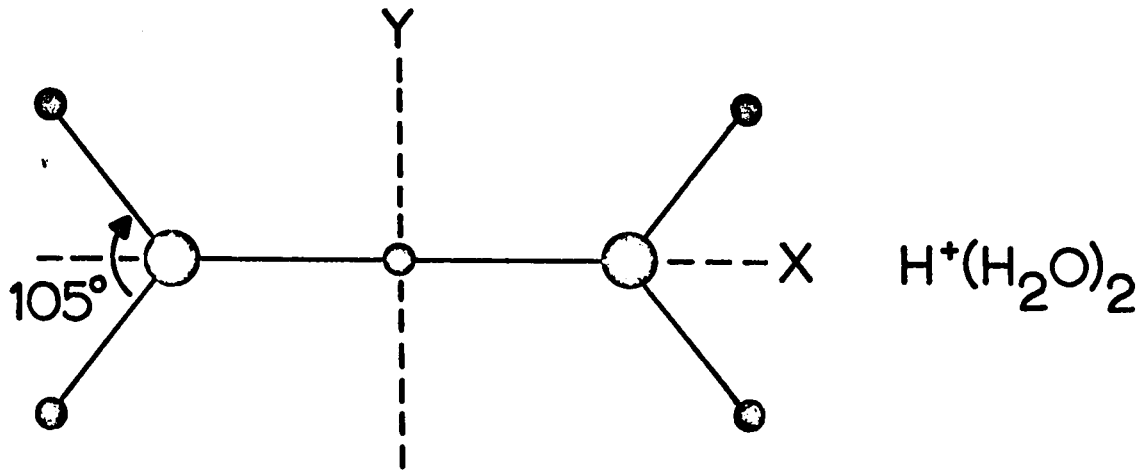

$I_x = 3.82$ $\qquad$ $I_y = 29.0$ $\qquad$ $I_z = 33.0 \times 10^{-40}$ g cm^2

$\sigma = 8$

Figure 5.10 Assumed structures of H_3O^+ and $H^+(H_2O)_2$ for the theoretical calculation of $\Delta S°_{1,2}$.

On substitution in equations 5.3 and 4.8, $S°_{int\ rot} = +4.7$ e.u.

The remaining terms needed to calculate $\Delta S°_{1,2}$ are vibrational. The magnitude of these terms is expected to be very small because of the large experimental values of $\Delta H_{0,1}$ and $\Delta H_{1,2}$ which are -169 (51) and -36 kcal/mole respectively. These values indicate a high bond energy. From equation 4.11 the torsional vibrations similar to those described for $K^+(H_2O)$ are expected to have a negligible entropy. The high bond energy also indicates that the force constants for the other vibrations are high. As can be seen from equations 4.10 and 4.11 this results in a small value for entropy for the new vibrations. We are naively assuming the original vibrations to be unchanged. Consequently taking $\Delta S°_{vib} = 0$ gives $\Delta S°_{1,2} = -34$ e.u. The difference between the theoretical and experimental entropy values, + 1 e.u., is certainly within the combined errors of theory and experiment.

C. Enthalpy Changes

The values of the thermodynamic functions for reaction 7,8 are compared to the values for the condensation of water vapor and the values for the gas phase reaction 5.14

5.14 $$H_2O + H_2O \rightleftharpoons (H_2O)_2$$

in Table 5.4. The fact that $\Delta H°_{7,8}$ is close to the heat of condensation of water need not mean that the effect of the

TABLE 5.4

Comparison of Values for the Thermodynamic Functions corresponding to the condensation of a water molecule onto $H^+(H_2O)_{7(g)}$ and $H_2O_{(g)}$ and into a pool of liquid water with a planar surface.

	$H^+(H_2O)_{7(g)}$	$H_2O_{(g)}$ [a]	$H_2O_{(l)}$ [b]
$\Delta H°_{298}$	- 10.3	- 5.0	- 10.52 kcal/mole
$\Delta G°_{298}$	- 2.2	+ 2.7	- 2.05 kcal/mole
$\Delta S°_{298}$	- 2.7	-25.8	- 28.39 e.u.

[a] From Reference (59).

[b] From Reference (61).

ionic change is negligible beyond the octahydrate. From the enthalpy given in Table 5.4 for reaction 5.14, it is apparent that the heat of condensation for a water molecule condensing onto a small electrically neutral gaseous nucleus is considerably less than the heat of condensation into liquid water with a planar surface.

One reason for this is that the enthalpy of condensation depends on the radius of curvature of the water surface. Dufour and Defay (62) estimate the heat of evaporation from a droplet of radius 10Å to be 0.94 of that from a plane surface. Extending the calculation to 4Å, an assumed value for the radius of the octahydrate, one obtains ΔH_{evap} (r = 4Å)/ΔH_{evap} (r = ∞) = 0.85, which gives 8.8 kcal/mole for the heat of evaporation from a neutral cluster with r = 4Å. Since the calculation depends on the macroscopic concept of surface tension, its extension to a 4Å radius is tenuous. However, the calculation does indicate that a significant fraction of $\Delta H_{7,8}$ is made up of ion-molecule attractions rather than molecule-molecule attractions.

D. The Structure of the Complex Ions

Consideration of the structure of $H_{2n+1}O_n^+$ involves two models. The first model is similar to that proposed for $K^+(H_2O)_n$, namely a central ion with coordinated water molecules. The central ions in the observed $H_{2n+1}O_n$ ions may be predominantly hydronium ions or hydrogen ions. The ion with molecular weight 19 is

undoubtedly H_3O^+ rather than $H^+(H_2O)$. The notation $H^+(H_2O)$ implies that all the ionic charge resides on one hydrogen, which is incorrect (63). The next ion in the series, molecular weight 37, can be represented equally well as $H^+(H_2O)_2$ or $H_3O^+(H_2O)$. One can think of the proton as being equally bonded to the two water molecules. If the higher hydrates are of the form $H_3O^+(H_2O)_\omega$, a break might be expected in the thermodynamic functions between reactions 5.15 and 5.16. The reason is that although the first three water molecules can coordinate to the hydrogen atoms of H_3O^+,

$$5.15 \quad H_3O^+(H_2O)_2 + H_2O \rightleftarrows H_3O^+(H_2O)_3$$

$$5.16 \quad H_3O^+(H_2O)_3 + H_2O \rightleftarrows H_3O^+(H_2O)_4$$

the fourth water molecule must coordinate in a new way. This way may be the formation of an outer complex of the type shown in Figure 4.21 or the coordination of the water molecule to the oxygen atom of the hydronium ion.

Figures 5.11 and 5.12 show $\Delta H°_{n-1,n}$ and $\Delta G°_{n-1,n}$ at 298°K as a function of n-1,n. These curves do not show any obvious breaks. For this reason the first derivative curves of $\Delta H°_{n-1,n}$ and $\Delta G°_{n-1,n}$ are also plotted in Figures 5.11 and 5.12 respectively. Although $\Delta(\Delta H°_{n-1,n})$ shows a slight break between reactions 5.15 and 5.16, $\Delta(\Delta G°_{n-1,n})$ does not. Although the possibility that H_3O^+ is the central ion is not ruled out since there is a slight break and since the $\Delta H°_{4,5}$ value from the present work is somewhat inaccurate due to a small curvature in the van't Hoff plot, it would appear that H^+ is more likely the central ion.

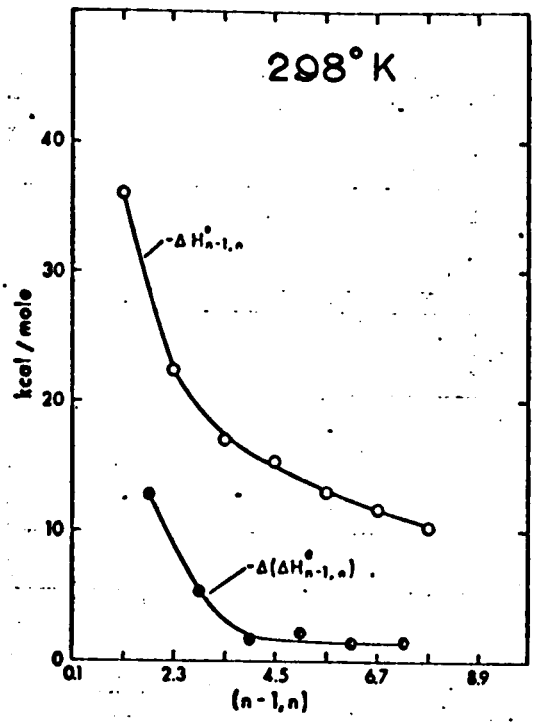

Figure 5.11

Plot of $\Delta H^{\circ}_{n-1,n}$ and $\Delta(\Delta H^{\circ}_{n-1,n})$ vs. n-1,n. The enthalpies of the reactions decrease quite regularly. A possible break is indicated between $\Delta H_{3,4}$ and $\Delta H_{4,5}$.

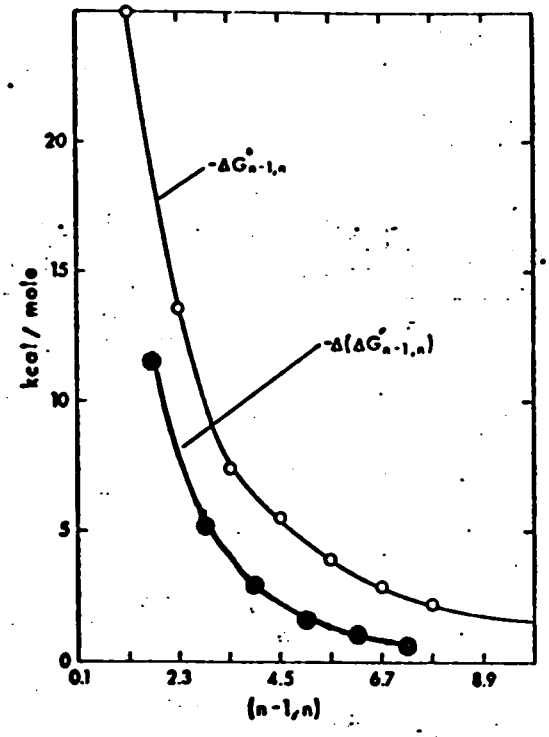

Figure 5.12

Plot of $\Delta G^{\circ}_{n-1,n}$ and $\Delta(\Delta G^{\circ}_{n-1,n})$ at 298°K vs. n-1,n. Standard state of water vapor is 1 atm. Decrease of free-energy changes is quite regular showing that stabilities of clusters change quite regularly.

This suggests a second model without a fixed central ion. In this model the ionic charge moves from molecule to molecule in the cluster by proton transfer. This model has as its basis the high proton mobility observed in liquid water. Such a model would suggest smooth changes in $\Delta H°_{n-1,n}$ and $\Delta G°_{n-1,n}$ with n-1,n since each successive condensation of a water molecule would give rise to similar interactions.

These two models are not very different if it is considered that $H^+(H_2O)_n$ and $H_3O^+(H_2O)_{n-1}$ are important transient structures in the mobile charge model.

6. SOLVATION OF THE AMMONIUM ION BY AMMONIA MOLECULES

6.1 Introduction

The study of the $NH_4^+(NH_3)_n$ system was undertaken to determine $\Delta H°_{n-1,n}$, $\Delta G°_{n-1,n}$, and $\Delta S°_{n-1,n}$ for reaction 6.1.

$$6.1 \quad (n-1,n) \quad NH_4^+(NH_3)_{n-1} + NH_3 \underset{\longleftarrow}{\overset{M}{\longrightarrow}} NH_4^+(NH_3)_n$$

The system $NH_4^+(NH_3)_n$ is of interest because of its similarity to $H^+(H_2O)_n$. In Chapter 5 the experimental thermodynamic values suggested that the hydrated species being investigated was $H^+(H_2O)_n$ rather than $H_3O^+(H_2O)_{n-1}$. Previous work by Kebarle (15) on reaction 6.1 for steps n-1,n = 2,3; 3,4; and 4,5 indicated the solvated species was $NH_4^+(NH_3)_n$. The structure was also indicated from a study of $NH_4^+(H_2O)_n$ by Hogg and Kebarle (17). The present work was done to obtain a complete set of thermodynamic data on reaction 6.1 to confirm or refute the structure $NH_4^+(NH_3)_n$.

6.2 Reactions Leading to $NH_4^+(NH_3)_n$

NH_3^+ and NH_2^+ are the main primary ions formed in the proton beam. As is the case in irradiated water vapor, the primary ions react rapidly to give a protonated species.

$$6.2 \quad NH_3^+ + NH_3 \longrightarrow NH_4^+ + NH_2$$

$$6.3 \quad NH_2^+ + NH_3 \longrightarrow NH_4^+ + NH$$

The thermal energy reaction rates of reactions 6.2 and 6.3

are 5.2×10^{-10} and 8.4×10^{-10} cm^3/molecule-sec. respectively (64). The further reactions of NH_4^+ are given by reactions 6.4, 6.5, and 6.1 where M is a third body to remove the energy released on condensation. The equilibrium constant

6.4 (0,1) $$NH_4^+ + NH_3 \xrightarrow{M} NH_4^+(NH_3)$$

6.5 (1,2) $$NH_4^+(NH_3) + NH_3 \xrightarrow{M} NH_4^+(NH_3)_2$$

$K_{n-1,n}$ is given by equation 6.1 where $I_{NH_4^+(NH_3)_n}$ and $I_{NH_4^+(NH_3)_{n-1}}$

6.1 $$K_{n-1,n} = \frac{I_{NH_4^+(NH_3)_n}}{I_{NH_4^+(NH_3)_{n-1}} P_{NH_3}}$$

are the mass analyzed ion currents of $NH_4^+(NH_3)_n$ and $NH_4^+(NH_3)_{n-1}$ respectively. P_{NH_3} is the pressure of ammonia in the ion source.

6.3 Effect of Ion Exit Slit Dimensions on Results

The dimensions of the ion exit slit in the ion source were found to affect the results. Initially the equilibrium constants were measured at temperatures up to 590°C with a 5μ x 4 mm ion exit slit. At 590°C the measurement of $K_{0,1}$ was interfered with by the presence of an impurity which gave an ion current of K^+ which was seventy times larger than the total ion current due to $NH_4^+(NH_3)_n$. Consequently the temperature was reduced to 330°C and the constants $K_{0,1}$ and $K_{1,2}$ were measured. These values were erroneous. $K_{0,1}$ was a factor of two lower and $K_{1,2}$ ten times higher

than the previous results predicted. On inspection of the ion source ion exit slit, it was found that the slit had buckled upon cooling from 590°C. The area of the buckled slit was much larger than the original area. A new ion exit slit was made 15μ x 1.7 mm. The equilibrium constants measured with this slit installed in the ion source were in agreement with the undistorted 5μ x 4 mm slit as shown in Figure 6.8.

At low temperatures the results using the 15μ x 4 mm slit became unacceptable. Figure 6.1 shows the constants measured as a function of pressure at -32°C. At a pressure of 0.57 torr an increase in the ion acceleration potential between the ion source and the first acceleration plate (draw-out plate) from 360 v to 550 v changed $K_{3,4}$ from 6.0 to 1.4. This indicates that a substantial proportion of the mass analyzed ions have undergone a collision just outside the ion source. The higher ion acceleration causes a greater number of ionic clusters to undergo dissociative collisions.

To reduce the number of collisions outside the ion source, the ion exit slit area was reduced by about a factor of five. The new dimensions were 1.5μ x 3.5 mm. The measurements of the constants with this slit in the ion source gave pressure independent equilibrium constants at all temperatures as illustrated in Figures 6.4, 6.5, 6.6,

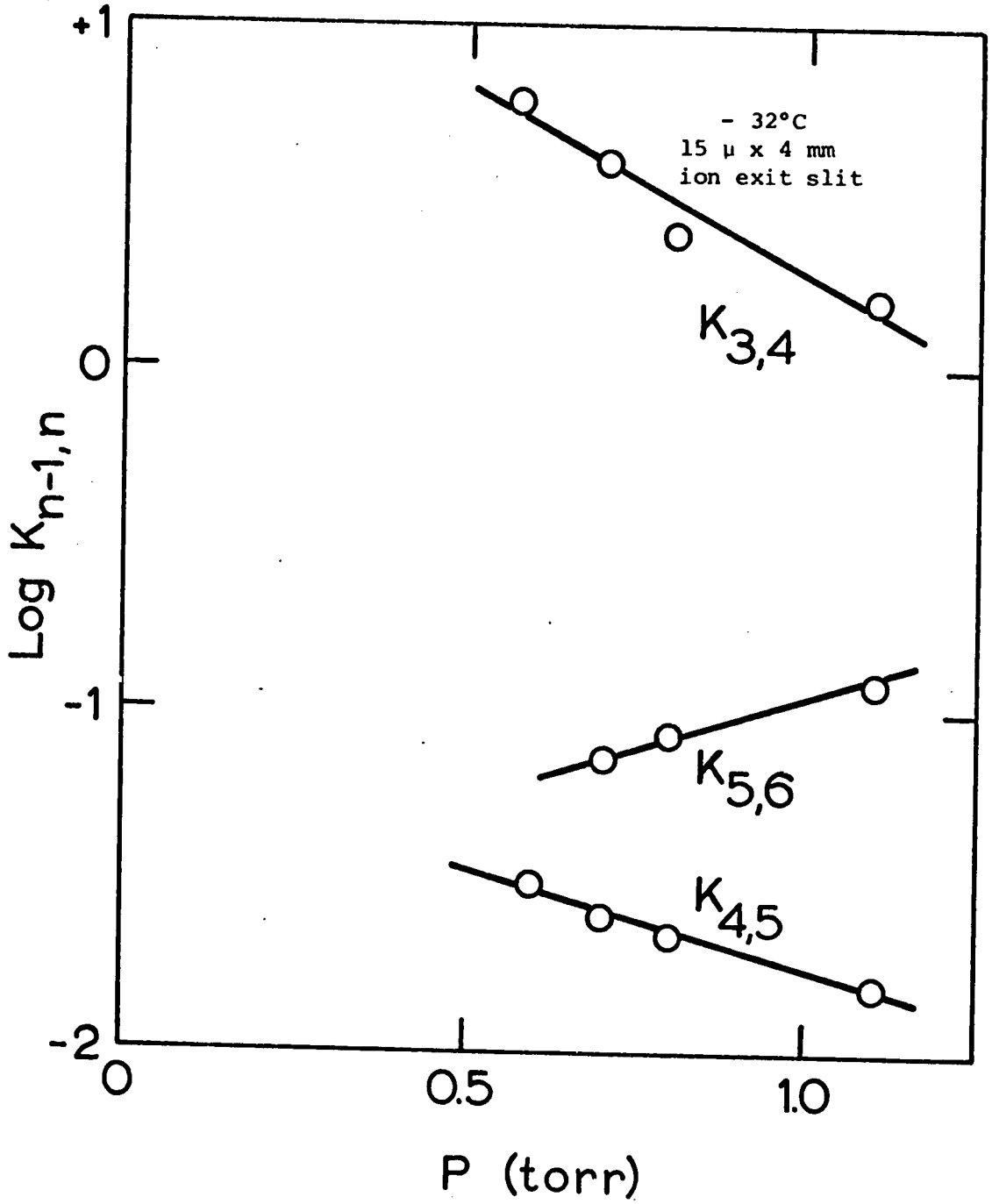

Figure 6.1 Equilibrium constants affected by collisions outside the ion source.

and 6.7. The constants were also in agreement with the previously measured constants which are also shown in Figures 6.4, 6.5, 6.6, and 6.7,

6.4 Results

Some representative mass spectra are listed in Table 6.1 Figures 6.2 - 6.7 show the plots of $K_{n-1,n}$ versus ammonia pressure obtained at temperatures from -57° to 485°C. Figure 6.8 shows van't Hoff type plots of the equilibrium constant. Values for the thermodynamic functions $\Delta H°_{n-1,n}$, $\Delta G°_{n-1,n}$, and $\Delta S°_{n-1,n}$ at 298°K obtained from equation 5.2 are listed in Table 6.2. Included in Table 6.2 are the values obtained by Hogg, Haynes, and Kebarle (15). The free energy values are seen to be in good agreement, although the enthalpy and entropy values are not in good agreement. Table 6.2 does not include values for reaction 5,6 because of insufficient data.

6.5 Discussion

A. $NH_4^+(NH_3)_n$ as a Function of Pressure

By the method outlined in section 4.3 the relative ionic concentrations can be calculated by use of equations 4.13 and 4.14. The values for A and B are listed in Table 6.3. Figure 6.9 illustrates the change in relative concentrations as a function of ammonia pressure at 300°K. As explained in section 5.3 the cluster concentrations are of interest to radiation chemists studying the vapor phase radiolysis of a polar molecule.

B. Entropy Changes

The entropy change occurring in reaction 6.4 is

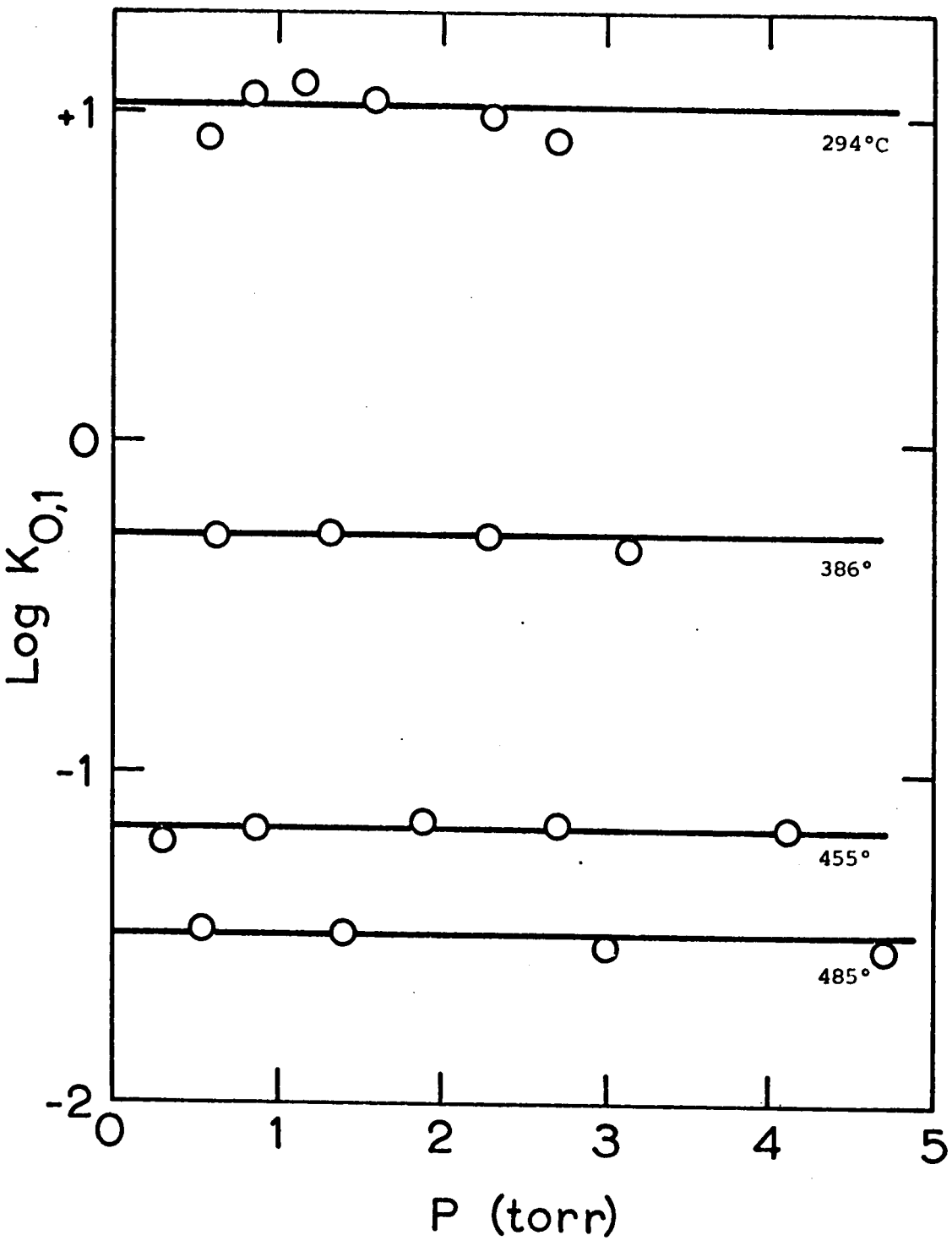

Figure 6.2 Plots of log $K_{0,1}$ versus pressure at various temperatures. O, 5 μ x 4 mm ion exit slit dimensions.

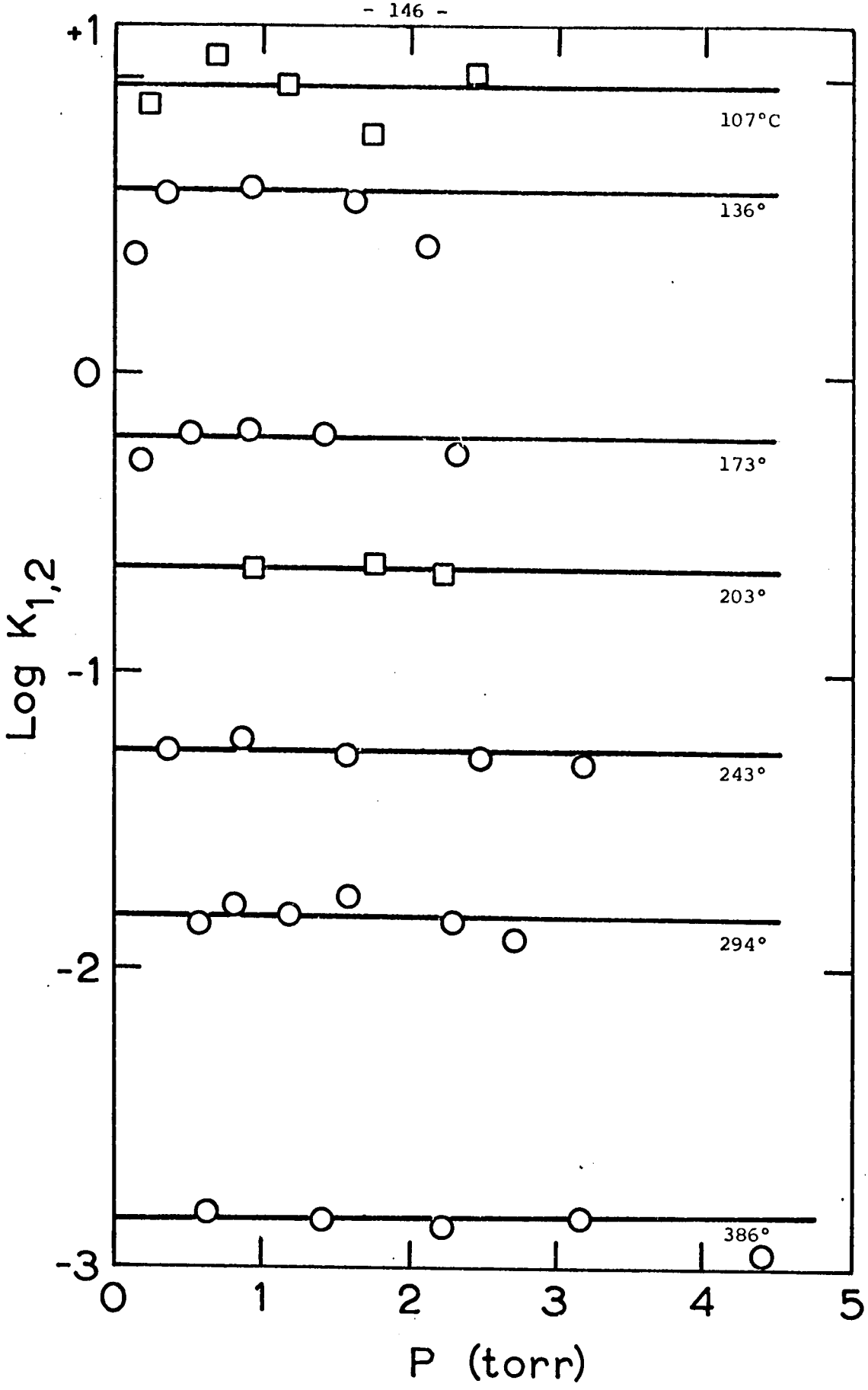

Figure 6.3 Plots of Log $K_{1,2}$ versus pressure at various temperatures. O, 5 μ x 4 mm; □, 15 μ x 1.7 mm ion exit slit dimensions.

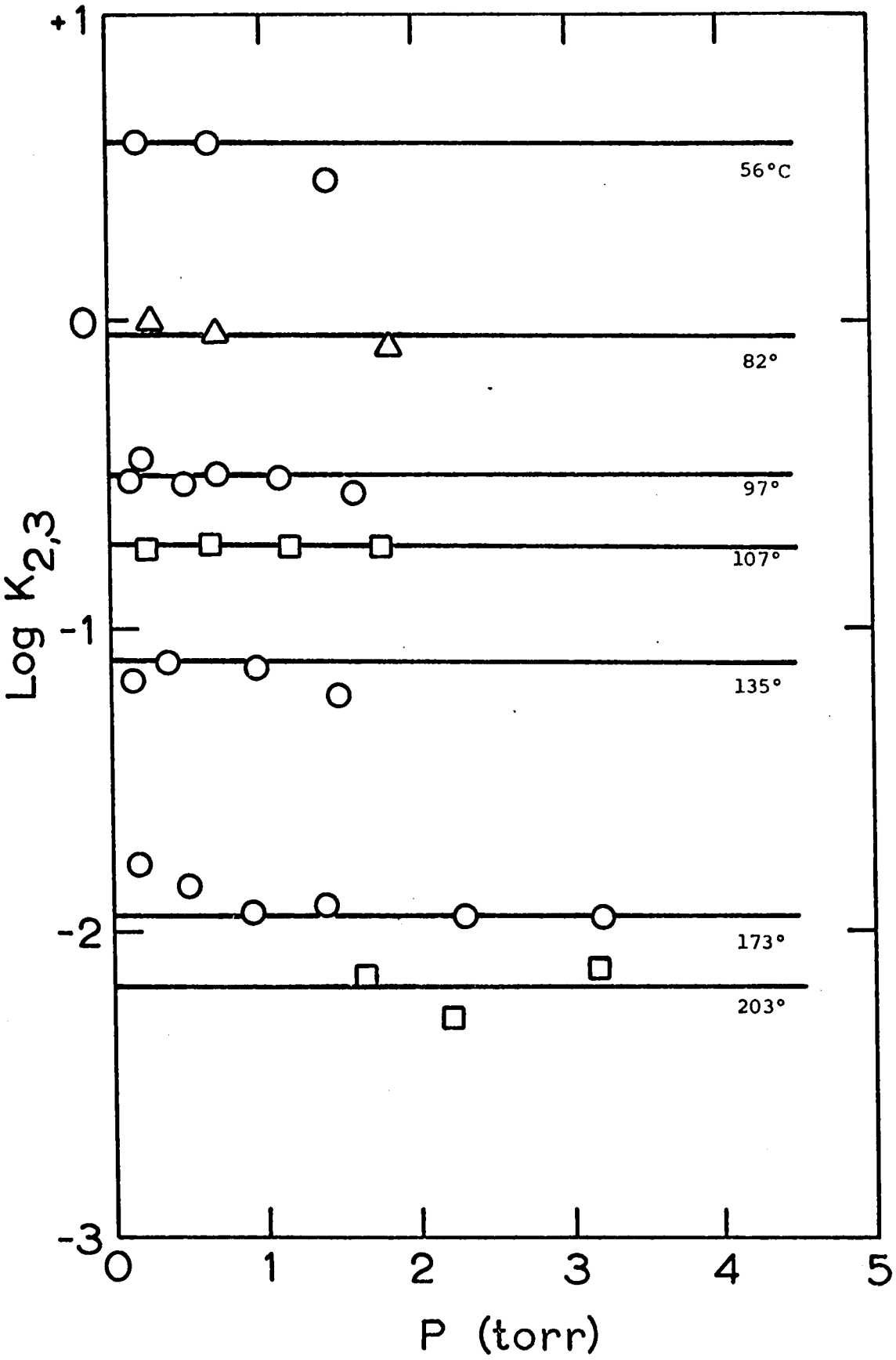

Figure 6.4 Plots of log $K_{2,3}$ versus pressure at various temperatures. O, 5 μ x 4 mm; □, 15 μ x 1.7 mm; △, 1.5 μ x 3.5 mm ion exit slit dimensions.

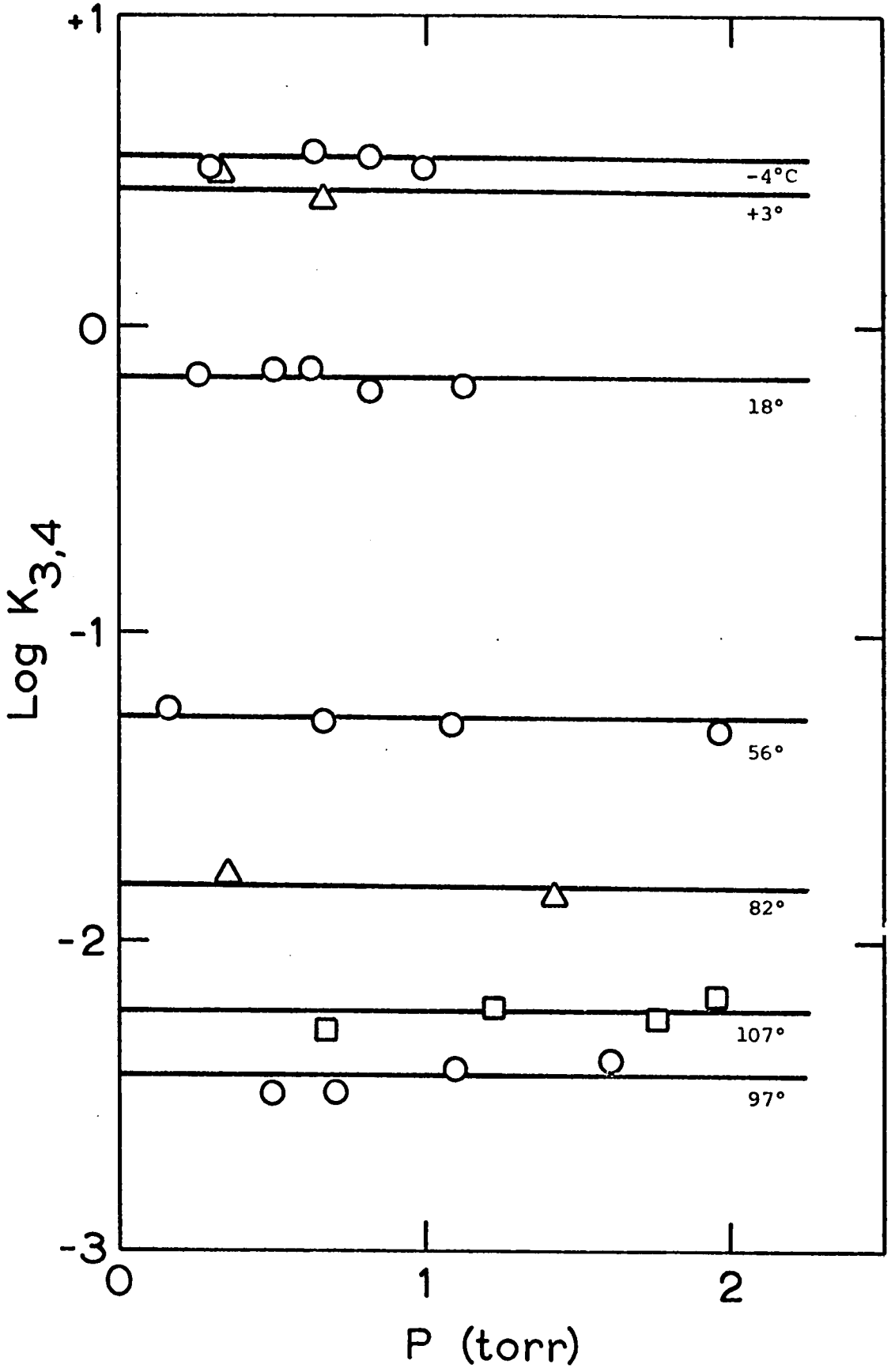

Figure 6.5 Plots of Log $K_{3,4}$ versus pressure at various temperatures. O, 5 μ x 4 mm; □, 15 μ x 1.7 mm; △, 1.5 μ x 3.5 mm ion exit slit dimensions.

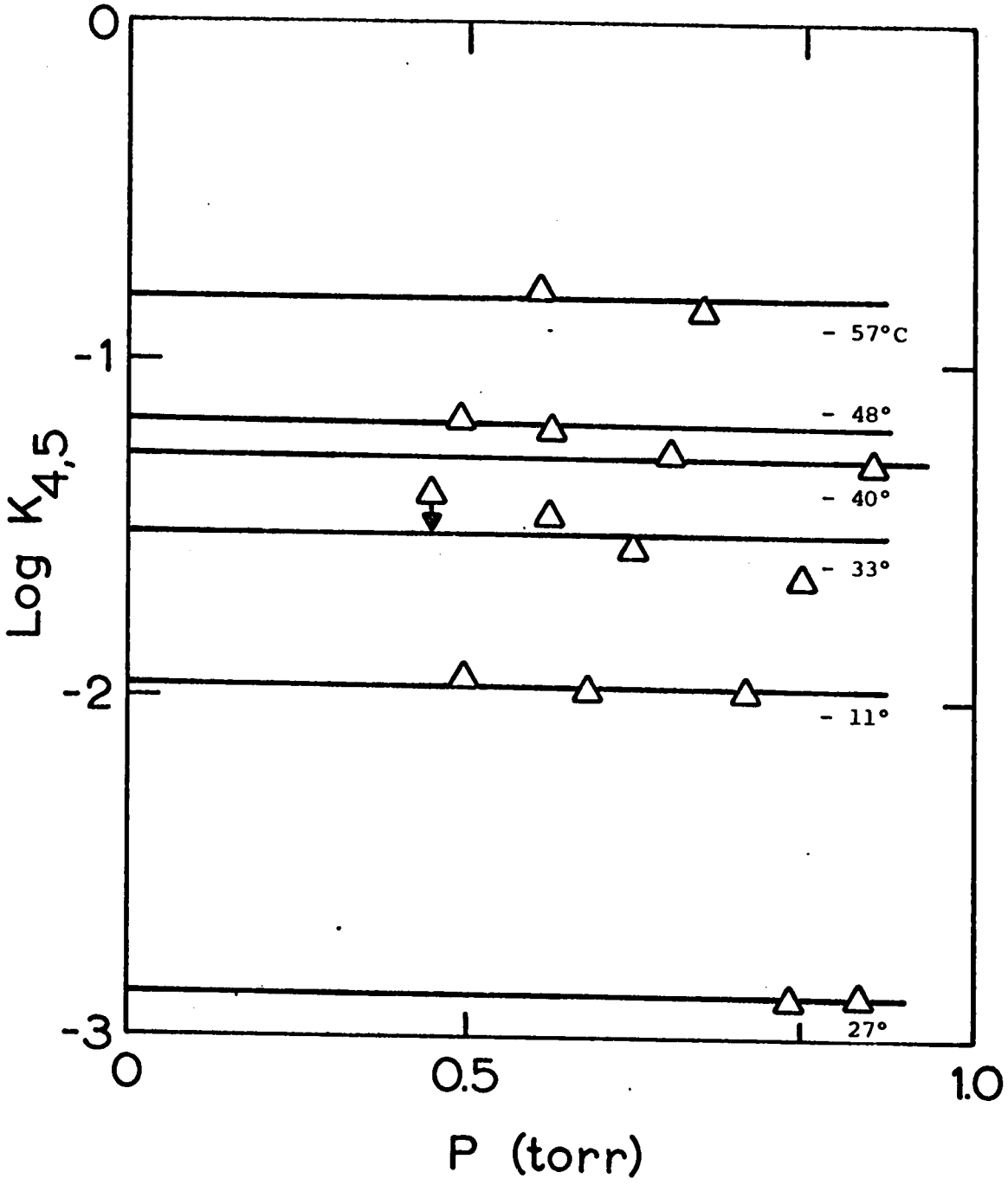

Figure 6.6 Plots of log $K_{4,5}$ versus pressure at various temperatures. △, 1.5 μ x 3.5 mm ion exit slit dimensions.

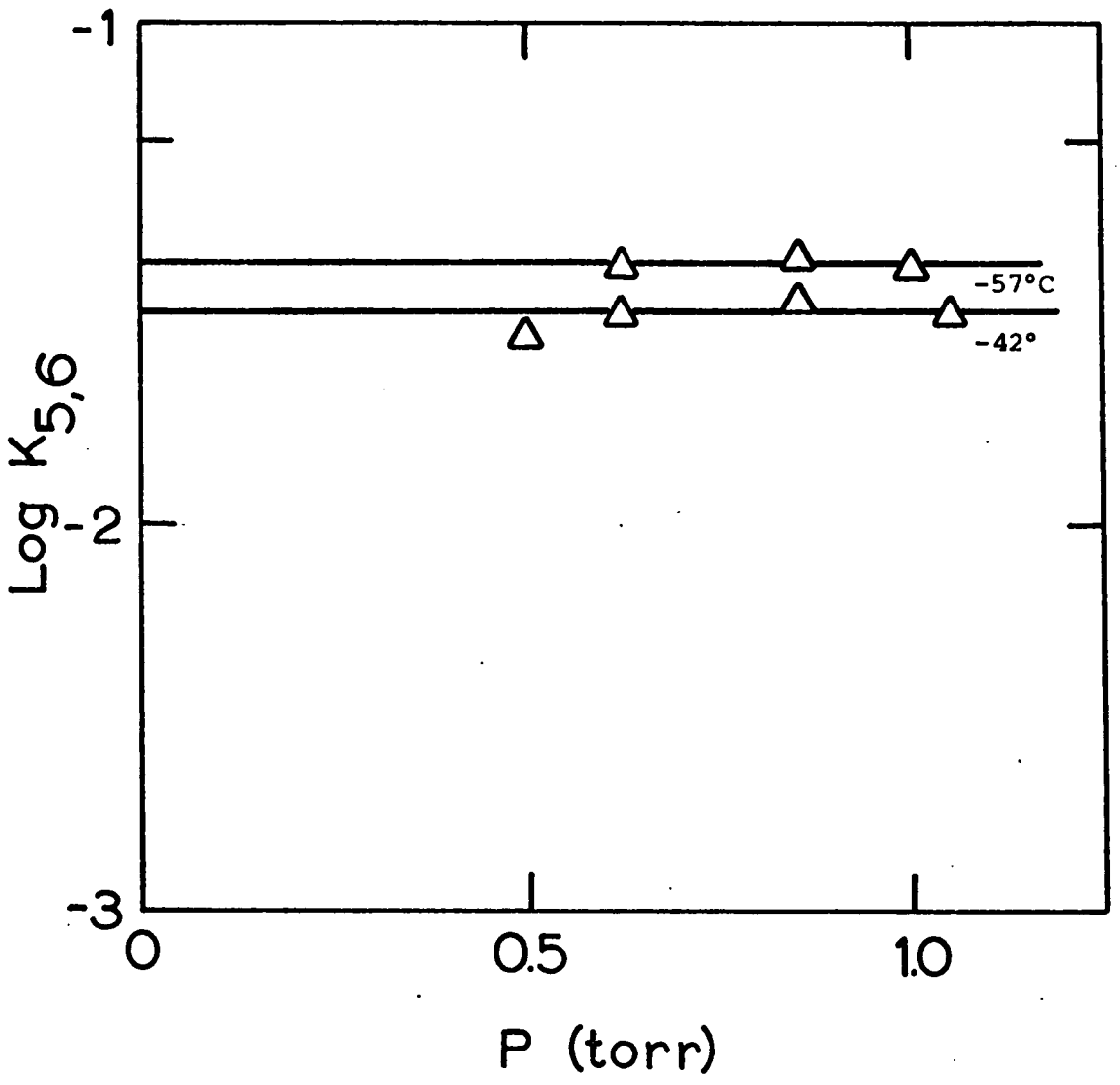

Figure 6.7 Plots of log $K_{5,6}$ versus pressure at various temperatures. △, 1.5 μ x 3.5 mm ion exit slit dimensions.

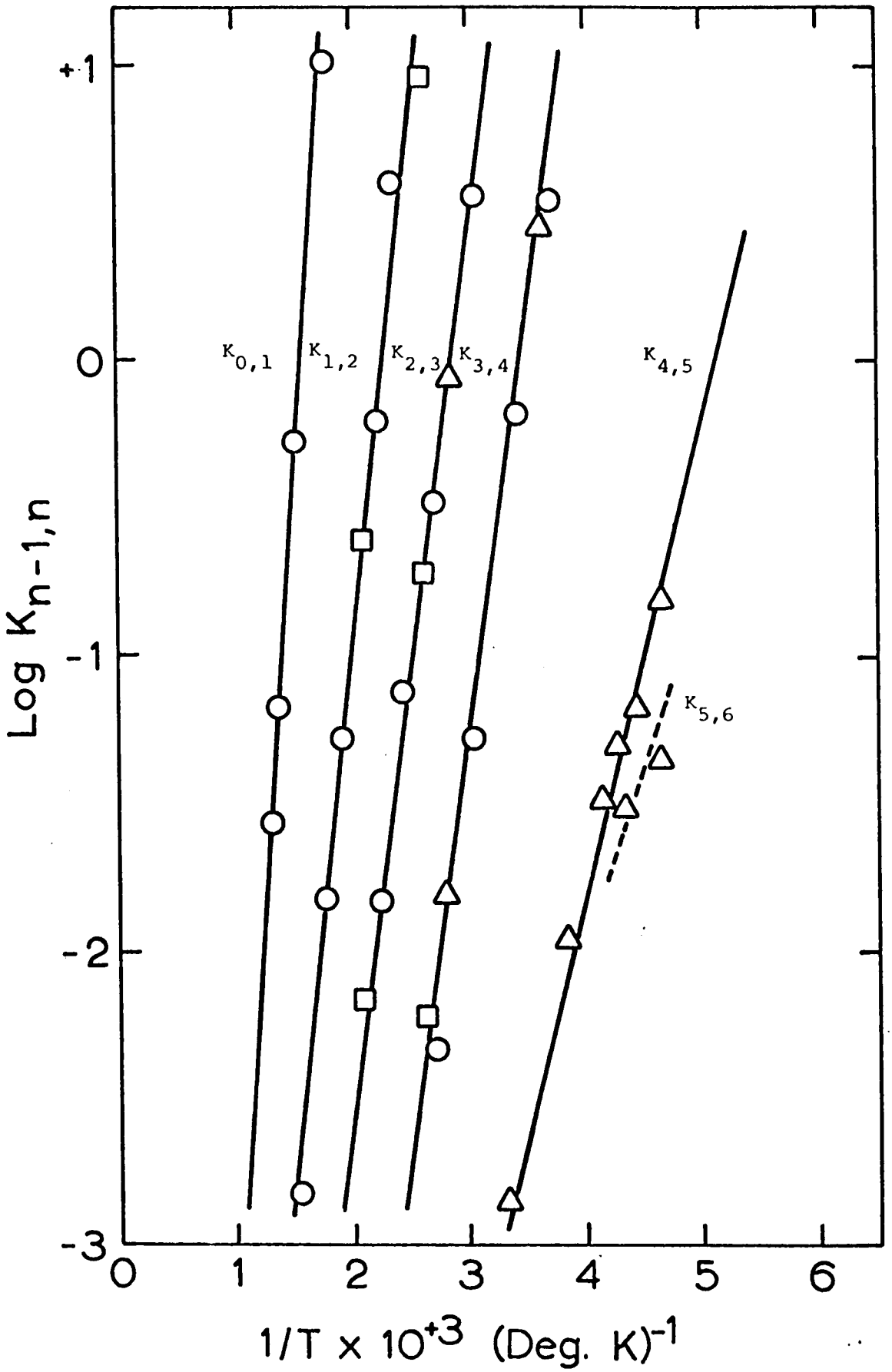

Figure 6.8 Van't Hoff-type plots of the equilibrium constants. O, 5 μ x 4 mm; □, 15 μ x 1.7 mm; △, 1.5 μ x 1.7 mm ion exit slit dimensions.

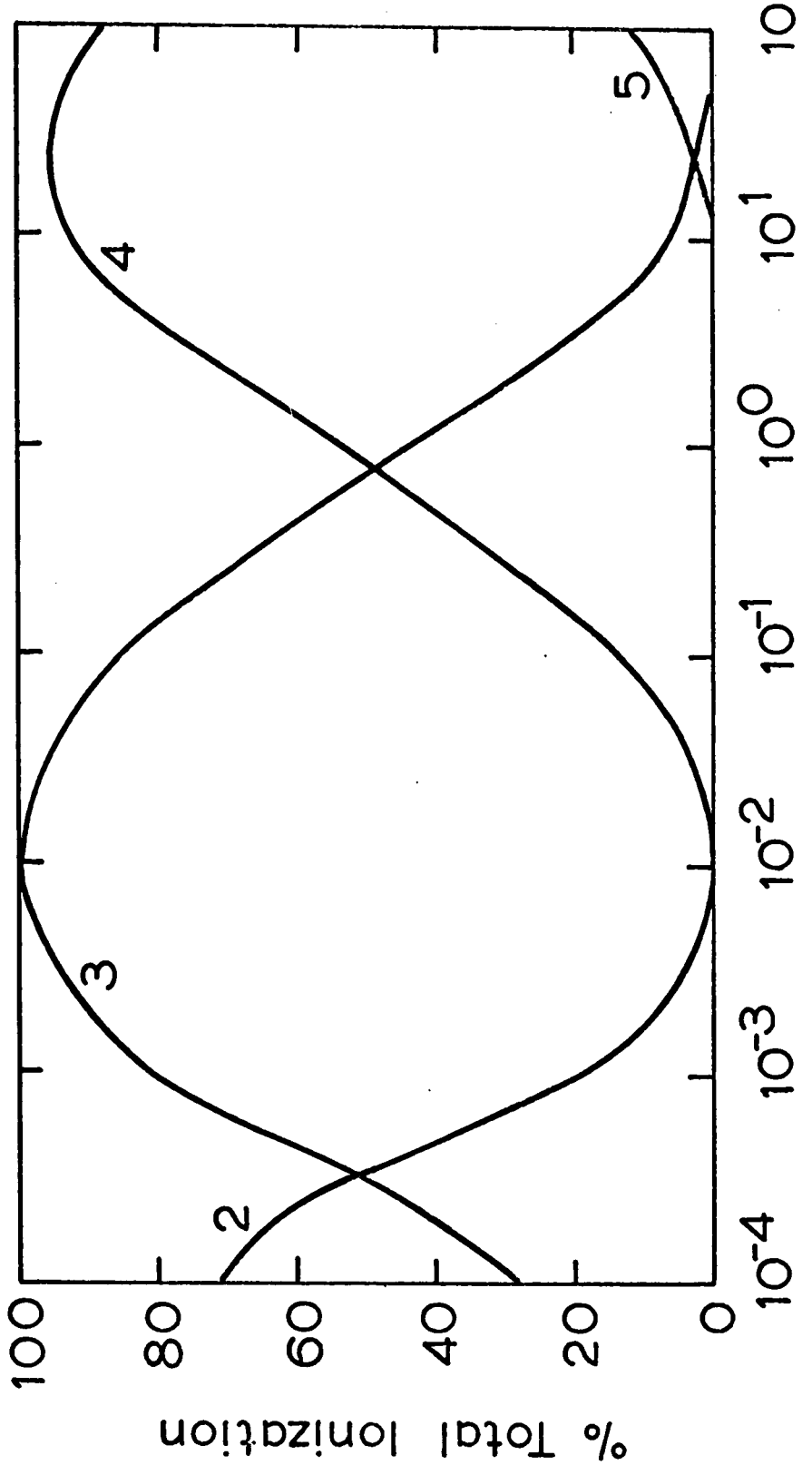

Figure 6.9 Calculated equilibrium distributions of clusters $NH_4^+(NH_3)_n$ from experimental data for 300°K.

TABLE 6.1

Representative Data Given as the Mass Spectra in Per Cent Total Ionization

No.	Temp.* C° a	b	P. torr	Mass Spectrum of $NH_4^+(NH_3)_n$ n=0	1	2	3	4	5	Total Ion Current A x 10^{14}
1	-2	-5	0.30			1.1	50	49		1
			0.63			0.8	30	69		3
			0.79			1.3	26	73	0.21	4
	-2	-6	0.98			1.6	24	74	0.45	4
			1.22			2.0	27	70	0.60	3
	-2	-6	1.85			2.3	27	70	1.0	1
2	93	105	0.20		24	71	4.4			1
			0.40		8.1	81	11			4
			1.00		4.4	74	21	0.07		10
			1.41		.7	68	31	0.14		10
			2.22		1.0	59	40	0.34		9
	88	100	3.21		2.1	52	45	0.61		5
3	379	391	0.20	95	5.0					0.3
			0.67	74	26	0.027				2
			1.31	59	41	0.076				10
	379	391	2.23	46	54	0.16				40
			3.04	40	60	0.27				100
	381	398	4.36	36	64	0.30				100

*a is the temperature of the thermocouple in the bottom of the ion source while b is the temperature of the thermocouple in the ion source top.

TABLE 6.2

Experimental Thermodynamic Values for the Gas Phase Reactions:

$$NH_4^+(NH_3)_{n-1} + NH_3 \rightleftharpoons NH_4^+(NH_3)_n \quad (n-1,n)$$

at 298°K and 1 atm.

n-1,n	$-\Delta H^\circ_{n-1,n}$ (kcal/mole)		$-\Delta G^\circ_{n-1,n}$ (kcal/mole)		$-\Delta S^\circ_{n-1,n}$ (e.u.)	
	Present work	Ref. 15	Present work	Ref. 15	Present work.	Ref. 15
0,1	27		17.5		32	
1,2	17		9.0		27	
2,3	14.0	17.8	6.1	6.4	27	38
3,4	13.1	15.9	3.6	3.8	32	40
4,5	7.5	(9)[b]	0.2	0.5	25	(33)[a]

a Estimated.

b Obtained from $\Delta G^\circ_{4,5}$ and the estimated $\Delta S^\circ_{4,5}$.

TABLE 6.3

Constants for the Determination of $K_{n-1,n}$

Standard state 1 torr.

Reaction n-1,n	A	B
0,1	5.87	9.84
1,2	3.69	8.75
2,3	3.05	8.75
3,4	2.85	9.84
4,5	1.63	8.31

expected to be similar to the corresponding reaction in the $H^+(H_2O)_n$ system, reaction 5.3. The values for respective experimental entropy changes are, in fact, very close, -32 and - 33 e.u. This agreement plus the theoretical calculation of the entropy change for reaction 5.3 suggests the experimental entropy value for $\Delta S°_{0,1}$ for reaction 6.4 is approximately correct.

C. Comparison of Results to Other Ammonia Condensation Reactions

The values for the thermodynamic functions of reaction 4,5 are compared to the values for reactions 6.6 and 6.7 in

6.6 $$NH_{3(g)} + NH_{3(g)} \longrightarrow (NH_3)_{2(g)}$$

6.7 $$NH_{3(g)} \xrightarrow{NH_{3(\ell)}} NH_{3(\ell)}$$

Table 6.4. The magnitude of the entropy changes are seen to be similar for all three reactions. Because of the low heat of condensation of ammonia, the forces in the 6^{th} cluster are predominantly ion-molecule rather than molecule-molecule forces.

D. The Structure of the Solvated Ions

As discussed in the previous chapter, there is a choice between two models for the structure of the solvated ions. In the first model a central ion, either NH_4^+ or H^+, is surrounded

TABLE 6.4

Comparison of Values for the Thermodynamic Functions of Condensation Type Reactions at 298°K

Reaction	ΔH° (kcal/mole)	ΔG° (kcal/mole)	ΔS° (e.u.)
4,5	-7.5	-0.2	-25
6.6[a]	-4.4	+3.5	-26.8
6.7[b]	-4.75	+2.17	-23.2

a. Ref. (59).

b. Ref. (61).

by NH_3 molecules. If the central ion is NH_4^+, one might expect a break in the thermodynamic functions upon addition of the fifth ammonia molecule. The reason is that only four ligands can be coordinated with the hydrogen atoms of NH_4^+. Consequently, the addition of the fifth ammonia molecule requires either the beginning of an outer shell of ammonia molecules or a rearrangement of the complex, possibly to $H^+(NH_3)_5$. As can be seen from Table 6.2, the values for all three thermodynamic functions take a sharp drop in absolute magnitude between reactions 3,4 and 4,5. This supports the idea that the central ion of the complex for n=1 to 4 is NH_4^+. An analysis of the relative potential energies of $H^+(NH_3)_5$ and $NH_4^+(NH_3)_4(NH_3)$ would be required to determine the central ion.

We may now consider why the ammonia system has the central ion NH_4^+ while the water system (section 5.3 D), apparently has either the central ion H^+ or an ion H^+ which is free to move about in the cluster. The central ion H^+ possibility for the ammonia cluster cannot be ruled out on theoretical grounds without a detailed study. However, the mobile H^+ possibility is less likely in the ammonia system than in the water system since the phenomenon of the anomalously high mobility of H^+ which occurs in liquid water has been found absent in liquid ammonia in an investigation by Gill (65).

7. CONCLUSIONS FROM THE GAS PHASE SOLVATION RESULTS

7.1 Introduction

The reason for performing this work was to obtain information on gas phase solvation reactions. It was hoped that the gas phase solvation results would be useful to researchers studying solvation phenomena in the liquid phase. The advantage of the present work over liquid phase work was that the empirical formula and relative concentration of each solvated species could be determined directly by mass analysis.

7.2 Structure of the Solvated Ions

The observation of solvated species in the present work proved the existence and stability of certain ionic clusters. From the smooth change in the thermodynamic values for $\Delta H°_{n-1,n}$, $\Delta G°_{n-1,n}$, and $\Delta S°_{n-1,n}$ for the reaction 7.1, it was concluded

$$7.1 \qquad H^+(H_2O)_{n-1} + H_2O \rightleftarrows H^+(H_2O)_n$$

in section 5.3 D that notation $H^+(H_2O)_n$ better represents the ionic clusters than $H_3O^+(H_2O)_{n-1}$. The basis for this conclusion is the assumption that if the cluster had a central ion H_3O^+, a break would occur in the thermodynamic values between reactions 3,4 and 4,5.

Similarly, a central ion NH_4^+ would be indicated for the cluster $NH_4^+(NH_3)_n$ if a break occurred in the thermodynamic

values between the specific reactions 3,4 and 4,5 of the general reaction 7.2. In Chapter 6 a definite break was found at this point.

$$7.2 \qquad NH_4^+(NH_3)_{n-1} + NH_3 \rightleftharpoons NH_4^+(NH_3)_n$$

The question of the identity of the central ion does not arise in the hydration of the potassium ion. Consequently it might be expected that the plots for the thermodynamic values for reaction 7.3 as a function of n-1,n would be completely structureless. However,

$$7.3 \qquad K^+(H_2O)_{n-1} + H_2O \rightleftharpoons K^+(H_2O)_n$$

as seen in Figure 4.20 this is not the case. As indicated in section 4.4 the "bump" in the $\Delta H°_{n-1,n}$ plot versus n-1,n may be due to the non-uniform changes in the ligand-ligand distances with increasing cluster size. This affects the changes in the dipole-dipole repulsion energies which are primarily responsible for the change of $\Delta H°_{n-1,n}$ with n-1,n.

We may now consider why the plots of the thermodynamic values for reaction 7.3 show some structure while the thermodynamic values for reaction 7.1 produce a smooth curve. The relative lack of structure for the thermodynamic values for reaction 7.1 is an indication that the proton and its surrounding water molecules are not held in fixed positions while K^+ is most probably fixed. Instead the charge in $H^+(H_2O)_n$ can move about the cluster by proton transfer.

A second means of determining the structure of the ions is from a plot of the weighted average number of ligands

per ion as a function of pressure. Such plots are illustrated in Figure 7.1A and 7.1B. For $K^+(H_2O)_n$ and $H^+(H_2O)_n$ no single ionic species appears to exhibit dominant stability in the pressure range considered. However, the plot of $NH_4^+(NH_3)_n$ indicates a high relative stability of $NH_4^+(NH_3)_4$ over the pressure range 10^{-3} to 10^{-1} torr.

One conclusion from the above considerations is that if a single structure such as $H_9O_4^+$ as proposed by Eigen and de Maeyer (66) has special stability in liquid water, the special stability is created by the effect of the bulk solvent on the ionic cluster.

7.3 Effect of the Liquid Phase on the Ionic Clusters

A. Ligand Bond Energies in the Liquid Phase

One way in which the present $\Delta H°_{n-1,n}$ values can be related to the condensed phase is through the theoretical arguments of Bernal and Fowler (67). They have proposed the following relating to the ionic solvation in liquid water. The hydration of an ion will occur when the potential energy of a water molecule coordinated to an ion is less than that of a free water molecule. The free molecule has four neighbors while the ion-bonded molecule has three, an ion and two water molecules. The condition for an ion having at least one coordinated water is, therefore, that the potential energy $\Delta E°_{n(\ell)}$ for a water molecule due to coordination to

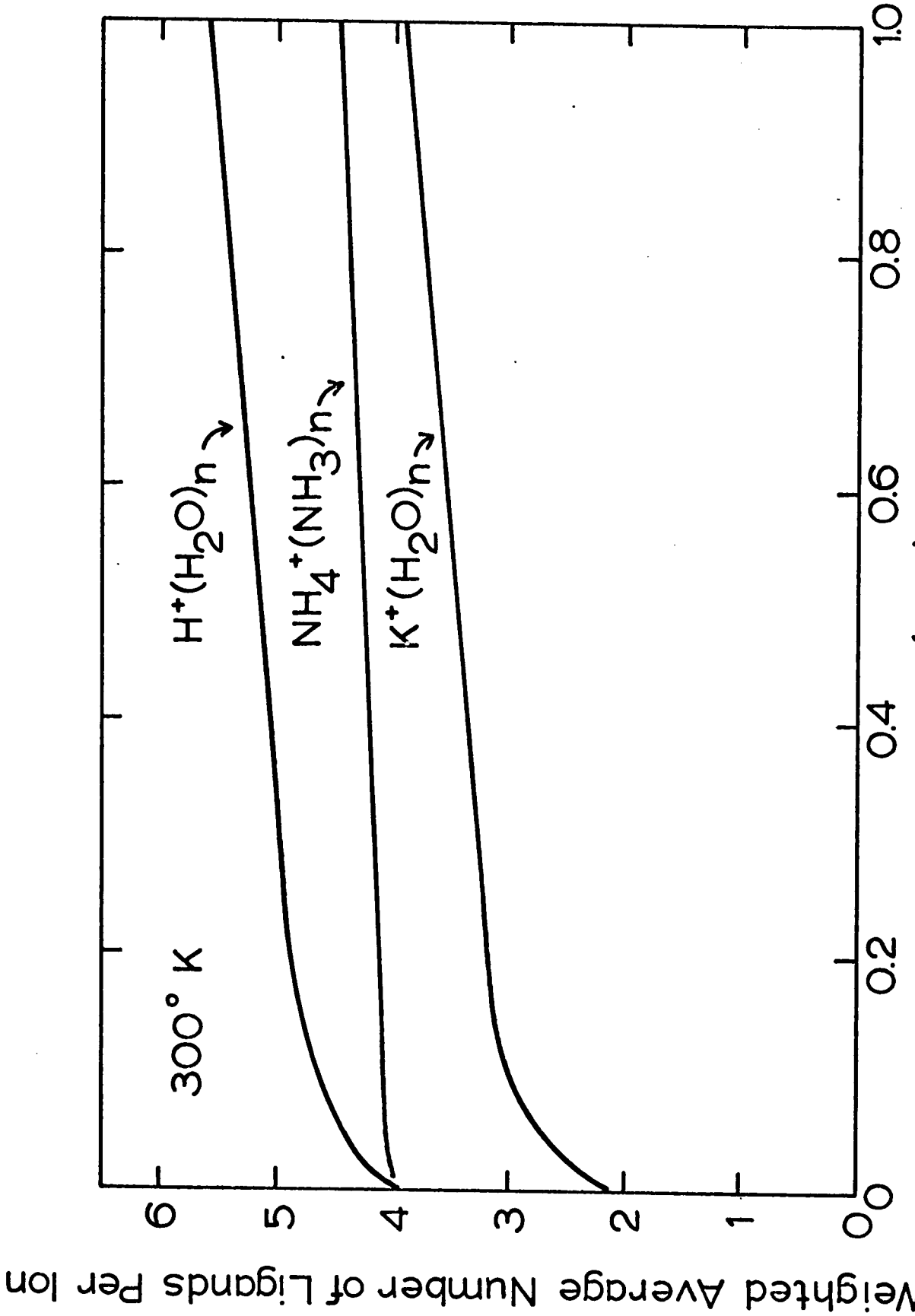

Figure 7.1A Plot of the weighted average number of ligands per ion versus pressure.

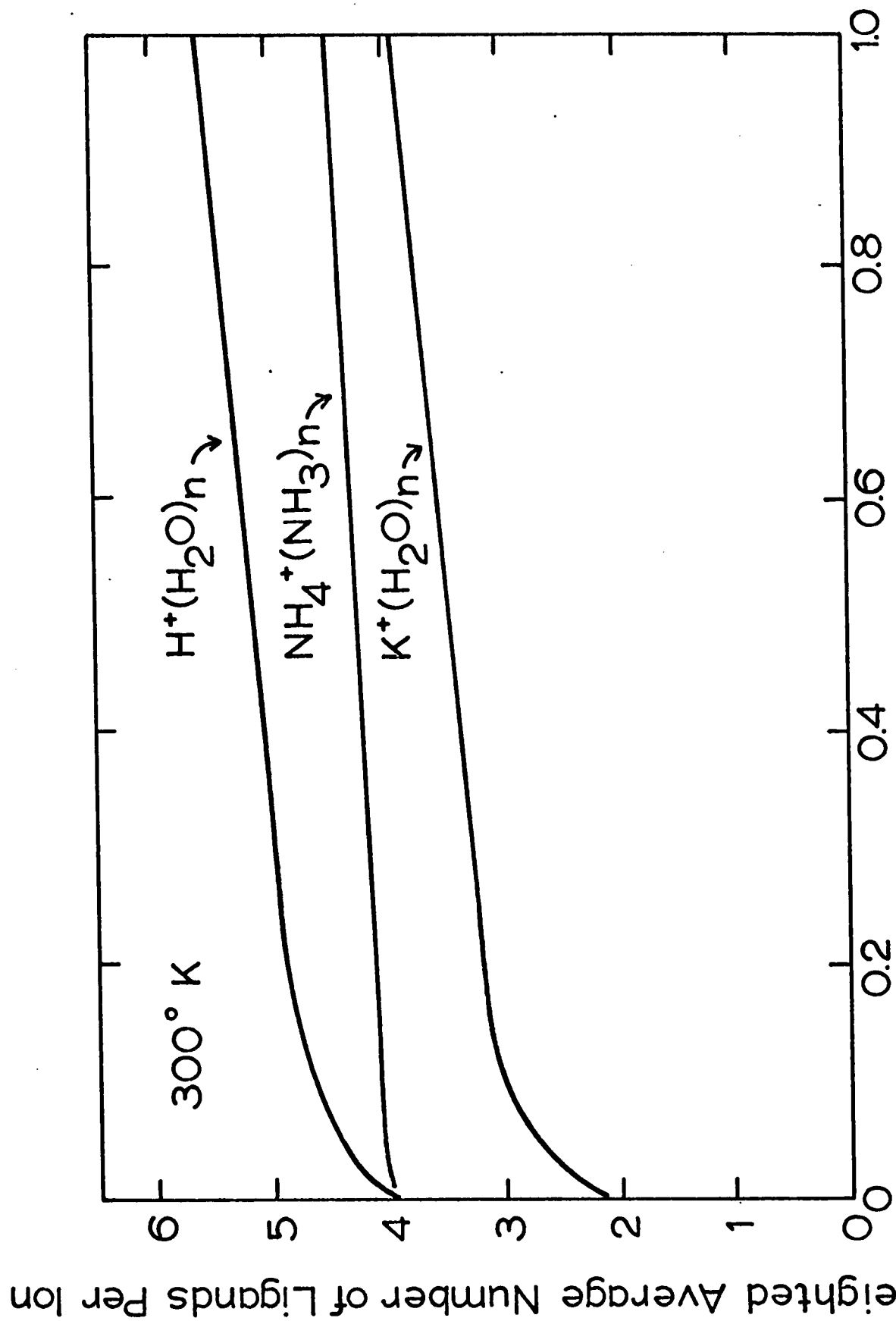

Figure 7.1A Plot of the weighted average number of ligands per ion versus pressure.

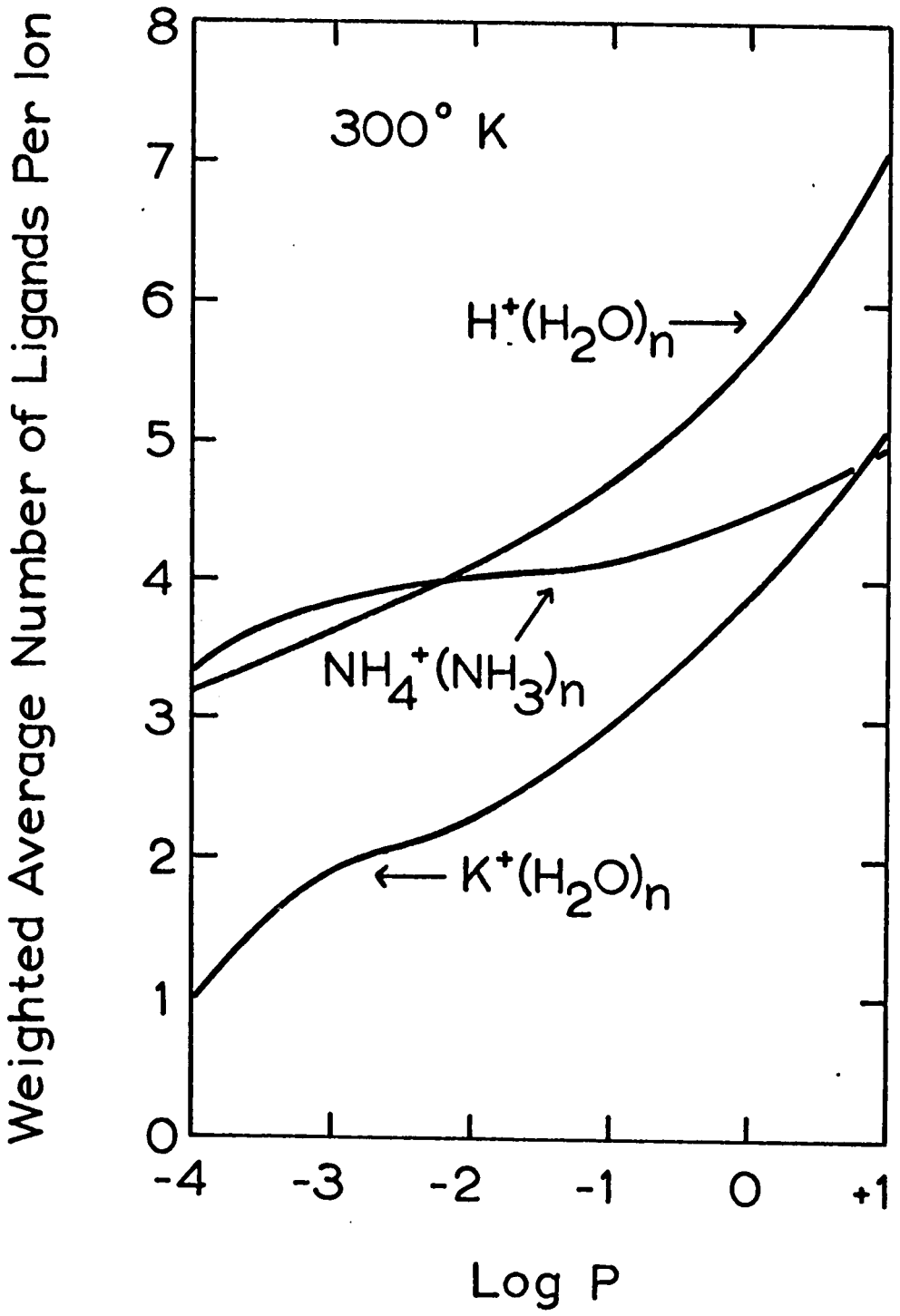

Figure 7.1B Plot of weighted average number of ligands per ion versus log pressure. The log scale is used to cover a wide pressure range.

an ion be less than the potential energy 2 $P.E._{H.B.}$ for a water molecule due to coordination to two water molecules. 2 $P.E._{H.B.}$ is calculated by Bernal and Fowler to be -15 kcal/mole. This fact gives rise to equation 7.1 for the ion-water molecule bond energy B.E.

$$7.1 \qquad B.E. = \Delta E°_{n(\ell)} + 15$$

$\Delta E°_{n(\ell)}$ can be set equal to $\Delta E°_{n(g)}$, the potential energy for a water molecule due to coordination to an ion in the gas phase. This is not unreasonable since Bernal and Fowler appear to have taken the dielectric constant as unity in their calculation of $P.E._{H.B.}$

Since in section 4.4 it was found that $\Delta H°_{n-1,n} \approx \Delta E°_{n(g)}$, $\Delta H°_{n-1,n} \approx \Delta E°_{n(\ell)}$. Equation 7.1 can be rewritten as equation 7.2.

$$7.2 \qquad B.E. = \Delta H°_{n-1,n} + 15$$

The bond energies calculated for $K^+(H_2O)_n — H_2O$ and $H^+(H_2O)_n — H_2O$ with the $\Delta H°_{n-1,n}$ values from Table 4.2 and 5.2 respectively are listed in Table 7.1. The bond energies for $K^+(H_2O)_n — H_2O$ show that the potassium ion in solution may have one or two coordinated water molecules.

However, the potassium ion is considered to be unhydrated in solution (55,68). The discrepancy may well be due to approximations in the theoretical calculations. Nevertheless, the present results suggest rather weak bonds for the liquid

TABLE 7.1

Ion-Water Molecule Bond Energies in the Liquid Phase

Bond	Bond Energy (kcal/mole)
$K^+ — H_2O$	- 2.9
$K^+(H_2O) — H_2O$	- 1.1
$K^+(H_2O)_2 — H_2O$	+ 1.8
$H^+(H_2O) — H_2O$	- 11
$H^+(H_2O)_2 — H_2O$	- 7
$H^+(H_2O)_3 — H_2O$	- 2
$H^+(H_2O)_4 — H_2O$	0
$H^+(H_2O)_5 — H_2O$	+ 2

phase coordination of a water molecule to the potassium ion.

The bond energies for $H^+(H_2O)_n$ — H_2O indicate that the largest expected ionic cluster in liquid water is $H^+(H_2O)_5$. Because of the relatively strong bond energy of the second molecule and the zero bond energy for the fifth molecule, the dominant ion in solution could be $H^+(H_2O)_3$ or $H^+(H_2O)_4$.

B. Comparison of Experimental Gas Phase Free Energy Values with the Free Energy of Hydration

The free energy of hydration of an ion, $\Delta G°_{hyd}$, is defined as the free energy change occurring in reaction 7.4 a or 7.4 b.

7.4 a $$M^+_{(g)} + \infty\ H_2O_{(\ell)} \longrightarrow M^+_{(aq.)} + \infty\ H_2O_{(\ell)}$$

7.4 b $$X^-_{(g)} + \infty\ H_2O_{(\ell)} \longrightarrow X^-_{(aq.)} + \infty\ H_2O_{(\ell)}$$

The determination of $\Delta G°_{hyd}$ has been the subject of a number of papers. The present gas phase free energies of hydration $\Delta G°_{n-1,n}$ can be directly compared with $\Delta G°_{hyd}$. In a recent paper, Kebarle, Arshadi, and Scarborough (21) have compared the values of $\Delta G°_{3,4}$ (measured in this laboratory) to $\Delta G°_{hyd}$ for the ions, Na^+, K^+, F^-, Cl^-, Br^-, and I^-. Although this discussion is mostly a review of the Kebarle *et.al.* paper, the present approach is somewhat different.

If one assumes that both $\Delta G°_{3,4}$ and $\Delta G°_{hyd}$ have the same dependence on the ionic radius, the relative values of $\Delta G°_{3,4}$ and the relative values of $\Delta G°_{hyd}$ should be similar.

On this basis a comparison between relative free energy values is given in Table 7.2. The values for $\Delta G°_{hyd}$ in column B resulted from Volta potential difference measurements between phases separated by gas (69). The values in columns C to E result from the Born equation (70), equation 7.3 in which N is Avogadro's number, ze is the ionic charge, r is the ionic radius and D is the dielectric constant.

$$7.3 \qquad -\Delta G°_{hyd} = \frac{Nz^2e^2}{2r}\left(1 - \frac{1}{D}\right)$$

The experimental radii of Gourary and Adrian (71) result in the best theoretical agreement with the gas phase free energies. The values of Randles (69) are in good agreement with both those values from Gourary and Adrian's radii and the gas phase free energies.

7.4 A Suggestion for Further Research

Because the gas phase solvation reactions are relevant to liquid phase solvation, radiation chemistry (6), and upper atmospheric equilibria (4), it is proposed that further work be carried out in this area. One interesting project would be the study of the effect of the ionic charge on solvation. Two reactions which might be studied are 7.5 and 7.6. The reason

$$7.5 \qquad Hg^{+}(H_2O)_{n-1} + H_2O \rightleftharpoons Hg^{+}(H_2O)_n$$

$$7.6 \qquad Hg^{+2}(H_2O)_{n-1} + H_2O \rightleftharpoons Hg^{+2}(H_2O)_n$$

TABLE 7.2

Relative Free Energies of Hydration

Ion	$\Delta G^\circ_{3,4}/\Delta G^\circ_{3,4}(K^+)$	$\Delta G^\circ_{hyd}/\Delta G^\circ_{hyd}(K^+)$			
	A	B	C	D	E
Na^+	1.30	1.22	1.22	1.27	1.41
K^+	1.00	1.00	1.00	1.00	1.00
F^-	1.38	1.23	1.55	1.28	0.98
Cl^-	0.91	0.88	1.14	0.91	0.74
Br^-	0.74	0.81	1.06	0.83	0.65
I^-	0.51	0.71	0.95	0.73	0.59

A. From data compiled in Reference (21).

B. From Reference (69) experimental.

C,D,E. From Born equation with radii from References (72,71,45) respectively.

for proposing mercury ion solvation is that both Hg^{+} and Hg^{+2} can be created by ionization of Hg vapor by the 100 kev proton beam which is available in this laboratory. One difficulty in this study is that reaction 7.7 may interfere with reaction 7.6.

7.7 $$Hg^{+2} + H_2O \rightarrow Hg^{+} + H_2O^{+}$$

$$\Delta H = -6.09 \text{ e.v.} \quad (51)$$

BIBLIOGRAPHY

1. C.E. Melton in F.W. McLafferty (ed.) Mass Spectrometry of Organic Ions, Academic Press, New York (1963), Chapter 2.

2. R.J. Munson and A.M. Tyndall, Proc. Roy. Soc. A172, 28 (1939).

3. L.B. Loeb, Basic Processes of Gaseous Electronics, University of California Press, Los Angeles (1961), Chapter 1.

4. R.S. Narcisi and A.D. Bailey, J. Geophys. Res. 70, 3687 (1965).

5. S.C. Lind, Radiation Chemistry of Gases, Reinhold Publishing Corp., New York (1961), p. 8.

6. a A.R. Anderson, B. Knight and J. Winter, Nature 209, 199 (1966).

b A.R. Anderson, B. Knight and J. Winter, Trans. Faraday Soc. 62, 359 (1966).

7. K. Bansal and G.R. Freeman, private communication.

8. P.H. Dawson and A.W. Tickner, J. Chem. Phys. 40, 3745 (1964).

9. P.F. Knewstubb and A.W. Tickner, J. Chem. Phys. 38, 464 (1963).

10, a J. Yang and D.C. Conway, J. Chem. Phys. 40, 1729 (1964.)

b D.C. Conway and J. Yang, J. Chem. Phys. 43, 2900 (1965).

11. L.W. Sieck, F.P. Abramson and J.H. Futrell, J. Chem. Phys. 45, 2859 (1966)

12. M.S.B. Munson, J. Amer. Chem. Soc. 87, 5313 (1965).

13. M.S.B. Munson, J. Phys. Chem. 70, 2034 (1966).

14. H.D. Beckey, Z, Naturforsch. 15a, 822 (1960).

15. A.M. Hogg, R.M. Haynes and P. Kebarle, J. Amer. Chem. Soc. 88, 28 (1966).

16. S.K. Searles and P. Kebarle, J. Phys. Chem. 72, 742 (1968).

17. A.M. Hogg and P. Kebarle, J. Chem. Phys. 43, 449 (1965).

18. P. Kebarle, R.M. Haynes and J.G. Collins, J. Amer. Chem. Soc. 89, 5753 (1967).

19. P. Kebarle and A.M. Hogg, J. Chem. Phys. 42, 798 (1965).

20. P. Kebarle, S.K. Searles, A. Zolla, J. Scarborough and M. Arshadi, J. Amer. Chem. Soc. 89, 6393 (1967).

21. a P. Kebarle, M. Arshadi and J. Scarborough, J. Chem. Phys. (to be published July, 1968).

b P. Kebarle, M. Arshadi and J. Scarborough, J. Chem. Phys. (submitted for publication).

22. J.G. Collins, Ph.D. Thesis, University of Alberta (1967).

23. C.A. McDowell (ed.) Mass Spectrometry, McGraw-Hill Book Co. Inc., New York (1963).

24. W.J. Moore, Physical Chemistry, Prentice-Hall, Inc., Englewood Cliffs, New Jersey (1962), p. 343.

25. E.W. McDaniel, Collision Phenomena in Ionized Gases, John Wiley & Sons, Inc., New York (1964), p. 490.

26. S. Glasstone, Textbook of Physical Chemistry, D. Van Nostrand Co. Inc., New York (1946), p. 276.

27. Reference (24), p. 229.

28. F.J. Garrick, Phil. Mag. 9, 131 (1930); 10, 76 (1930).

29. "Consolidated Vacuum Corp., Bulletin 4-3," Consolidated Vacuum Corp., Rochester, New York.

30. A. Guthrie, Vacuum Technology, John Wiley and Sons, Inc., New York (1963), Chapter 2.

31. J.T. Park, Ph.D. Thesis, University of Nebraska, (1963).

32. a J.T. Prud'homme, Texas Nuclear Corp., Neutron Generators, Texas Nuclear Corp., Austin, Texas (1962).

b Instruction Manual Model 150-1H Neutron Generator, Texas Nuclear Corp., Austin, Texas.

33. For example, V.L. Tal'roze and E.L. Frankevich, Russ. J. Phys. Chem. (Eng. trans.) 34, 1275 (1960); A.G. Harrison and J.C.J. Thynne, Trans. Faraday Soc. 62, 2804 (1966); and K.R. Ryan and J.H. Futrell, J. Chem. Phys. 43, 3009 (1965).

34. D. Durden, T. Good and P. Kebarle, J. Chem. Phys. (submitted for publication).

35. Reference (24), p. 427.

36. G.R. Freeman, "Radiation Chemistry Lecture Notes," University of Alberta, p. 78.

37. R.O. Jenkins and W.G. Trodden, Electron and Ion Emission from Solids, Routledge and Kegan Paul Ltd., London (1965), Chapter 7.

38. Reference (24), p. 225.

39. Reference (30), p. 509.

40. R.W. Kiser, Introduction to Mass Spectrometry, Prentice-Hall, Inc., Englewood Cliffs, New Jersey (1965), p. 57.

41. D.V. Pilipenko and Ya. M. Fogel, J. Exp. Theo. Phys. (Eng. trans.) 21, 266 (1965).

42. G.B. Lopantseva and O.B. Firsov, J. Exp. Theo. Phys. (Eng. trans.) 23, 648 (1966).

43. G.H. Wannier, Phys. Rev. 83, 281 (1951).

44. R.J. Munson, A.M. Tyndall and K. Hoselitz, Proc. Roy. Soc. A172, 28 (1939).

45. Handbook of Chemistry and Physics, 41st Ed., Chemical Rubber Publ. Co., Cleveland (1959), p. 3389.

46. P. Kebarle, R.M. Haynes and S.K. Searles, Adv. Chem. Ser. 58, 210 (1966).

47. Reference (26), Chapter 11.

48. N. Davidson, Statistical Mechanics, McGraw-Hill Book Co. Inc., New York (1962), Chapter 11.

49. G.M. Barrow, Introduction to Molecular Spectroscopy, McGraw-Hill Book Co. Inc., New York (1962), Chapter 2.

50. W.A. Chupka, J. Chem. Phys. 30, 458 (1959).

51. V.I. Vedeneyev, L.V. Gurvich, V.N. Kondrat'yev, V.A. Medvedev and Ye. L. Frankevich, (Trans. by Scripta Technica Ltd.,), Bond Energies, Ionization Potentials, and Electron Affinities, Edward Arnold Ltd., London (1966).

52. G.J. Doyne and R.G. Caldwell, Report AD 635 522, Standford Research Institute (1966).

53. American Chemical Society, Adv. Chem. Ser. 15, 9 (1955).

54. J.S. Muirhead-Gould and K.J. Laidler, Trans. Faraday Soc. 63, 944 (1967).

55. G. Sposito and K.L. Babcock, J. Chem. Phys. 47, 153 (1967).

56. Reference (26), p. 300.

57. L.B. Magnusson, J. Chem. Phys. 39, 1953 (1963).

58. G.C. Pimentel and A.L. McClellan, The Hydrogen Bond, W.H. Freeman and Co., San Francisco (1960), p. 280.

59. Reference (58), p. 343.

60. J.C.J. Thynne and A.G. Harrison, Trans. Faraday Soc. 62, 2468 (1966).

61. F.D. Rossini, D.D. Wagman, W.H. Evans, S. Levine and I. Jaffe, Natl. Bur. Std. Circ. No. 500, (1952).

62. L. Dufour and R. Defay, Thermodynamics of Clouds, Academic Press, Inc., New York (1963), p. 86.

63. J.L.J. Rosenfeld, J. Chem. Phys. 40, 384 (1964).

64. A.G. Harrison and J.C.J. Thynne, Trans. Faraday Soc. 62, 2804 (1966).

65. J.B. Gill, Chem. Commun. 1965, 7 (1965).

66. M. Eigen and L. De Maeyer, Proc. Roy. Soc. 247A, 505 (1958).

67. J.D. Bernal and R.H. Fowler, J. Chem. Phys. 1, 515 (1933).

68. O. Ya. Samoilov (Trans. by D.J.G. Ives), Structure of Aqueous Electrolyte Solutions and the Hydration of Ions, Consultants Bureau, New York (1965), p. 106.

69. J.E.B. Randles, Trans. Faraday Soc. 52, 1573 (1956).

70. K.B. Harvey and G.B. Porter, Introduction to Physical Chemistry, Addison-Wesley Publ. Co. Inc., London (1963) p. 332.

71. B.S. Gourary and F.J. Adrian, Solid State Physics 10, 127 (1960).

72. W.M. Latimer, K.S. Pitzer and C.M. Slanski, J. Chem. Phys. 7, 108 (1935).

FORTRAN IV PROGRAM FOR CALCULATION OF POTENTIAL ENERGIES

```
C  ION-MOLECULE ELECTROSTATIC ENERGY I BY SKS
       REAL QI,POLI,Q(10),POL(10),R,RR,EE(20),EPOL(20),EDIP(20),
      1X(10,10),Y(10,10),Z(10,10),DX(10),DY(10),DZ(10),EDISP(20),IP(2),
      2EREP(20),E(10,20),DE(10,20),A(20),POLM,D,C,XX,YY,ZZ,BB,
      3RR1(9,10,10,10),R1(10,10),DIF,R12,R13,REP(20)
       INTEGER I,J,K,L,N,P,IN,M
       READ(5,1)QI,POLI,POLM,IP(1),IP(2),P,(Q(I),POL(I),I=1,P)
     1 FORMAT(F3.0,1X,4(F6.2,1X),I2/(F5.2,1X,F6.2))
       WRITE(6,18)QI,POLI,POLM,IP(1),IP(2),P,(Q(I),POL(I),I=1,P)
    18 FORMAT (1H1,10X,10HINPUT DATA/3H QI,2X,4HPOLI,4X,4HPOLM,3X,5HIP(1),
      11X,5HIP(2), 2X,1HP/1X,F3.0,1X,4(F6.2,1X),I2//5H Q(I),4X,6HPOL(I)/
      2(1X,F5.2,1X,F6.2))
    15 READ(5,4)N
     4 FORMAT(I2)
       IF(N.EQ.-1)STOP
       WRITE(6,20)N
    20 FORMAT(1H1,2X,1HX,8X,1HY,8X,1HZ,30X,4HN = ,I2)
       IN=1
       DO 22 J=1,N
       WRITE(6,32)J
    32 FORMAT(1HO,5X,13HMOLECULE NO. ,I2)
       DO 22 I=1,P
       READ(5,5) X(I,J),Y(I,J),Z(I,J)
     5 FORMAT(3(F7.3,2X))
       WRITE(6,21)X(I,J),Y(I,J),Z(I,J)
    21 FORMAT(3(1X,F7.3,2X))
    22 CONTINUE
       READ(5,5)(DX(I),DY(I),DZ(I),I=1,N)
       WRITE(6,27)(DX(I),DY(I),DZ(I),I=1,N)
    27 FORMAT(3X,2HDX,8X,2HDY,8X,2HDZ//3(1X,F7.3,2X))
       A(IN)=X(1,1)
```

```
 13 EE(IN)=0.
    EPOL(IN)=0.
    EDIP(IN)=0.
    DO 8 J=1,N
    DO 8 I=1,P
    R=SQRT(X(I,J)**2+Y(I,J)**2+Z(I,J)**2)
    IF(IN.EQ.1)R1(I,J)=R
    IF(IN.NE.2)GOTO30
    IF((R1(I,J)-R).GT..001)WRITE(6,31)I,J
 31 FORMAT(1HO,20X,13HERROR IN DATA/1X,2HI=,I2,5X,2HJ=,I2)
 30 EE(IN)=EE(IN)+334.*QI*Q(I)/R
    EPOL(IN)=EPOL(IN)-167.*QI**2*POL(I)/R**4
  8 CONTINUE
    IF(N.EQ.1) GO TO 7
    M=N-1
    DO 12 J=1,M
    DO 12 I=1,P
    DO 12 L=2,N
    DO 12 K=1,P
    IF(J.GE.L) GO TO 12
    RR=SQRT((X(I,J)-X(K,L))**2+(Y(I,J)-Y(K,L))**2+(Z(I,J)-Z(K,L))**2)
    EDIP(IN)=EDIP(IN)+334.*Q(I)*Q(K)/RR
    IF(IN.NE.1)RR1(J,I,L,K)=RR
    IF(IN.NE.2)GOTO12
    IF(RR1(J,I,L,K)-RR).GT..001)WRITE(6,25)J,I,L,K
 25 FORMAT(1HO,20X,13HERROR IN DATA/1X,2HJ=,12,5X,2HI=,I2,5X,2HL=,I2,5 X,2HKV,
   1X,2HK=,I2)
 12 CONTINUE
```

```
 7 E(N,IN)=EE(IN)+EPOL(IN)+EDIP(IN)
   IF(IN.EQ.20) GO TO 11
   DO 14 I=1,P
   DO 14 J=1,N
   X(I,J)=X(I,J)+DX(J)
   Y(I,J)=Y(I,J)+DY(J)
14 Z(I,J)=Z(I,J)+DZ(J)
   A(IN+1)=A(IN)+DX(1)
   IN=IN+1
   GO TO 13
11 WRITE(6,16)N,(A(IN),E(N,IN),EE(IN),EPOL(IN),EDIP(IN),IN=1,20)
16 FORMAT(1H1,4HN =,I2,23X,23HALL VALUES IN KCAL/MOLE//5H R(A),
  19X,5HTOTAL,7X,7HION-DIP,5X,7HION-POL,                4X,7HDIP-DIP,
  2 //20(1X,5(F7.2,5X)/))
   GO TO 15
17 STOP
   END
```